

# **Uncertainties in Segmentation and their Visualisation**

## **Onzekerheden in Segmentatie en hun Visualisatie**

(met een samenvatting in het Nederlands)

PROEFSCHRIFT

ter verkrijging van  
de graad van doctor aan de Universiteit Utrecht  
op gezag van de Rector Magnificus,  
Prof. dr. W. H. Gispen,  
ingevolge het besluit van het College voor Promoties  
in het openbaar te verdedigen  
op vrijdag 1 oktober 2004 des middags te 2:30 uur

door

**Arko Lucieer**

geboren op 17 januari 1977  
te Rotterdam, Nederland

**Promotoren** Prof. dr. M. J. Kraak  
Universiteit Utrecht  
Faculteit Geowetenschappen  
Prof. dr. ir. A. Stein  
Universiteit Wageningen  
Leerstoelgroep wiskundige en statistische methoden

**Leden promotiecommissie** Prof. dr. A. Bagchi  
Prof. dr. P. A. Burrough  
Prof. dr. P. F. Fisher  
Prof. dr. S. M. de Jong  
Prof. dr. ir. M. Molenaar



INTERNATIONAL INSTITUTE FOR GEO-INFORMATION SCIENCE AND EARTH  
OBSERVATION, ENSCHEDE, THE NETHERLANDS

ITC Dissertation number 113  
ITC, P.O. Box 6, 7500 AA Enschede, The Netherlands



Universiteit Utrecht, Utrecht, The Netherlands

**Universiteit Utrecht**

ISBN 90-6164-225-6

**Printed by** International Institute for Geo-Information Science and Earth Obser-  
vation, Enschede, The Netherlands

Copyright © 2004 by Arko Lucieer

To Vanessa, Marja & John



# Abstract

This thesis focuses on uncertainties in remotely sensed image segmentation and their visualisation. The first part aims to develop and implement a visual exploration tool to interact with a fuzzy classification algorithm. The proposed tool uses dynamically linked views, consisting of an image display, a parallel coordinate plot, a 3D feature space plot, and a classified map with an uncertainty map. It allows interaction with the parameters of a fuzzy classification algorithm by visually adjusting fuzzy membership functions of classes. Its purpose is to improve insight into fuzzy classification of remotely sensed imagery and related uncertainty. The visual fuzzy classification technique is tested on a Landsat 7 ETM+ image of an area in Southern France characterised by land cover objects with indeterminate boundaries. The visual classifier gives an overall classification accuracy of 88%, outperforming traditional fuzzy classifiers. Additionally, a focus group user test of the tool provides qualitative feedback and shows that insight into a fuzzy classification algorithm and uncertainty improves considerably.

Spheres and ellipsoids are used to represent class clusters in a 3D feature space prior to a remotely sensed image classification. These shapes provide only rough approximations of irregular shaped class clusters.  $\alpha$ -shapes can improve visualisation of class clusters in a 3D feature space, as  $\alpha$ -shapes visualise the shape of a class clusters more accurately. In addition,  $\alpha$ -shapes might improve insight into a classification, and related uncertainty. These shapes can clearly show where classes overlap, giving an indication for thematic uncertainty. Most classification algorithms do not take into account irregular and concave cluster shapes. Therefore, a classification algorithm, based on  $\alpha$ -shapes, is proposed and implemented. Meaningful classification results can be obtained with  $\alpha$ -shapes.

The aim of the second part of this study is to develop, implement and apply image segmentation techniques for identification of objects and quantification of their uncertainty. A split-and-merge algorithm is applied on an IKONOS image of an agricultural area in the Netherlands. Existential uncertainty of spatial objects is quantified through object boundaries. The segmentation algorithm is applied at various values of splitting and merging

---

thresholds. Objects occurring at many segmentation steps have less existential uncertainty than those occurring at only a few steps. Segmentation results are validated with a topographic map and a boundary matching technique.

The segmentation technique is extended with a supervised procedure based on grey-level and multivariate texture to extract spatial objects from an image scene. Object uncertainty is quantified to identify transition zones of objects with indeterminate boundaries. The Local Binary Pattern (LBP) operator, modelling texture, is integrated into a hierarchical splitting segmentation to identify homogeneous texture regions in an image. A multivariate extension of the standard univariate LBP operator is proposed to describe colour texture. The technique is illustrated with two case studies. The first considers an image with a composite of texture regions. The two LBP operators provide good segmentation results with accuracy values of 95% and higher. The second case study involves segmentation of coastal land form and land cover objects using Light Detection And Ranging (LiDAR) imagery and multi-spectral Compact Airborne Spectral Imager (CASI) imagery of a coastal area in the UK. The multivariate LBP operator is superior to the univariate LBP operator, segmenting the area into meaningful objects, yielding valuable information on uncertainty at transition zones. The univariate LBP measure is extended to a multi-scale texture measure to improve identification of land forms. A region growing segmentation based on the multi-scale LBP measure is applied to identify spatial land form objects from a LiDAR digital surface model (DSM). Meaningful coastal land form objects can be extracted with this algorithm.

Visualisation methods described in the first part and the segmentation techniques described in the second part are combined and extended to visualise object uncertainty. The third part of this study aims to develop and implement visualisation techniques to explore the relation between uncertainty in the spatial extent of image objects and their thematic uncertainty. An object is visualised in 3D feature space and in geographic space based on a user-defined uncertainty threshold. Changing this threshold updates both visualisations, showing the effect of uncertainty on the spatial extent of an object and its shape in feature space. Spheres, ellipsoids, convex hulls, isosurfaces, and  $\alpha$ -shapes are compared for visualisation of objects in a 3D feature space plot. These objects are derived either by visual classification or segmentation.  $\alpha$ -shapes provide the most accurate representation, however, computational demands are very high, making them unsuitable for fast interactions. Alternatively, an isosurface can provide a good approximation of an  $\alpha$ -shape, facilitating fast interaction. The visualisation technique is illustrated with the results of the case studies discussed in the first and second part of this study. Results show that this interactive visualisation tool allows for valuable inferences about object uncertainty.

# Samenvatting

Deze studie richt zich op onzekerheden in segmentatie van remote sensing beelden en hun visualisatie. Het eerste deel heeft tot doel een visuele exploratie techniek te ontwikkelen om meer inzicht te verkrijgen in een fuzzy classificatie algoritme. Deze techniek maakt gebruik van beeld visualisatie gecombineerd met een parallel coordinate plot, een 3D plot van de attribut ruimte, en een geclassificeerd beeld met informatie over onzekerheid. Het geeft de mogelijkheid voor interactie met de parameters van een fuzzy classificatie algoritme door visuele bijstelling van fuzzy membership functies voor de individuele klassen. Het doel is om inzicht te verbeteren in het functioneren van een fuzzy classificatie techniek en thematische onzekerheid. De techniek is getest op een Landsat 7 ETM+ beeld van een gebied in Zuid-Frankrijk dat gekenmerkt wordt door landbedekkings objecten met vage grenzen. Het classificatie algoritme geeft een goed resultaat met een nauwkeurigheid van 88%, wat beter is dan traditionele fuzzy classificatie algoritmen. Een gebruikers test geeft een kwalitatieve beschrijving van de gebruikte visualisatie technieken. Deze test toont aan dat inzicht in een fuzzy classificatie algoritme en onzekerheid kan verbeteren met het gebruik van visualisatie technieken.

Bollen en ellipsoïden worden gebruikt om klasse clusters in een 3D attribut ruimte te visualiseren voor een beeld classificatie. Deze vormen geven een ruwe beschrijving van onregelmatige klasse clusters.  $\alpha$ -shapes kunnen visualisatie van klasse clusters verbeteren in een 3D ruimte. Tevens kunnen  $\alpha$ -shapes gebruikt worden om inzicht in classificatie van remote sensing beelden en onzekerheid te verbeteren. De meeste classificatie algoritmen houden geen rekening met concave cluster vormen.  $\alpha$ -shapes modelleren de klasse vormen zo nauwkeurig mogelijk en deze studie laat zien hoe  $\alpha$ -shapes gebruikt kunnen worden in een beeld classificatie. Waardevolle classificatie resultaten worden behaald met deze techniek.

Het doel van het tweede deel van deze studie is het ontwikkelen, implementeren en toepassen van beeld segmentatie technieken voor identificatie van objecten en het kwantificeren van hun onzekerheid. Een 'split-and-merge' techniek is toegepast op een IKONOS beeld van een landbouwgebied

---

in Overijssel, Nederland. Thematische object onzekerheid wordt gekwantificeerd via object grenzen. De segmentatie techniek wordt toegepast met verschillende criteria voor het opsplitsen en samenvoegen van object blokken. Objecten die op meerdere segmentatie stappen voorkomen zijn stabiel en vertonen minder onzekerheid dan objecten die maar op een aantal segmentatie stappen voorkomen. Segmentatie resultaten zijn gevalideerd met een topografische kaart en een techniek die object grenzen vergelijkt.

De segmentatie techniek is verder uitgebreid met een aanpak gebaseerd op univariate- en multivariate textuur maten om ruimtelijke objecten in een beeld te detecteren. Object onzekerheid is gekwantificeerd om overgangszones tussen vage objecten te identificeren. De Local Binary Pattern (LBP) maat is geïntegreerd in een hiërarchische segmentatie procedure voor identificatie van homogene gebieden gekenmerkt door textuur. Een multivariate uitbreiding van deze textuur maat is voorgesteld en beschreven voor het modelleren van textuur in meerdere banden (multivariate textuur). De techniek is geïllustreerd met twee praktijk studies. De eerste toepassing gebruikt een beeld van een compositie van vijf kunstmatig texturen. De univariate en multivariate LBP maten geven goede segmentatie resultaten met nauwkeurigheidswaarden van 95% en hoger. Segmentatie in de tweede toepassing heeft tot doel landvorm- en landbedekkings objecten te identificeren in een Light Detection And Ranging (LiDAR) beeld en een multispectraal Compact Airborne Spectral Imager (CASI) beeld van een kustgebied in Engeland. De studie toont aan dat de multivariate LBP maat beter is dan de univariate LBP maat in segmentatie van het gebied. De segmentatie geeft waardevolle informatie over onzekerheid in de overgangszones tussen objecten. Tevens is de univariate LBP maat uitgebreid naar een textuur maat voor meerdere schalen om identificatie van landvormen te verbeteren. Een 'region growing' segmentatie techniek gebaseerd op deze maat is toegepast op een LiDAR hoogte model. Dit algoritme maakt het mogelijk om landvorm objecten te identificeren van een digitaal hoogte model van een kustgebied in Engeland. Tevens wordt een maat voor ruimtelijke onzekerheid verkregen, die waardevolle informatie geeft over overgangszones.

De visualisatie technieken die beschreven zijn in het eerste deel van deze studie en de segmentatie technieken in het tweede deel worden gecombineerd om object onzekerheid te visualiseren. Het derde deel heeft tot doel een visualisatie techniek te ontwikkelen om de relatie tussen onzekerheid in de ruimtelijke verbreiding en thematische onzekerheid van objecten te verkennen. De verbreiding van een object wordt gevisualiseerd in een 3D attribuut ruimte en in de geografische ruimte, gebaseerd op een onzekerheidsgrens gedefinieerd door een gebruiker. Verandering van deze grens laat de verandering zien in beide visualisaties. Daarmee laten deze visualisaties het effect zien van onzekerheid op de representatie van een object in beide ruimtes. Bollen, ellipsoïdes, convex hulls, isovlakken en  $\alpha$ -shapes worden vergeleken voor visualisatie van objecten in een 3D plot. Deze objecten zijn verkregen van

een visuele classificatie of een segmentatie van een beeld.  $\alpha$ -shapes geven de meeste nauwkeurige representatie van een cluster. Echter er is veel rekenkracht nodig om  $\alpha$ -shapes te berekenen en visualiseren, wat deze vormen ongeschikt maakt voor snelle interacties. Isovlakken kunnen gebruikt worden als een alternatief, omdat ze een goede beschrijving geven van een  $\alpha$ -shape en een snelle interactie mogelijk maken. Deze visualisatie techniek wordt beschreven met de resultaten van de toepassing die beschreven zijn in deel 1 en 2 van deze studie. De resultaten tonen aan dat de visualisatie techniek gebruikt kan worden om waardevolle conclusies te trekken over onzekerheden in ruimtelijke objecten.



# Acknowledgements

In September 2000, I started this Ph.D. research at ITC in Enschede. It has been a very interesting project and I would like to thank my supervisors Menno-Jan Kraak and Alfred Stein for their help, support, and trust in my work, our discussions and meetings were very valuable. I would like to thank all of my colleagues in the GIP and EOS departments for their support and company. Barend Köbben, Ton Mank, Corné van Elzaker, Willy Kock, Wim Feringa, Jeroen van der Worm, and Connie Blok, thanks for the early morning coffees in our tearoom, we have had some great laughs. Noline Emmer, thanks for your company and long chats during our trips on the train to and from ITC, and our nights in the climbing hall. Etien Koua, thanks for your company in our office.

I would like to thank Pete Fisher for his supervision in Leicester, UK. He has been a big source of inspiration and our discussions were incredibly motivating and valuable. Charlie, Renata and Harry thanks for hosting me in your home. Freek van der Meer, Arta Dilo, Raymond Nijmeijer, Norman Kerle, Wietske Bijker, Harald van der Werff, and Daniël van de Vlag thanks for your participation in the focus group user test, giving me valuable feedback on the software tool I developed for visualisation of uncertainty. I very much appreciate your comments and I hope to include them in future versions of *Parbat*. I would like to thank Steven de Jong and Raymond Sluiter from Utrecht University for providing the Landsat 7 imagery of the “La Peyne” study area. Steven has motivated me to pursue a PhD position in remote sensing and I thank him for his excellent supervision and support during my Masters in Physical Geography. Furthermore, I would like to thank Lourens Veen from Twente University for all the time he spent on the isosurface source code, chapter 8 would not have come this far without his help and insights.

Harald van der Werff, Jelle Ferwerda, Daniël van de Vlag and Marleen Noomen, the ITC AiO-team, thanks for the great time in and outside ITC. The obligatory coffee breaks and lunches were fun. I wish you all the best for the rest of your PhDs. Harald and Jelle, thanks for your friendship and company in Enschede, chatting, climbing, playing squash, or just having dinner together. I am also grateful to my friends David Molenaar, Wouter Dorigo and Tom van Maarseveen. Since we met, we have shared a lot of ups and downs and you have given me a lot of support and inspiration. I have enjoyed all of our adventures in the mountains, climbing and ski touring, or just spending time together at home having dinner, watching slides, or chatting till late.

---

## *Acknowledgements*

---

Richard Coleman and Jon Osborn from the University of Tasmania, thanks for giving me the opportunity to start a career as a lecturer and researcher in the Centre for Spatial Information Science at the University of Tasmania. I am happy to be part of such a dynamic and an ambitious team. Furthermore I would like to thank Richard Mount for his friendship, and our valuable remote sensing discussions.

Finally, I want to thank my parents Marja Roozen and John Lucieer. They have always let me made my own decisions in life. Studying Physical Geography, pursuing a PhD and emigrating to Tasmania are examples of those decisions. I would not have come this far without your love, support and help. I would like to dedicate this thesis to my parents and Vanessa, who has also been a great support. In a way, this PhD project has led to our meeting and in finishing this PhD we can now start a new life together. Thanks for all your love and encouragement.

# Contents

<b>Abstract</b>	<b>vii</b>
<b>Samenvatting</b>	<b>ix</b>
<b>Acknowledgements</b>	<b>xiii</b>
<b>List of Figures</b>	<b>xix</b>
<b>List of Tables</b>	<b>xxi</b>
<b>1 Introduction</b>	<b>1</b>
1.1 Problem description . . . . .	1
1.2 What is <i>uncertainty</i> ? . . . . .	2
1.3 Uncertainty visualisation . . . . .	4
1.4 Segmentation . . . . .	5
1.5 Research objectives . . . . .	6
1.5.1 Visualisation . . . . .	6
1.5.2 Segmentation . . . . .	6
1.5.3 Object uncertainty visualisation . . . . .	7
1.6 Software prototype . . . . .	7
1.7 Structure of the thesis . . . . .	7
<b>I Visualisation</b>	<b>11</b>
<b>2 Interactive Visualisation of a Fuzzy Classification</b>	<b>13</b>
2.1 Introduction . . . . .	13
2.2 Fuzzy classification . . . . .	14
2.3 Uncertainty visualisation . . . . .	17
2.4 Components of the visual classifier . . . . .	19

---

2.5	Visualisation of classes . . . . .	21
2.6	Visual fuzzy classification . . . . .	24
2.7	Implementation of the prototype <i>Parbat</i> . . . . .	26
2.8	Prototype test case . . . . .	29
2.8.1	Study area and data set . . . . .	29
2.8.2	Visual fuzzy classification of the study area . . . . .	30
2.8.3	Fine-tuning the visual classification . . . . .	32
2.8.4	Visual classification based on Principal Components . . . . .	34
2.8.5	Visual classifier versus standard fuzzy classifiers . . . . .	34
2.9	Prototype evaluation with focus groups . . . . .	36
2.10	Discussion . . . . .	38
2.11	Conclusions . . . . .	40
<b>3</b>	<b>Alpha-shapes for Visualisation and Classification</b>	<b>43</b>
3.1	Introduction . . . . .	43
3.2	Class cluster shape . . . . .	44
3.3	$\alpha$ -shapes . . . . .	46
3.4	$\alpha$ -shape implementation and visualisation . . . . .	46
3.5	$\alpha$ -shape based classification . . . . .	49
3.6	$\alpha$ -shape classification results . . . . .	51
3.7	Distance metrics for $\alpha$ -shape based classifier . . . . .	52
3.8	Discussion . . . . .	55
3.9	Conclusions . . . . .	56
<b>II</b>	<b>Segmentation</b>	<b>57</b>
<b>4</b>	<b>Segmentation of Spatial Objects and their Uncertainty</b>	<b>59</b>
4.1	Introduction . . . . .	59
4.2	Image segmentation with a split-and-merge algorithm . . . . .	61
4.3	Quantifying existential object uncertainty . . . . .	62
4.4	Segmentation validation measures . . . . .	63
4.5	Study area . . . . .	64
4.6	Segmentation results . . . . .	65
4.7	Segmentation validation . . . . .	67
4.8	Discussion . . . . .	72
4.9	Conclusions . . . . .	74
<b>5</b>	<b>Texture-based Segmentation to Identify Fuzzy Objects</b>	<b>75</b>
5.1	Introduction . . . . .	75
5.2	Study area . . . . .	77

5.3	Texture . . . . .	79
5.4	Texture measure - the Local Binary Pattern Operator (LBP) . . .	79
5.5	Texture-based image classification . . . . .	81
5.6	Texture-based image segmentation . . . . .	83
5.7	Texture image example . . . . .	85
5.8	Segmentation of LiDAR DSM . . . . .	88
5.9	Segmentation of CASI image . . . . .	90
5.10	Discussion and conclusions . . . . .	92
<b>6</b>	<b>Multivariate Texture-based Segmentation</b>	<b>95</b>
6.1	A multivariate texture model . . . . .	95
6.2	Colour texture example . . . . .	98
6.3	Multivariate texture segmentation of a CASI image . . . . .	100
6.4	Identification of geological units in Mongolia . . . . .	102
6.4.1	Study area and geological map . . . . .	102
6.4.2	Remote sensing imagery . . . . .	103
6.4.3	Segmentation results . . . . .	104
6.4.4	Segmentation validation . . . . .	107
6.5	Discussion and conclusions . . . . .	108
<b>7</b>	<b>Multi-scale Texture for Land Form Segmentation</b>	<b>111</b>
7.1	Introduction . . . . .	111
7.2	Multi-scale texture model . . . . .	113
7.3	Seeded region growing . . . . .	113
7.4	Multi-scale texture measures from a LiDAR DSM . . . . .	116
7.5	Texture-based region growing for identification of land form objects	118
7.6	Discussion and conclusions . . . . .	120
<b>III</b>	<b>Object uncertainty visualisation</b>	<b>123</b>
<b>8</b>	<b>Visualisation of Thematic and Spatial Object Uncertainty</b>	<b>125</b>
8.1	Introduction . . . . .	125
8.2	Isosurfaces . . . . .	127
8.3	Comparison of object representations . . . . .	130
8.4	Visual link between thematic uncertainty and spatial uncertainty .	131
8.5	Case study: classification . . . . .	133
8.6	Case study: segmentation . . . . .	138
8.7	Discussion . . . . .	144
8.8	Conclusions . . . . .	145

<b>9 Conclusions</b>	<b>147</b>
9.1 Visualisation . . . . .	147
9.2 Segmentation . . . . .	148
9.3 Object uncertainty visualisation . . . . .	150
<b>Bibliography</b>	<b>151</b>
<b>ITC Dissertations</b>	<b>161</b>
<b>Publications of the author</b>	<b>171</b>
<b>Biography</b>	<b>175</b>

# List of Figures

1.1	Thesis structure . . . . .	9
2.1	Three main visualisations . . . . .	22
2.2	3D feature space plot with class spheres . . . . .	23
2.3	Interactive visual fuzzy classification . . . . .	25
2.4	Visual fuzzy classification result . . . . .	27
2.5	<i>Parbat</i> prototype . . . . .	28
2.6	Landsat image of the ‘La Peyne’ study area . . . . .	30
2.7	Fine-tuning of classification result . . . . .	33
2.8	Visual fuzzy classification of 3 PCA bands . . . . .	35
2.9	Standard fuzzy <i>c</i> -means classification . . . . .	37
3.1	Circle, ellipse, convex hull and $\alpha$ -shape . . . . .	45
3.2	2D $\alpha$ -shape . . . . .	47
3.3	Comparison of class shapes . . . . .	48
3.4	Land cover class $\alpha$ -shapes . . . . .	49
3.5	Distance metric $\alpha$ -shape classifier . . . . .	50
3.6	$\alpha$ -shape based fuzzy classificaiton result . . . . .	51
3.7	Problems with distance metric for $\alpha$ -shape classifier . . . . .	53
3.8	$\alpha$ -shape as membership function . . . . .	54
3.9	$\alpha$ -shape 3D medial axis . . . . .	55
4.1	Existential uncertainty depicted by boundary stability . . . . .	62
4.2	Colour composite of an IKONOS image of the study area . . . . .	65
4.3	Segmentation result . . . . .	66
4.4	Image of the Boundary Stability Index (BSI) . . . . .	67
4.5	Object boundaries from segmentation result . . . . .	68
4.6	Boundaries from topographic map and seven reference objects . . . . .	68
4.7	Number of segments within each reference object . . . . .	69
4.8	Segment overlap percentages . . . . .	70

---

4.9	Segment $AFI$ values . . . . .	70
4.10	$D(B)$ and $D(B)_{corr}$ values . . . . .	72
4.11	$CDM$ values . . . . .	73
5.1	Overview of the study area . . . . .	78
5.2	Circular neighbourhood set . . . . .	80
5.3	Texture example . . . . .	86
5.4	Unsupervised split-and-merge segmentation . . . . .	87
5.5	Supervised texture-based segmentation . . . . .	87
5.6	Texture measures for LiDAR DSM . . . . .	88
5.7	Segmentation result LiDAR DSM . . . . .	90
5.8	Texture measures for band 12 of a CASI image . . . . .	91
5.9	Segmentation result band 12 CASI image . . . . .	92
6.1	Multivariate neighbourhood set . . . . .	97
6.2	Segmentation of colour textures . . . . .	99
6.3	Segmentation of land cover . . . . .	101
6.4	Geological map of the study area . . . . .	104
6.5	Landsat and ASTER images of the study area in Mongolia . . . . .	105
6.6	Segmentation of Landsat TM image . . . . .	106
6.7	Segmentation of ASTER image . . . . .	106
6.8	Comparison ASTER segmentation with geological map . . . . .	108
7.1	Multi-scale circular neighbourhood set . . . . .	114
7.2	3D view of LiDAR DSM of the study area . . . . .	116
7.3	Multi-scale texture values . . . . .	117
7.4	Region growing results . . . . .	119
7.5	Detailed section of the fore dune . . . . .	120
8.1	Computational speed for generation of each visualisation . . . . .	131
8.2	Comparison of shapes for object visualisation . . . . .	132
8.3	Visual fuzzy classification of Landsat image . . . . .	134
8.4	Isosurface for class Agriculture . . . . .	135
8.5	Spatial extent of class Agriculture . . . . .	136
8.6	Overlap of class Agriculture and Urban . . . . .	137
8.7	Object uncertainty for CASI land cover segmentation . . . . .	139
8.8	Isosurface for Woodland object . . . . .	140
8.9	Spatial extent of Woodland object . . . . .	141
8.10	Isosurface for Fore dune object . . . . .	142
8.11	Spatial extent of Fore dune object . . . . .	143
8.12	Overview of suitability of shapes . . . . .	145

# List of Tables

2.1	Classification accuracy % for a classification based on the <i>initial</i> class sphere configuration . . . . .	31
2.2	Classification accuracy % for a classification based on the <i>adjusted</i> class sphere configuration . . . . .	32
2.3	Classification accuracy % for a classification based on an <i>adjusted</i> class sphere configuration of the first three Principal Components .	34
2.4	Classification accuracy assessment for different classifiers . . . . .	36
3.1	Classification accuracy % for a classification based on $\alpha$ -shapes . .	52
3.2	Classification accuracy for $\alpha$ -shapes and convex hulls . . . . .	52
4.1	Description of seven reference objects used for validation . . . . .	69
5.1	Confusion matrix with per-class accuracy values % for segmentation of texture image . . . . .	88
5.2	Confusion matrix with per-class accuracy values % for segmentation of LiDAR DSM . . . . .	90
5.3	Confusion matrix with per-class accuracy values % for segmentation of CASI image . . . . .	92
6.1	Confusion matrix with per-class accuracy values % for segmentation of texture image . . . . .	100
6.2	Confusion matrix with per-class accuracy values % for multivariate texture-based segmentation of CASI image . . . . .	102
6.3	Confusion matrix with per-class accuracy values % for segmentation of Landsat TM image . . . . .	107
6.4	Confusion matrix with per-class accuracy values % for segmentation of ASTER image . . . . .	107

---

*List of Tables*

---

# Chapter 1

## Introduction

*Everything is vague to a degree you do not realise  
till you have tried to make it precise.*

from “The Philosophy of Logical Atomism” — Bertrand Russell

### 1.1 Problem description

Remote sensing imagery can provide a valuable source of information for mapping the Earth surface. Satellite images have made it possible to map at global to regional scales, to map remote areas, and to update existing information efficiently and cheaply (Richards and Jia, 1999; Lillesand and Kiefer, 2000; Campbell, 2002). Advances in spatial resolution now allow us to detect small objects from both airborne sensors and spaceborne sensors. Additionally, the increase in spectral resolution of multispectral and hyperspectral sensors has made it possible to derive information on the physical composition of the surface, such as chemical components in vegetation, soil, rock and water. This makes remote sensing data suitable for a range of applications, like land cover mapping, geology, botany, forestry, biology, urban planning, and oceanography. For all these applications, an important stage in image processing is the translation from reflectance or digital numbers (DN) to thematic information, also known as classification. We classify objects by reducing a multiplicity of phenomena to a relatively small number of general classes (Tso and Mather, 2001). Classification is often performed to generalise

---

a complex image into a relatively simple set of classes. A classified map is then used as input into a geographic information system (GIS) for further processing or analysis. Such inference is most often less than perfect and there is always an element of uncertainty in a classification result. As it can affect further processing steps and even decision making, it is important to understand, quantify and communicate uncertainty.

## 1.2 What is *uncertainty*?

“Where is the highest mountain on Earth?” This is a simple question and one would most certainly answer: ‘the Mount Everest in the Himalayas’. However, this question presupposes that the concept ‘mountain’ is precisely defined when in fact it is not. It is a vague concept as it gives rise to paradoxical arguments of the Sorites variety (Varzi, 2001; Fisher et al., 2004). The Sorites paradox can be used to test whether a concept is vague (Fisher, 2000):

Is one rock a pile of rocks?

The answer to this simple question is clearly ‘No’.

If a second rock is added to the first, is there a pile?

Again the answer is ‘No’.

If a third rock is added, is there a pile?

For a third time the answer is ‘No’

The argument so far is uncontroversial. From it, however, a general form of argument can be concluded (Fisher, 2000). If there are  $n$  rocks, but no pile, then adding one rock to make  $n + 1$  rocks will not make a pile. By repeated application of this premise it can be seen that as  $n$  increases to a large number, the addition of a single rock still does not change a non-pile into a pile. Therefore, the argument is logically valid, yet the conclusion is plainly false (Varzi, 2001).

Mount Everest, measuring 8850 m (above sea level), is unmistakably the *highest* mountain on Earth. There is still a problem; not only the definition of a mountain is inherently vague, also the spatial extent suffers from vagueness. Where exactly *is* Everest? Where does it begin and where does it end? Everest does not refer to a volume of a pile of rocks demarcated from its surrounding. A mountain has a spatial extent, but that extent is a matter of degree. Its summit is definitely part of the mountain, its (lower) slopes and valleys are to a lesser extent part of the moun-

tain. This example shows that the concept ‘mountain’ is vague in its definition as well as in its spatial extent. Not only ‘mountain’ but virtually every geographic concept suffers from vagueness (Fisher, 2000; Varzi, 2001; Fisher et al., 2004). Therefore, uncertainty, of which vagueness is a component, has been an important topic in recent scientific literature on geographical information science and remote sensing (Burrough and Frank, 1996; Canters, 1997; Fisher, 1999; Wel, 2000; Foody and Atkinson, 2002).

Data uncertainty as a component of data quality may be taken into account when considering the ‘fitness for use’ of geographical data for a particular application. With the increasing use of remotely sensed data as input in a GIS, uncertainty in remotely sensed image classification has received more attention (Canters, 1997; Wel, 2000; Zhang and Foody, 2001; Foody and Atkinson, 2002). Various types of uncertainty can influence information extraction from remotely sensed imagery. Atmospheric conditions, geometric calibration, sensor sensitivity, and sensor resolution are important during data acquisition. Concerning image classification, uncertainty can arise from vagueness in class definition, mixed pixels, and transition zones or fuzzy boundaries.

Many classification methods for extraction of land cover objects have been developed, and many strategies and modifications have been proposed to improve classification accuracy, being another component of data quality. In most studies, map accuracy is assessed by means of a confusion or error matrix, comparing a sample of classified pixels with reference data obtained from aerial photographs or ground surveys. Much work has been published on optimal strategies for sampling (Stein and Ettema, 2003), accuracy measures have been refined to deal with change agreement, and methods have been presented to estimate statistically sound classification probabilities from the confusion matrix (Rosenfield et al., 1982; Congalton, 1991; Foody, 1992; Stehman, 1992; Fenstermaker, 1994). Measures of accuracy, like the confusion matrix, can only be derived for a land cover class as a whole. Therefore, the most fundamental drawback of the confusion matrix is its inability to provide information on spatial distribution of uncertainty in a classified scene. Information on thematic and spatial uncertainty is essential in determining the quality of a classification result.

Fuzzy set theory as an expression of concepts of vagueness is an appropriate model for working with remotely sensed imagery (Foody, 1996; Fisher, 1999). To adapt to the fuzziness characteristic of many natural phenomena, fuzzy classification approaches have been proposed and successfully applied in remotely sensed land cover classification (Wang, 1990; Foody, 1996; Zhang and Foody, 2001). These ‘soft’ or ‘fuzzy’ classifiers can be used to quantify uncertainty as these classifiers

model the membership that a pixel belongs to a certain class. The strength of class membership is an indication of thematic uncertainty. The spatial distribution of these uncertainty values provide valuable information on the spatial extent of classes or objects. In addition to quantification of uncertainty, exploration and communication are essential in uncertainty analysis. Visualisation seems an appropriate means for the presentation and exploration of patterns and spatial behaviour of uncertainty (MacEachren, 1992; Fisher, 1994; Goodchild et al., 1994; Hootsmans, 1996; Wel et al., 1997; Blenkinsop et al., 2000; Bastin et al., 2002).

### 1.3 Uncertainty visualisation

Uncertainty visualisation aims to present data in such a way that users become aware of the locations and degree of uncertainties in their data to make more informed analyses and decisions. Although a desire exists to reduce uncertainty from an end-users and decision-makers perspective, it can never be eliminated (Foody and Atkinson, 2002). Therefore, visualisation techniques are required to explore and to present uncertainty information in an accessible way.

Maps are a form of scientific visualisation, and maps existed before visualisation developed into a distinct scientific field. The objective of visualisation is to analyse information about data relationships graphically, whereas cartography aims at conveying spatial relationships. The emphasis in scientific visualisation is more on its analytical power (exploratory analysis) than on its communicative aspects; it is primarily directed at discovery and understanding. In cartography, emphasis can lie equally on exploration and presentation (MacEachren and Kraak, 1997; Kraak and MacEachren, 1999). MacKinaly and Schneiderman (1999) stated that visualisation is the use of computer-supported, interactive, visual representations of data to amplify cognition.

In recent years, visualisation tools have been proposed that focus on presentation and exploration of uncertainty in remotely sensed image classifications (Wel et al., 1997; Blenkinsop et al., 2000; Bastin et al., 2002). None of these tools, however, provided a way of visually interacting with a classification algorithm. Visual interaction could greatly improve insight into classification and related uncertainty. Methods and tools are required to allow a user to explore uncertainty in spatial data visually and to review the effects of different decisions during classification. Visual exploration of classification uncertainty and uncertainty related to image objects are, therefore, the focal points of this research. Visual exploration of the relation between the thematic component and spatial component of uncertainty

can provide meaningful information on object transition zones or class overlap.

## 1.4 Segmentation

Remote sensing classification is often used to partition an image into meaningful objects. Classifiers, either supervised or unsupervised, are most often pixel-based assigning a class label to each individual pixel. They are based on distance or similarity measures in attribute or feature space. In contrast, *segmentation* in remote sensing, identifies homogeneous image objects based on spatial properties. Spatial relations between pixels are an important source of information that can help in object extraction from remotely sensed imagery. The focus of classification techniques, therefore, is on thematic pixel information, whereas, for segmentation techniques it is on spatial information. Segmentation is used to identify image objects. In a subsequent object-based classification, information about these objects, like reflectance distribution, object shape and size, and object semantics can be used to improve classification. This study focuses on segmentation for identification of image objects. Additionally, the use of texture may be important. Texture reflects the spatial structure of pixel values in an image, and it is therefore indispensable in segmenting an area into sensible geographical units. A focal point of this study is the use of univariate and multivariate texture models in segmentation to improve object identification.

Recent research on remote sensing classification has focused on modelling and analysis of uncertainty in a final classification result. Both fuzzy and probabilistic approaches have been applied to uncertainty modelling in remote sensing classification (Canters, 1997; Foody, 1992; Foody, 1996; Hootsmans, 1996; Wel et al., 1997; Wel, 2000; Zhang and Foody, 2001). Most studies focused on pixel-based classification uncertainty. An object-based approach may reduce uncertainty. Additionally, interpretation of uncertainty of real world objects may be more intuitive than that of individual pixels. Geographical objects are often characterised by vagueness, which may be caused by natural transition zones. Quantification of extensional uncertainty (Molenaar, 1998), or uncertainty in the spatial extent of objects, can help to identify these transition zones.

## 1.5 Research objectives

The main aims of this study are:

- To develop and apply explorative visualisation tools to interact with a fuzzy classification algorithm that help to improve understanding of fuzzy classification and thematic uncertainty.
- To develop, implement and apply (texture-based) segmentation methods to identify image objects and to quantify object uncertainty.
- To develop and implement visualisation techniques to explore the relation between thematic uncertainty and spatial uncertainty related to image objects.

### 1.5.1 Visualisation

Objectives from the visualisation perspective:

- To develop and implement techniques and methods to visually explore uncertainty in remotely sensed land cover classification.
- To develop and implement techniques to visually interact with a fuzzy classification algorithm to improve understanding of classification and underlying thematic uncertainty.
- To develop and implement techniques to visualise the shape of thematic classes in feature space to improve visual inferences about thematic uncertainty.

### 1.5.2 Segmentation

Objectives from the segmentation perspective:

- To develop, implement and apply segmentation techniques for identification of image objects from multi-spectral remotely sensed imagery.
- To develop, implement and apply texture models to improve segmentation.

- To develop and implement techniques to quantify uncertainty related to objects.

### 1.5.3 Object uncertainty visualisation

Objectives from the uncertainty perspective:

- To develop and implement visualisation methods to explore the relation between uncertainty in the spatial extent of objects and their thematic uncertainty.

## 1.6 Software prototype

All techniques described in this study are implemented in a research prototype called *Parbat*. The software tool, is programmed in Java, using the Java Advanced Imaging library (JAI) for advanced image processing and the Java 3D library for 3D visualisation (Sun Microsystems Inc., 2004). One advantageous property of Java is its platform in-dependency, meaning that *Parbat* can be used on most operating systems. The prototype can be downloaded from <http://parbat.lucieer.net> (Lucieer, 2004). The reader of this thesis is encouraged to try the software, to experience the full effect of the interactive visualisation and image processing techniques described in this study.

## 1.7 Structure of the thesis

Figure 1.1 shows the structure of this thesis, outlining the focus of the individual chapters. Part I discusses *pixel-based* classification techniques and visualisation of *thematic uncertainty*. In part II, identification of *objects* is discussed and uncertainty is modelled both in the *spatial and thematic* domain. Part III aims to link these domains, visualising the *relation between spatial and thematic uncertainty of objects*.

Part I on visualisation, starts with chapter 2 about an interactive visual fuzzy classification technique. Land cover is classified from a Landsat image of an area

in southern France. The focus of this chapter is on the thematic aspect of uncertainty in a fuzzy remote sensing classification and interaction with a fuzzy classification algorithm. Chapter 3 focuses on the shape of class clusters in 3D feature space.  $\alpha$ -shapes are used to visualise the shape of reference class clusters and  $\alpha$ -shapes are used in a supervised fuzzy classification to account for irregular cluster shapes. Part II on segmentation, starts with chapter 4 about a split-and-merge image segmentation algorithm to identify land cover objects in an IKONOS image scene. A range of segmentation parameters is used to model spatial uncertainty through object boundaries. Chapter 5 continues with a supervised texture-based segmentation algorithm. It is applied to a multi-spectral airborne image (CASI) of a coastal area in northwest England. Uncertainty is quantified through object building blocks to identify transition zones between fuzzy objects. The texture-based segmentation algorithm is extended in chapter 6 for the multivariate case. Two case studies show that meaningful land cover and geological objects can be extracted from different remotely sensed images. Again, uncertainty values give valuable information on spatial uncertainty in transition zones. In chapter 7 the texture model is extended with a multi-scale approach to identify land form objects from a LiDAR digital surface model (DSM). A Region growing algorithm segments meaningful coastal land form objects from a DSM, providing useful information on object transition zones. In part III, chapter 8 describes a visualisation tool to explore the relation between uncertainty in the spatial extent of objects and their thematic uncertainty. It provides insight into object uncertainty both in the spatial and thematic domain. The thesis is concluded with chapter 9.

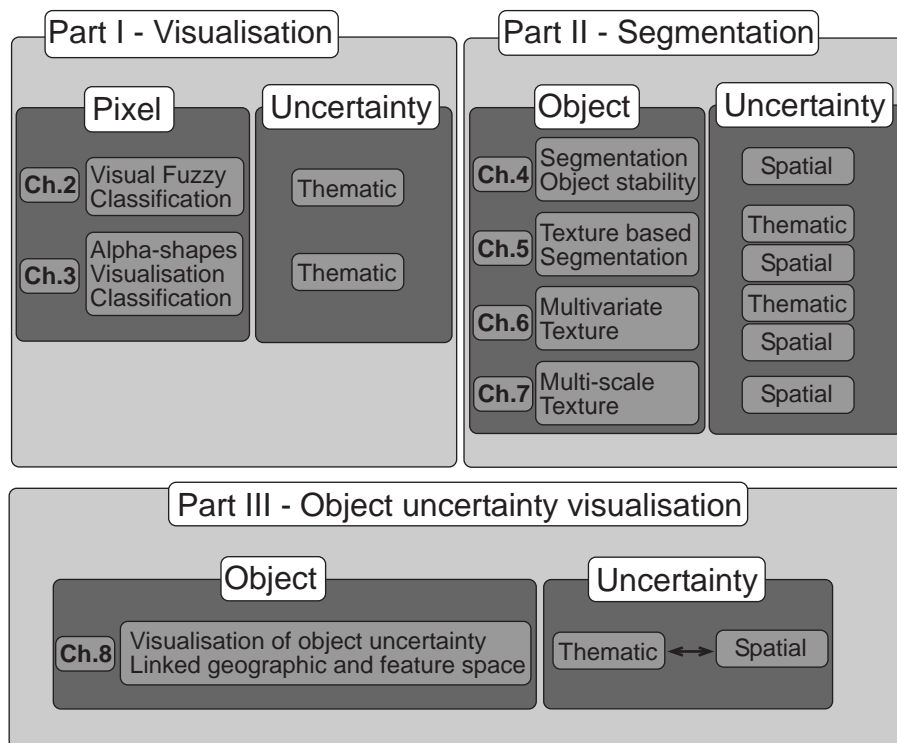


Figure 1.1: Thesis structure

*1.7. Structure of the thesis*

---

Part I

# Visualisation





## Chapter 2

# Interactive Visualisation of a Fuzzy Classification\*

*Everyone is an explorer.  
How could you possibly live your life looking at a door  
and not open it?*

R. D. Ballard

### 2.1 Introduction

Most proprietary GIS and remote sensing software provide numerous conventional and advanced classification algorithms. However, most if not all of these packages do not offer tools to model, visualise and manage uncertainty in classifications.

---

\*This chapter is based on the following papers:

Lucieer, A. and Kraak, M. J. (2004). Interactive and visual fuzzy classification of remotely sensed imagery for exploration of uncertainty, *International Journal of Geographical Information Science* **18**(5): 491–512.

Lucieer, A. and Kraak, M. J. (2002). Interactive visualisation of a fuzzy classification of remotely sensed imagery using dynamically linked views to explore uncertainty, in G. Hunter and K. Lowell (eds), *Proceedings Accuracy 2002, 5th International Symposium On Spatial Accuracy Assessment in Natural Resources and Environmental Sciences*, Melbourne, Australia, pp. 348–356.

---

Many of these packages can produce good colourful thematic maps, however, users nowadays want to be presented with information about the quality of these maps. Uncertainty in classification is an important aspect of the data quality and usability or ‘fitness for use’ of a classified map. Therefore, modelling and communication of uncertainty is becoming more important. An appropriate way to present spatial and thematic behaviour of uncertainty is via visualisation. In recent years, visualisation prototypes have been proposed that focus on presentation and exploration of uncertainty in a remotely sensed image classification (Wel et al., 1997; Blenkinsop et al., 2000; Bastin et al., 2002). However, none of these tools provide a way of interacting with a classification algorithm itself. Visual interaction with the classification algorithm could greatly improve insight into classification and related uncertainty.

This chapter describes and demonstrates a novel visualisation tool that allows for interaction with a supervised fuzzy classification algorithm. The objective of this chapter is to develop, implement and apply a geovisualisation tool by which a geoscientist can interact with the parameters of a fuzzy classification algorithm in order to gain insight into the working of a fuzzy classification and related uncertainty, and to possibly refine the classification result. For this study, a Landsat 7 ETM+ image of an area characterised by semi-natural vegetation types was selected. Transition zones between these vegetation types are known to be problematic in image classification. The prototype was evaluated with a focus group user test.

## 2.2 Fuzzy classification

Supervised image classification is a technique that is often applied in analysis of remotely sensed data. The result of such a classification is a thematic map with a label for each pixel of the class with which it has the highest strength of membership. This hard or crisp classification is based on conventional crisp set theory. A conventional classification of remotely sensed imagery, models the study area as a number of unique, internally homogeneous classes that are mutually exclusive. However, these assumptions are often invalid, especially in areas where transition zones and mixed pixels occur. Land cover types are rarely internally homogeneous and mutually exclusive, therefore, classes can hardly ever be separated by sharp or crisp boundaries, in feature space as well as geographic space. Furthermore, complex relationships exist between spectral responses recorded by the sensor and the situation on the ground, where similar classes, pixels or objects show varied spec-

tral responses and similar spectral responses may relate to dissimilar classes, pixels or objects. Moreover, remotely sensed images contain many pixels where boundaries or sub-pixel objects cause pixel mixing, with several land covers occurring within a single pixel. Finally, classes are often hard to define resulting in vagueness and ambiguity in a classification scheme. Most, if not all, geographical phenomena are poorly defined to some extent and, therefore, fuzzy set theory as an expression of concepts of vagueness is an appropriate model for working with remotely sensed imagery (Fisher, 1999; Zhang and Foody, 2001). To adapt to the fuzziness characteristic of many natural phenomena, fuzzy classification approaches have been proposed (Wang, 1990; Foody, 1996; Zhang and Foody, 2001).

Fuzzy classification is based on the concept of fuzzy sets (Zadeh, 1965). In the fuzzy set model, the class assignment function attributes to each element a grade of membership in the real interval  $[0,1]$  for every defined set. This grade of membership corresponds to the degree to which the element is similar to the concept or prototype represented by that set. Accordingly, fuzzy sets enable representation of imprecisely defined classes such as land cover classes. Several techniques exist to derive fuzzy memberships. These techniques can be divided in two groups (Burrough and McDonnell, 1998):

- The Similarity Relation Model is data-driven. It involves searching for patterns within a dataset similar to traditional clustering. The most wide-spread method is the Fuzzy  $c$ -means algorithm (Bezdek, 1981).
- The Semantic Import Model is user-driven. An expert defines the membership functions (Evans, 1977).

The fuzzy  $c$ -means classifier (FCM) uses an iterative procedure that starts with an initial random allocation of the objects to be classified into  $c$  clusters. Given the cluster allocation, the centre of each cluster (in terms of attribute values) is calculated as the weighted average of the attributes of the objects. In the next step, objects are reallocated among the classes according to the relative similarity between objects and clusters based on a well-known distance measure: the Euclidean, Diagonal (attributes are scaled to have equal variance) or Mahalanobis (both variance and covariance are used for distance scaling) metrics are frequently used. Reallocation proceeds by iteration until a stable solution is reached where similar objects are grouped together in a cluster. Their membership value gives their degree of affinity with the centroid of the class (Bezdek, 1981). Membership  $\mu$  of the  $i^{th}$  object to the  $c^{th}$  cluster of  $n$  number of classes in ordinary fuzzy  $c$ -means, with  $d$  the distance measure used for similarity, and the fuzzy exponent  $q$  determining the amount of fuzziness, is defined as:

$$\mu_{ic} = \frac{(d_{ic})^{\frac{-2}{q-1}}}{\sum_{c'=0}^n (d_{ic'})^{\frac{-2}{q-1}}} \quad (2.1)$$

Fuzzy clustering techniques like the FCM are unsupervised. This means, that the data are unlabelled. In some applications, however, a part of the data set has labels. For example, an expert in the training stage of a supervised remotely sensed image classification could obtain these labels. Zhang and Foody (2001) apply a modified version of the fuzzy  $c$ -means algorithm in order to develop a fully-fuzzy supervised classification method. In the supervised fuzzy  $c$ -means, the class centroids are determined from the training data. This reduces the clustering algorithm to a one step calculation, resulting in fuzzy membership values for each pixel in each of the defined classes.

The fuzzy exponent, fuzziness or overlap parameter determines the amount of fuzziness or class overlap. If this parameter is close to one, allocation is crisp and no overlap is allowed. For large values, there is complete overlap and all clusters are identical. The fuzziness of the classification can be modulated by varying the magnitude of the fuzziness parameter. Ideally, it should be chosen to match the actual amount of overlap. However, class overlap is generally unknown. Although the fuzziness parameter is often set between 1.5 and 3.0, no clear arguments for the choice of these values are presented (Burrough and McDonnell, 1998; Foody, 1996; Zhang and Foody, 2001).

Alternatively, expert knowledge of the area can be used to define shape, width and overlap of the membership functions for each class in a semantic import approach. However, a well-defined and functional classification scheme should exist.

Visualisation could be helpful in determining fuzziness between classes. If one would picture a classification of remotely sensed imagery, one could visualise the procedure in a feature space plot. In fact, classification is a clustering procedure in which unclassified pixels are labelled according to their position in relation to the position of class clusters in feature space. Visualisation of reference classes, their overlap and the position of pixels relative to the class clusters could greatly improve insight into classification. Visualisation could also help in exploring and adjusting overlap between classes. Thus, visualisation might improve the result and understanding of a fuzzy classification by interaction with its parameters.

## 2.3 Uncertainty visualisation

In the past one had to rely on traditional methods of cartographic expressions for visualisation of uncertainty. Today, it is possible to work in an interactive and dynamic visualisation environment that incorporates new methods, as those proposed here, alongside traditional methods. Traditional methods were mainly based on the theory of semiology of graphics of Bertin (1967). For example, MacEachren (1992) investigated the use of these graphic variables for uncertainty depiction, noting the crucial importance of logically coupling visual variables with data scale. Of the extended set of Bertin's variables, MacEachren suggested colour saturation as the most logical for uncertainty visualisation. Wel et al. (1997) proposed four static visualisation variables for conveying the quantitative character of uncertainty in remotely sensed image classification using probability vectors of individual pixels. Those variables being: value (grey-scale maps), colour saturation (bivariate maps), colour hue (associative ranking maps) and a combination of the latter two variables (dichotomy maps). An example is the traffic light principle: red, orange and green convey to a user prohibition, alertness, and permission respectively. Hootsmans (1996) proposed colour lightness and saturation to visualise uncertain information derived from fuzzy sets. Hootsmans combined colour hue to depict thematic class information and colour saturation or lightness to visualise uncertainty in one static map.

Techniques as described above focused on the extraction of uncertainty information from a classification, either as a probability vector or a membership vector per pixel, and presentation of this information to a user. The probability or membership vectors are summarised in a single uncertainty number, for example by computing the maximum membership or probability, confusion index or entropy from these vectors. These uncertainty values were then visualised with one of the techniques describe above, either as an uncertainty map or a thematic map combined with uncertainty information. These types of visualisations can help in communicating uncertainty in the final classification product, however, they do not allow for interaction with the classification.

Developments in computer graphic technology introduced dynamic visualisation techniques in cartography. For example, animation techniques were implemented to improve interpretation of large amounts of data, as is the case in visualisation of (classification) uncertainty. MacEachren (1994) distinguished between different uses of temporal graphic variables: to animate maps and to depict dynamic processes in time. Sequential display of different uncertainty maps and different thematic maps derived from the same image may make up an anima-

tion. For example, probabilities can be visualised sequentially, according to their ranking, thereby enabling the representation of all probabilities underlying a classification. This animation can follow different schemes, such as simply sequential, progressive, cyclic and back-and-forth. Fisher (1994) proposed duration as a variable to depict uncertainty: the higher the probability, the longer the period of time the class colour is displayed. Wel et al. (1997) proposed a method to toggle a thematic map and associated uncertainty map to result in a combined sensation of classes and uncertainty. Hootsmans (1996) used animation techniques to represent uncertainty related to fuzzy series analysis. A sequence of maps was generated by processing a fuzzy series for a set of alpha-cuts. Ehlschlaeger et al. (1997) described a technique of visualising uncertainty in elevation data using animation.

These dynamic visualisation techniques offered a more advanced and flexible solution to visualising uncertainty information. They provided insight into (per-pixel) uncertainty in the classification result by means of visualising the entire vector of probabilities or memberships. Most, if not all, of the mentioned techniques focused on visualising uncertainty in the classification result and did not allow for interaction with the classification. Another disadvantage of these techniques is that visualisation and interpretation of uncertainty becomes difficult when there is a large number of classes.

An interactive visualisation environment might be required to be able to improve the exploration of a classification and related uncertainty. The choice of a specific visualisation technique also depends on the user group. For decision makers, visualisation of uncertainty in the form of static maps might be sufficient, however, a scientific expert needs more in order to be able to improve the classification process. Geographic visualisation (geovisualisation or GVis) techniques might be helpful in this sense (MacEachren and Kraak, 2001). These techniques focus on exploration as opposed to presentation. Interactive visualisation techniques such as dynamically linked views (Dykes, 1997; MacEachren, 1994) and geographic brushing (Monmonier, 1989) are essential for exploration of geospatial information. A special issue of the *International Journal of Geographical Information Science* was devoted to visualisation for exploration of spatial data (Kraak and MacEachren, 1999). Several authors showed that geovisualisation tools with dynamically linked views facilitate exploratory analysis and ‘visual thinking’ (Andrienko and Andrienko, 1999; MacEachren et al., 1999). Therefore, uncertainty visualisation should not just present expert users with meta-information on data quality but should also enable them to explore uncertainty and its relation to the original data.

Recent studies (Bastin et al., 2002; Blenkinsop et al., 2000) showed that ex-

ploratory geovisualisation tools can help to improve the expert's understanding of uncertainty in a classified image scene. They proposed a combination of static, dynamic and interactive visualisations for exploration of classification uncertainty. Again, dynamically linked views and brushing functionality played a key role in these prototypes. The focus of these tools is on visual exploration of uncertainty in a classification result using linked displays of the original image, a parallel coordinate plot, a 2D feature space plot, the classified image with thematic classes, the uncertainty image displaying an uncertainty summary statistic per pixel and animation of alternative classifications. These tools provided better insight into classification uncertainty, however, they do not allow for interaction with the parameters of a classification algorithm. A user should be able to visually interact with a classification algorithm to improve their knowledge of the nature and effects of the algorithm. Improved understanding may contribute to a superior classification. A feature space plot, dynamically linked with an image display and the classification result, may provide the best technique to visualise a classification. A user should be able to adapt the reference class clusters in a feature space plot to change the parameters of a fuzzy classification algorithm. Visual interaction with these parameters can help to gain insight into the origin and effect of uncertainty in a classification. Another advantage is that it can help to fine-tune the classification result.

## 2.4 Components of the visual classifier

In this study, the visualisation design of MacEachren et al. (1999) is applied. MacEachren et al. (1999) proposed three dynamically linked representation forms that facilitate data exploration. Their prototype consisted of:

- Geoviews in which geographic space is mapped.
- Parallel coordinate plots that display several parallel axes, one for each variable in the data set with a line connecting individual records from one axis to the next, producing a signature.
- 3D scatterplots that represent the relationships between three variables.

The prototype in this study, called *Parbat*, adopts these different representation forms to facilitate visual classification (figure 2.1). The initial geoview in *Parbat* is an image display with a colour composite of three image bands or a single image

band in grey-scale. It contains two windows: the main image window with a size of 500 by 500 pixels and a pan window if the image is larger than the main window size. The image display provides basic image exploration functionalities such as an enhancement tool for contrast stretching, a zoom tool (with a variable zoom factor) floating over the main image window, and a geographic brushing tool to derive information about pixel reflectance values or digital numbers (DN) and geographic location (figure 2.1(a)).

The parallel coordinate plot (Inselberg, 1985; Inselberg, 1998) offers a technique by which a multidimensional space can be visualised in two dimensions. In *Parbat*, the *Parvis* parallel coordinate plot designed and implemented by Ledermann (2004) is adopted (Hauser et al., 2002). All image bands are plotted in the parallel coordinate plot (PCP). Axes can be reordered, scaled and translated by simple drag operations. Records can be selected in the display by dragging over them with a ‘brush’. Individual pixels can be selected and their signature and a DN-value label can be displayed on each axis. Since real-time high quality rendering of large datasets, like remotely sensed imagery, can become very time consuming, the PCP provides the user with a fast preview rendering of the data. On each axis, a transparent histogram can be plotted to obtain information about the mean DN-value and variance per band for better understanding of the data density (figure 2.1(c)).

The 3D feature space plot (figure 2.1(b)) is generated from three image bands. These bands can be selected from the colour composite in the image display, from the PCP based on their histograms, or any of the bands in the image. The unit on the axis in the 3D plot is reflection in digital numbers ranging from 0 to 255. Initially, all pixels are plotted in the 3D plot as small dots. In this mode, individual pixels cannot be selected. For selection purposes, the user can choose to plot small (grey) spheres that represent pixel values. If the image contains more than 2000 pixels, the pixels are sampled from the image either randomly or on a regular grid. To display the scatter cloud more accurately the user can also choose to calculate and visualise a density plot, in which the values of the 2000 most frequent occurring pixels are displayed. The pixel spheres are coloured according to their frequency using a grey scale with bright values as the most, and dark values as the least occurring pixel value. To explore the location of pixels in feature space the 3D plot can be navigated by (auto-)rotation, translation and zoom. Individual pixels can be selected to derive their DN-values. When a pixel is selected, it is highlighted and it flashes for five seconds to attract attention, its value is shown in the plot window. The position of the view changes automatically to an optimal location. Band names and DN-labels are shown on the three axes in the plot.

The 3D feature space plot is dynamically linked with the image display, i.e. the result of a selection in one view is also shown in other views by highlighting and the views are updated upon user action. In the image display, the selection colour used for highlighting a selected pixel can interfere with the original pixel colours in the image, therefore, selection colours can be changed in both views.

## 2.5 Visualisation of classes

An important step in a supervised classification is the choice of reference pixels (also known as regions or areas of interest) for the representation of different land cover classes. Usually, reference pixels are identified in the image or derived from external data like aerial photography or field observations. Groups of class reference pixels represent a land cover class. These pixels can be imported and visualised in the image display in their unique class colour. Statistical information from these reference pixels, like minimum and maximum values, mean vector and (co) variance matrix, is used in many classification algorithms.

The focus of this study is to develop an interactive visual fuzzy classification based on the visualisation of these reference class clusters in the 3D feature space plot. The user can add all reference classes or individual classes to the 3D plot. These class clusters are depicted by (semi-transparent) spheres, coloured according to their class colour. (figure 2.2). The centroid of a sphere (i.e. position in the 3D plot) is based on the mean vector of the class reference pixels. Initially, the radius of a sphere is based on two times the maximum standard deviation. Lighting and shading is applied to improve visibility of pixels, and class spheres and to facilitate the '3D feel'. Moreover, transparency can be changed interactively so that pixels inside the spheres become visible. Class overlap is clearly visible in places where spheres intersect (figure 2.2). Class spheres can be selected, showing a pop-up window with information about class label, class colour, mean DN-value in each band and maximum standard deviation (i.e. sphere radius). Exploration of this 3D plot provides valuable information about classes, class overlap and pixel positions. By selecting a pixel in the 3D plot inside or outside one of the spheres, a user can explore the geographical locations of pixels with the selected value highlighted in the image display. In addition, when a pixel is selected in the image a user can see whether or not it is included in a class cluster. The distance in feature space between a pixel and a class cluster or centroid reveals much information about its uncertainty. Additionally, when a pixel is located in between class spheres, uncertainty is most likely high. Especially, in the regions where class

## 2.5. Visualisation of classes

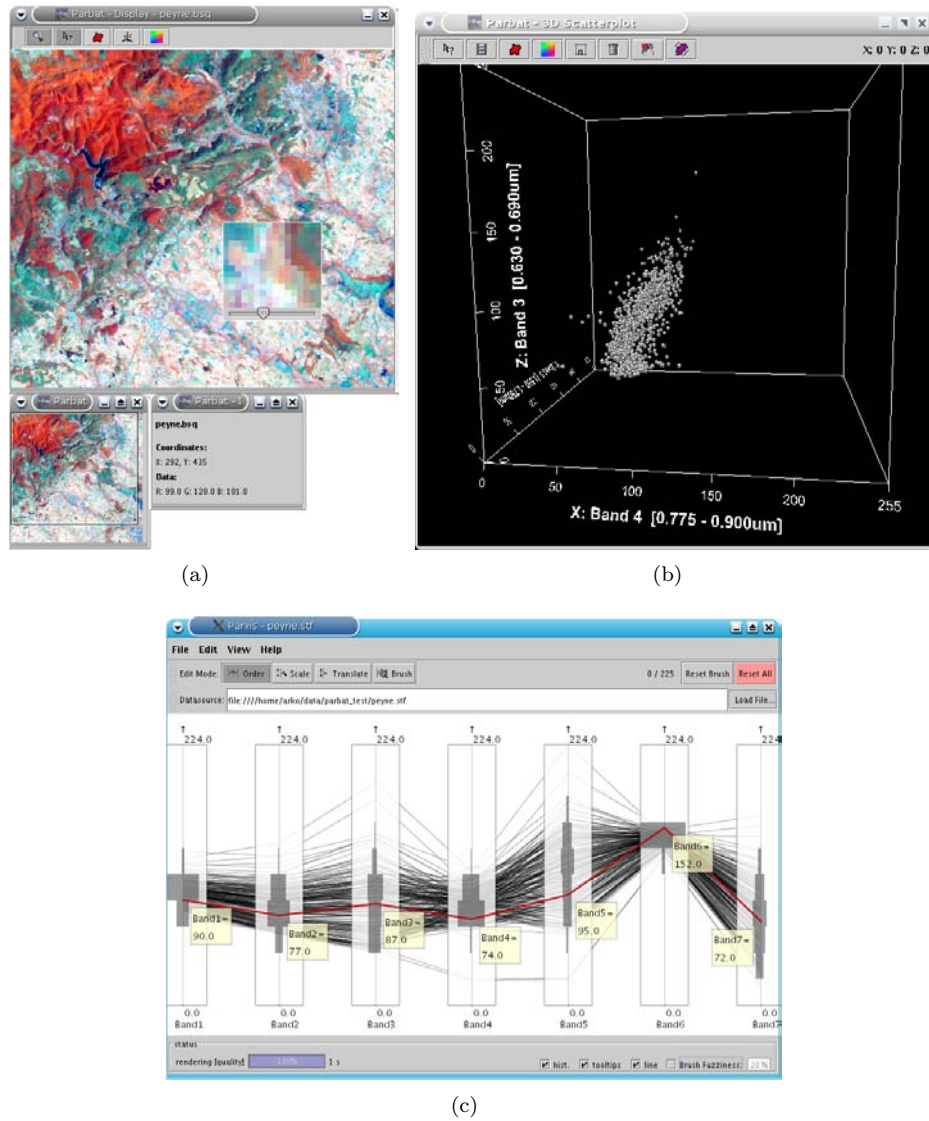


Figure 2.1: Three main visualisations: (a) Image display with a colour composite of band 4, 5 and 3 of a Landsat 7 ETM+ image; (b) 3D feature space plot shows the scatter cloud of pixels. The 3D plot can be linked to the image display in figure 2.1(a); (c) The parallel coordinate plot (PCP) shows the signatures of pixels in all seven bands.

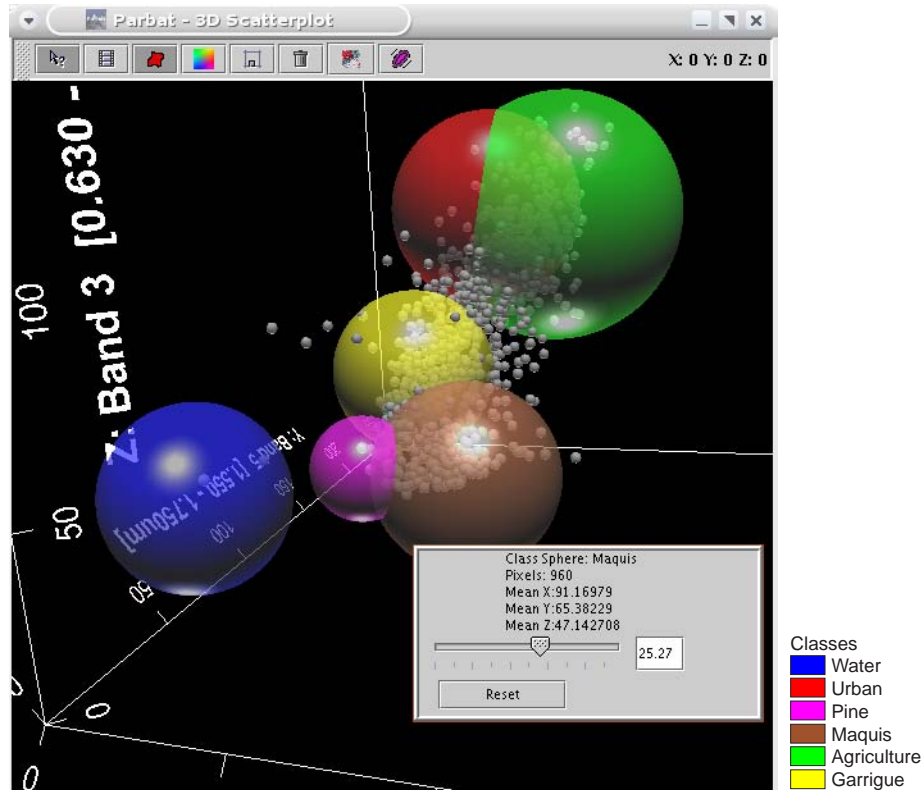


Figure 2.2: 3D feature space plot showing the class spheres of the reference classes. Overlap occurs between class maquis and pine, maquis and garrigue, and agriculture and urban. The class sphere of the maquis class is selected. The pop-up window shows the class label, colour, the number of pixels in the reference area, the mean value in each of the bands and the radius of the class sphere. The value of a selected pixel and the number of pixels in the image with the selected value are shown in the upper-right corner of the plot window. These image pixels are highlighted in the image display.

spheres overlap uncertainty values are high. The position and radius of the class spheres provide an initial condition for a fuzzy classification of the image with the spheres representing fuzzy membership functions. Interaction with these spheres could improve a classification and could help to fine-tune a classification result and discover relations between feature space, a thematic map, and an uncertainty map.

## 2.6 Visual fuzzy classification

The class spheres are used to define the membership functions for a fuzzy classification. In traditional fuzzy classification, the fuzziness parameter is set to a specific value. This decision is often relatively arbitrary. In addition, in a semantic import model the membership function is seldom based on well-founded data. Therefore, it can be argued that visual information on class overlap and class range is invaluable for determining the width and overlap of membership functions.

In *Parbat* a membership function is depicted by a class sphere, with the centroid as the point where membership equals 1.0, and the outside of the sphere itself is the point where membership equals 0.0, corresponding to a triangular membership function. Pixel membership values range between 0.0 (sphere) and 1.0 (centroid) in the area inside the sphere (figure 2.3). The initial radius of a sphere (width of the membership function) is based on two times the maximum standard deviation of the class under consideration. When the user selects a class sphere he or she is presented with a pop-up window with information about the class label, colour, mean values and the radius. The radius can be adjusted with a slider, increasing or decreasing the size of the sphere. The exact value for the radius of the changing sphere is shown in the pop-up window. By changing the radius of a class sphere, the user changes the width of the triangular membership function of a class (figure 2.3). Class overlap zones can be resized to increase or decrease the fuzziness, effectively changing the fuzziness parameter in a fuzzy *c*-means classification for those particular classes.

When all membership functions are adjusted based on the visual interpretation of class spheres, all unclassified pixels in the image can be classified. First, the user has to decide on the type of output products of the classification. Users are likely to be interested in a crisp classification product to see the spatial distribution of classes in the image or to see a generalised, classified version of the image. Therefore, a hard (i.e. ‘defuzzified’) land cover image is one of the main outputs of the classification, providing class labels and class colours for each pixel (figure 2.4(a)). A membership image with a membership layer for each class is the second product (figure 2.4(b)). Information about transition zones can be obtained from these membership images. A third output is an image depicting the maximum membership per pixel. This image gives an indication of the uncertainty of the classification; the lower the maximum membership, the higher is the uncertainty (figure 2.4(c)). Another powerful measure to depict uncertainty is the confusion index (*CI*) (Burrough and McDonnell, 1998) as a value for class vagueness of a membership vector.

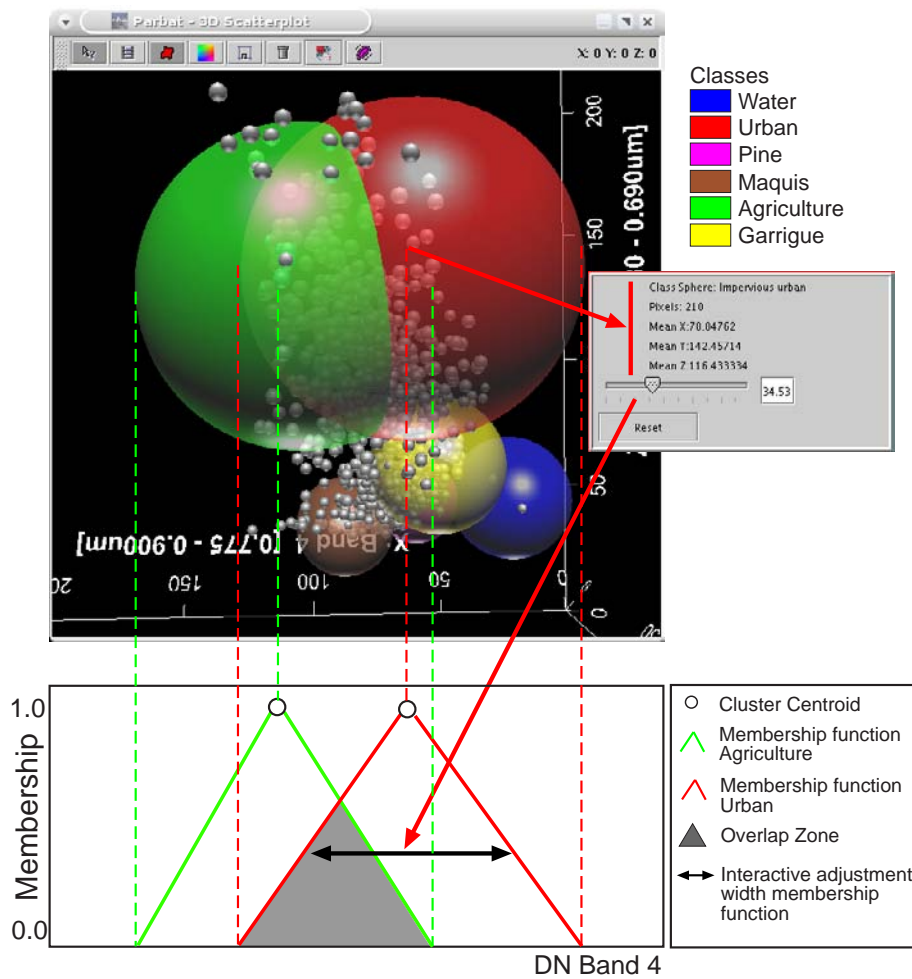


Figure 2.3: Representation of an interactive visual fuzzy classification. The classes agriculture and urban overlap in the 3D feature space plot. The class spheres depict triangular membership functions that are used for classification. The membership functions of the two overlapping classes are projected onto band 4 for clarification of the process. A popup slider is used to adjust the radius of the sphere, thereby changing the width of the membership function and possibly changing the overlap with another class/membership function.

$$CI = \frac{\mu_{max}^2}{\mu_{max}} \quad (2.2)$$

As a final output, an image with the confusion index is produced. This image gives an excellent overview of the areas where uncertainty is highest and classes overlap (figure 2.4(d)). When the actual classification is performed, the selected classification outputs are shown on screen and automatically linked to the 3D feature space plot. Pixels that fall outside any of the class spheres are unclassified. They are shown in black in the hard class image (figure 2.4(a)). The resulting image displays have the same functionality as the original image display. The user can navigate, zoom and query pixels in the image (see also figure 2.1(a)).

The dynamic links between the class image display and the 3D plot are very powerful. These links give the user the possibility to explore and discover relations between the class of a certain pixel, its uncertainty and the location in feature space. Based on the visual information a user can get a good indication of areas with high uncertainty and its origin. Insight into the actual classification can be improved, because the user can ‘play’ with the parameters of the algorithm by adjusting the class spheres in feature space. The new result is shown as a class image with related uncertainty information. Changes in class membership functions are immediately depicted in the output images. The user will get a better feel of the functioning of a fuzzy classification. Another advantage of this tool is that it enables a user to fine-tune the classification result.

## 2.7 Implementation of the prototype *Parbat*

The visualisation and classification techniques described above were implemented in the software prototype *Parbat* (<http://parbat.lucieer.net> (Lucieer, 2004)). The user interface contains a series of buttons to access the main visualisation and classification functions, similar to commercial image processing software like ERDAS Imagine and ENVI. Selection dialogs and displays are opened in new windows. Thus, *Parbat* implements a multiple document interface (MDI) without backing window; the main window is the button bar (figure 2.5). Currently, *Parbat* can read band sequential files based on the standard ENVI format. Both input and output functions use this file format. A band sequential file (often with the extension .bsq) is a generic binary file with an ASCII header describing the number of rows, columns, bands, band names, data type, projection, and sensor. Reference pixels for classification are selected from regions of interest (ROIs) digi-

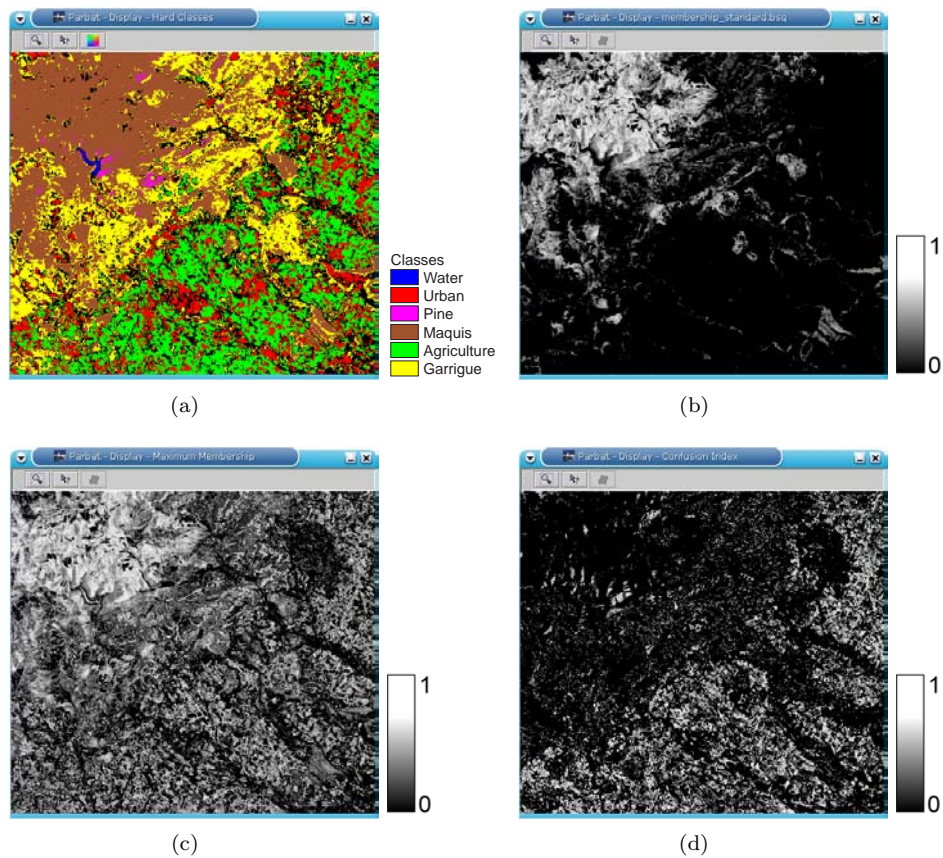


Figure 2.4: Classification result after an initial visual fuzzy classification based on default radii of the class spheres: (a) Crisp land cover class image display with class labels based on maximum membership. Black pixels are unclassified. These unclassified pixels occur outside any of the class spheres in the 3D feature space plot; (b) Membership image display for the class maquis shows high membership values for pixels in the Northwest, hilly part of the area; (c) Maximum membership map shows, for every pixel, the maximum membership value from the membership vector. The maquis and water pixels are classified with low uncertainty and maquis, urban and agricultural areas with higher uncertainty values; (d) Confusion image display shows areas where confusion in classification occurs (bright areas). Urban and agricultural areas overlap in feature space, as can be seen in figures 2.2 and 2.3. Pixels in this overlap zone show high confusion values in the image display (note: high uncertainty = high confusion = bright value).

## 2.7. Implementation of the prototype Parbat

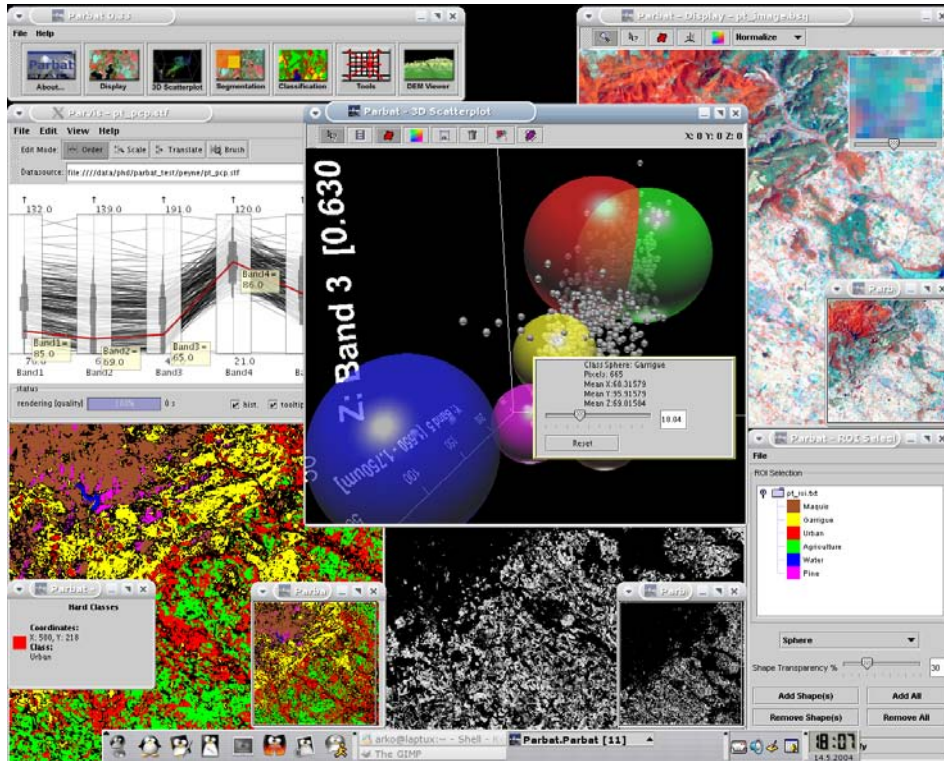


Figure 2.5: *Parbat* prototype, showing several selection, information and display windows.

tised in ENVI. The ENVI ROI ASCII export format is used as input in *Parbat* for visualisation of reference class pixels in the image display and class spheres in the 3D plot. Information about these ROIs is used in subsequent classification.

Currently, this prototype is tested and run on a Pentium III 800MHz laptop with 512Mb RAM and a video card supporting OpenGL running a Linux operating system (*Parbat* can also be run on MS Windows and other operating systems). Java 3D utilises OpenGL in the background and a video card supporting this 3D graphics standard greatly enhances 3D visualisation performance. A visual fuzzy classification based on three bands of an image of 512 by 512 pixels takes less than three seconds on this machine. Navigation of both the image display and 3D feature space plot is fast and smooth, without jittering.

## 2.8 Prototype test case

### 2.8.1 Study area and data set

In order to test the prototype, a subset of a Landsat 7 ETM+ image of an area in Southern France was used. Transition zones between vegetation types are known to be problematic in land cover classification of remotely sensed images (Foody, 1996). Therefore, classification uncertainty plays an important role in these images. A geovisualisation tool like *Parbat* can help to gain insight into classification uncertainty. An area in which these classification problems occur is the ‘La Peyne’ catchment located Northwest of Montpellier, France. This area was chosen as a study area to demonstrate the use of a geovisualisation tool for visual fuzzy classification and uncertainty. The area is situated at the fringe of the ‘Massif Central’ and is characterised by various geological and lithological substrates. The large variety in these substrates has caused a wide range of soil conditions and vegetation types. The northern part of the area is covered by a Mediterranean oak forest (also known as ‘maquis’) dominated by *Quercus ilex* and *Quercus pubescens* and lower ‘garrigue’ shrub lands. The southern part of the area is characterised by vineyards and agricultural crops (Lucieer et al., 2000; Sluiter, 2004). A subset (225 km<sup>2</sup>) of a Landsat 7 (ETM+) scene covering the ‘La Peyne’ area is used in this study (figure 2.6). The image was acquired on June 26<sup>th</sup>, 2001.

The study area is actively used as a research area for modelling floods, erosion, evapotranspiration, and soil temperature. Information on basic land cover provides important input for these models. The following land cover classes can be found in the study area: water (lake), maquis, garrigue, pine forest, agriculture (mostly vineyard) and urban area. Not all classes are likely to have similar spectral responses and overlap. Water, for example, is often a spectrally ‘pure’ class and usually does not overlap with other classes. However, maquis and garrigue were expected to show very similar signatures with significant overlap of clusters in feature space. Fieldwork showed that these classes often gradually change from one to the other. Urban areas are often a mix of roofs, gardens, cars and streets. Thus, the urban class would probably show a high variance in its class cluster in feature space. The same applied to vineyards, characterised by a mix of vegetation and bare soil, with the percentage of vegetation cover depending on the season.

Fieldwork was carried out to obtain ground reference data. Regions with ‘pure’ classes have been observed in the field and corresponding pixels digitised and extracted from the image to form reference class clusters. The mean and standard deviation from these class reference pixels was then used to plot the class spheres

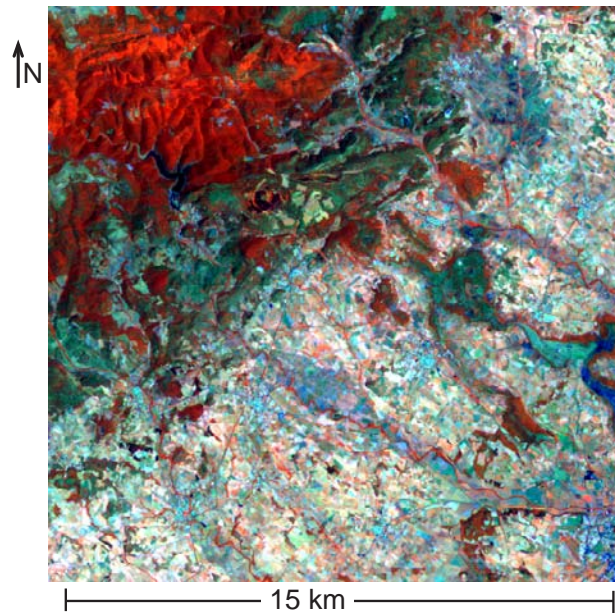


Figure 2.6: Colour composite of band 4,5, and 3 of a subset of a Landsat 7 ETM+ image of the 'La Payne' catchment in southern France.

in the 3D feature space plot. Additionally, the reference areas were highlighted in their class colour in the image display. Individual classes could be added or removed from the 3D plot or image display. The locations and sizes of the class reference spheres in the 3D plot provided an initial setup for the fuzzy classification. Before the actual classification, a user is stimulated to explore overlap zones between classes by navigation in the 3D plot and to explore relations between pixels in the 3D plot and pixels in the image display and their distance to the class reference clusters.

### 2.8.2 Visual fuzzy classification of the study area

To test the visual fuzzy classification in the prototype, band 4 (NIR), 5 (MIR) and 3 (RED) from the Landsat 7 test image were used. These three bands explained most of the variability in the image and were expected to give good classifica-

Table 2.1: Classification accuracy % for a classification based on the *initial* class sphere configuration

Class	Reference						
	Maquis	Garrigue	Urban	Agriculture	Water	Pine	Total
Unclassified	31.19	5.63	8.61	12.79	0.00	3.91	14.30
Maquis	68.81	0.00	0.00	0.00	0.00	0.00	16.75
Garrigue	0.00	94.37	0.00	0.33	0.00	0.00	23.57
Urban	0.00	0.00	91.39	34.92	0.00	0.00	21.76
Agriculture	0.00	0.00	0.00	51.97	0.00	0.00	17.08
Water	0.00	0.00	0.00	0.00	100.00	0.00	3.23
Pine	0.00	0.00	0.00	0.00	0.00	96.09	3.31
Total	100.00	100.00	100.00	100.00	100.00	100.00	100.00

tion results. When the reference class spheres were plotted, it could be observed that classes agriculture and urban overlapped considerably (figures 2.2 and 2.3). In addition, the maquis and garrigue class spheres, as well as the maquis and pine classes overlapped slightly. The water class sphere showed no overlap with other classes. An initial classification with the default membership functions (note that the default sphere radius equals two times the maximum standard deviation) showed that many pixels remained unclassified (figure 2.4(a)). This was caused by the small width of the membership functions. A confusion matrix from an accuracy assessment (table 2.1) showed that the urban class was over-classified and the agricultural class was under-classified, compared to what has been observed in the field. This initial classification had an overall accuracy of 72.12% (table 2.4). Furthermore, the image display with the confusion index visualised the spatial distribution of uncertainty (figure 2.4(d)). It showed that there was considerable confusion in agricultural and urban areas. In addition, in regions affected by shadow, confusion was high. This observation corresponded to the overlapping class spheres in the 3D plot. A user can explore these areas of high uncertainty by selecting a pixel with high confusion in the confusion image display and study the position of this pixel in the feature space plot (it is highlighted, it flashes and the position of the viewer changes to the optimal location). This exploration session showed that pixels with a high confusion index (i.e. high uncertainty) were located in the overlap zones between classes urban and agriculture. The maximum membership image display showed that in areas where maquis and water occur membership was highest, and therefore, uncertainty values were low (figure 2.4(c)). When pixels in these areas in the image display were selected, it could be observed that these pixels were located inside the maquis and water class spheres in the 3D plot, close to the centroids, therefore with high membership values.

Table 2.2: Classification accuracy % for a classification based on the *adjusted* class sphere configuration

<i>Class</i>	<i>Reference</i>						
	Maquis	Garrigue	Urban	Agriculture	Water	Pine	Total
Unclassified	10.07	0.00	7.89	2.95	5.00	0.78	4.50
Maquis	89.93	0.54	0.00	0.00	0.00	3.12	22.14
Garrigue	0.00	99.46	3.83	15.90	0.00	0.00	30.38
Urban	0.00	0.00	50.48	0.57	0.00	0.00	5.87
Agriculture	0.00	0.00	37.80	80.57	0.00	0.00	30.73
Water	0.00	0.00	0.00	0.00	95.00	0.00	3.07
Pine	0.00	0.00	0.00	0.00	0.00	96.09	3.31
Total	100.00	100.00	100.00	100.00	100.00	100.00	100.00

### 2.8.3 Fine-tuning the visual classification

To fine-tune the classification a user can go back to the 3D plot to reconfigure the class spheres based on a previous exploration session (figure 2.7). In the previous session, a considerable amount of pixels was unclassified because these pixels did not fall within any of the class spheres, therefore their membership was equal to 0. The first step of the fine-tune session was to increase the width of some of the membership functions (figure 2.3). The radius of the garrigue class sphere could easily be increased without making the overlap zone with maquis too large. The width of the urban class could be reduced, since it was over-classified in the initial classification. This class sphere was selected in the 3D plot and its radius decreased with the slider. The agriculture class sphere was resized to a larger size, because it was under-classified in the initial classification. See figure 2.7(a) for the resulting class sphere configuration. A second classification based on this configuration showed that most of the unclassified pixels in the previous session were classified (figure 2.7(b)). The area of the urban class was much smaller, corresponding with the small number of villages observed in the area, and the accuracy values for the maquis, garrigue and agriculture class increased (table 2.2). The confusion image display showed that confusion was highest in narrow transition zones between maquis and garrigue and in agricultural parcels (figure 2.7(d)). These parcels are most likely bare soil patches that are spectrally very similar to roofs of houses in the urban area. A selection of pixels in these areas showed that these pixels were located in the overlap zone between the agriculture and urban classes in the 3D feature space plot. The overall classification accuracy was 85.16% (table 2.4).

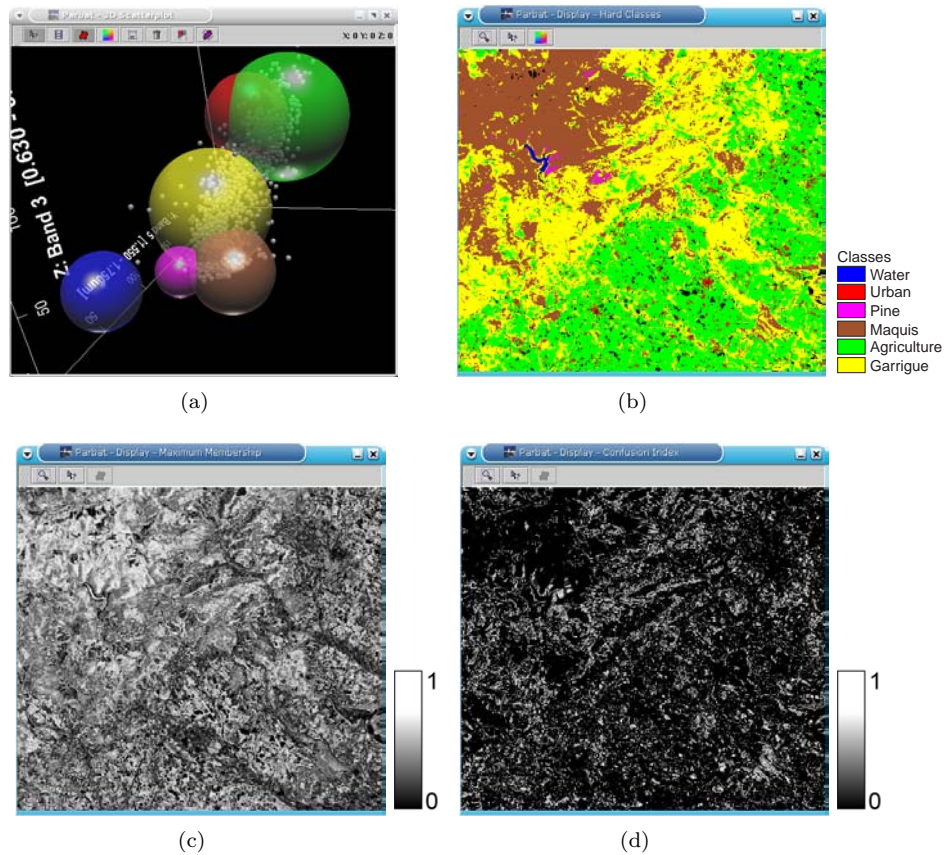


Figure 2.7: After an initial classification the classification result was fine-tuned by adjusting class sphere radii: (a) 3D plot with the adjusted class spheres; the sizes of the maquis class sphere, as well as the garrigue and agriculture class spheres increased. The radius of the urban class sphere decreased. This configuration of class clusters better reflects the situation in the field; (b) The revised 'defuzzified' (crisp) land cover map; (c) The maximum membership values for every pixel; (d) The confusion index for every pixel.

Table 2.3: Classification accuracy % for a classification based on an *adjusted* class sphere configuration of the first three Principal Components

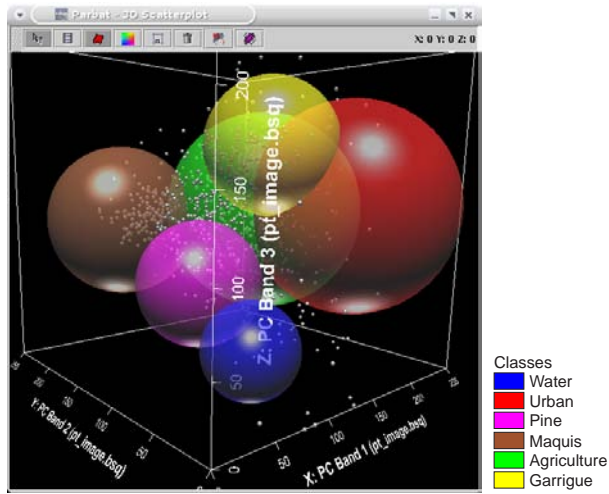
Class	Reference						
	Maquis	Garrigue	Urban	Agriculture	Water	Pine	Total
Unclassified	0.11	0.00	27.99	6.80	12.50	0.00	5.82
Maquis	99.89	0.11	0.00	0.00	0.00	0.00	24.35
Garrigue	0.00	96.42	5.50	6.31	0.00	3.91	26.80
Urban	0.00	0.00	53.35	2.21	0.00	0.00	6.73
Agriculture	0.00	2.60	13.16	84.67	0.00	0.00	29.95
Water	0.00	0.00	0.00	0.00	87.50	0.00	2.83
Pine	0.00	0.87	0.00	0.00	0.00	96.09	3.53
Total	100.00	100.00	100.00	100.00	100.00	100.00	100.00

#### 2.8.4 Visual classification based on Principal Components

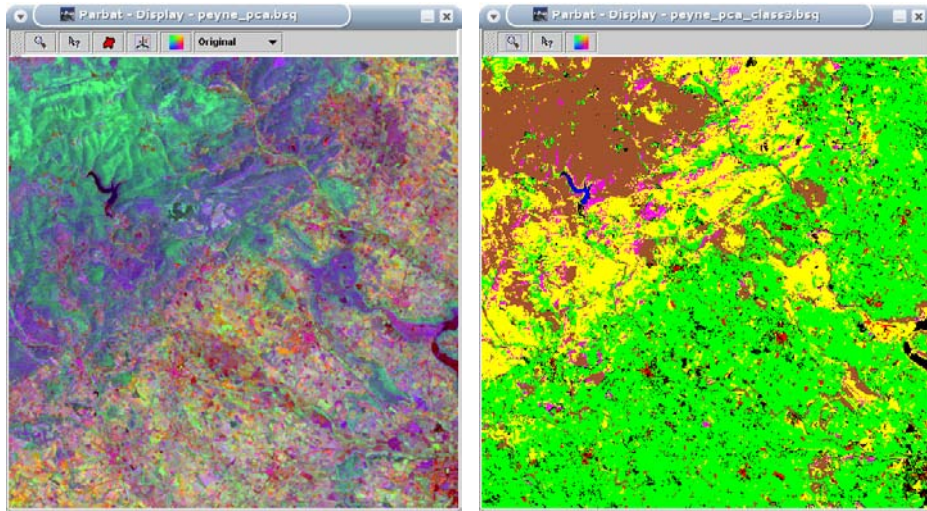
The visual classifier as proposed in this study is based on three image bands. These bands are chosen from all image bands, based on interpretation of the parallel coordinate plot and colour composites in the image display. In other words, only three dimensions of a seven dimensional feature space (in case of a Landsat 7 ETM+ image) were used. Alternatively, dimensionality reduction techniques could be applied to reduce a seven dimensional space to three dimensions. In this example, a Principal Component Analysis (PCA) was carried out to derive the three principal components that explain most variance in the data. These first three PC bands explain 99% of the total variance in seven original bands. The axis of the 3D plot were then formed by these first three principal components (figure 2.8(a)). Likewise, the image display contained a colour composite of these principal components (figure 2.8(b)). A visual fuzzy classification was then carried out in principal component space. The classification result is shown in figure 2.8(c). Table 2.3 gives the confusion matrix for this classification. It shows that almost no under-classification or over-classification occurred. The overall accuracy was 88.26%.

#### 2.8.5 Visual classifier versus standard fuzzy classifiers

Table 2.4 and figure 2.9 show that the visual classifier outperformed the standard supervised fuzzy classifiers (SFCM). In general, all standard fuzzy classifiers over-classified the urban area, i.e. too much urban area occurred in the classification result (figure 2.9(a)). Four supervised fuzzy classifiers (SFCM) were compared to the visual classifier. A fuzzy overlap parameter of 2.0 was used for all classifiers.



(a)



(b)

(c)

Figure 2.8: Visual fuzzy classification of Principal Component space with the first three Principal Components: (a) 3D Principal Component space with class spheres; (b) Image display with colour composite of the first three Principal Components; (c) PCA fuzzy visual classification.

Table 2.4: Classification accuracy assessment for different classifiers

Classifier	Bands	Distance	Accuracy %	Kappa
<i>Visual Classifier</i>	3, 4 and 5	original spheres	74.12	0.68
<i>Visual Classifier</i>	3, 4 and 5	adjusted spheres	85.16	0.81
<i>Visual Classifier</i>	3 PCA	adjusted spheres	88.26	0.85
SFCM	3, 4 and 5	Euclidean	68.13	0.61
SFCM	3, 4 and 5	Mahalanobis	63.50	0.56
SFCM	all	Euclidean	68.50	0.61
SFCM	all	Mahalanobis	68.15	0.61

The Euclidean and Mahalanobis distance measures gave different classification results. Additionally, the SFCM classification was carried out using the same three bands as in the 3D plot and using all bands in the image to test the effect of the number of bands. Table 2.4 shows that there was not much difference in performance between the different SFCM classifiers. Both visual classifiers outperformed the SFCM classifiers. Fine-tuning of the initial classification result improved accuracy with more than 10% to an overall classification accuracy of 84.41%. A visual classification based on the first three principal components resulted in a classification accuracy of 88.26%.

The main gain of the visual classifier, however, is the insight a user gets into the classification algorithm and related uncertainty by exploring the relations between classes and pixels and the relations between the spatial classification result (image display) and uncertainty information (confusion and maximum membership display), and corresponding thematic or spectral information in the 3D feature space plot. Dynamically linked views and interaction with the class reference spheres are, therefore, of crucial importance for the effectiveness of a visual classifier.

## 2.9 Prototype evaluation with focus groups

Evaluation is an important issue in considering the effectiveness of the prototype in improving understanding for fuzzy classification and uncertainty. Initially, a qualitative evaluation is of interest for a prototype with a focus on exploration. Focus groups provide a technique of qualitative user testing (Kessler, 2000; Morgan, 1998). Harrower et al. (2000) describe focus groups as a “cost-effective way to generate qualitative evidence concerning the pros and cons of a geovisualisation system”.

Eight researchers were invited for a two-hour focus group session. The partic-

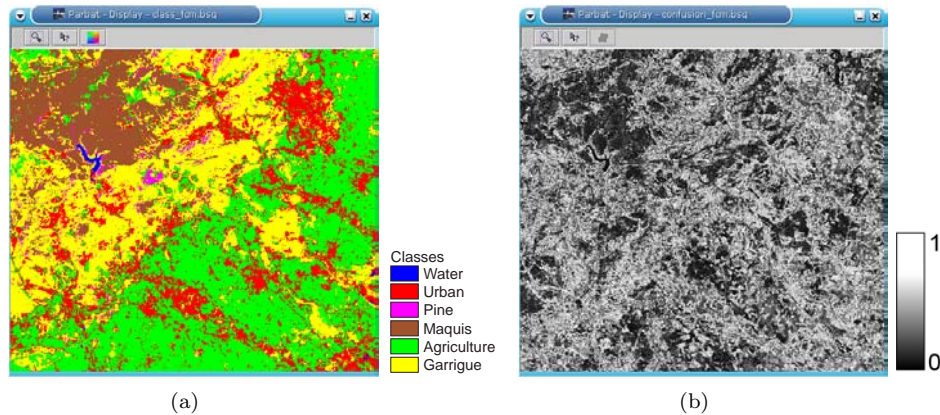


Figure 2.9: Standard supervised fuzzy  $c$ -means classification (SFCM all bands with Euclidean distance measure and overlap of 2.0) for comparison with the fuzzy visual classifier in figure 2.7: (a) Image display with hard classes shows that the urban class is over-classified and the agricultural class is under-classified; (b) Image display with the confusion index for the standard fuzzy  $c$ -means, which depicts high confusion values in agricultural, urban and garrigue areas.

ipants all had an academic background in remote sensing or visualisation. The session was started with a 20-minute presentation about the background of fuzzy classification of remotely sensed imagery and about geovisualisation. Then, the prototype was demonstrated by showing the different displays and their basic functionality, followed by a visual fuzzy classification based on class clusters in the 3D feature space plot. Next, the participants worked with the prototype for 45 minutes with clear directions to focus on the visual fuzzy classifier. Finally, their experiences were discussed in a 40-minute session.

All participants felt that the visualisation tool helped in understanding a classification algorithm. Dynamic linking of the different representations greatly improved their insight. The 3D plot provided an excellent visualisation for classification. Interaction with the class clusters helped in understanding the effect of changing membership functions and class overlap on the classification and uncertainty. Some participants noted that a tool like this would be very helpful in teaching students on remotely sensed image classification, to help them visualise the classification process.

One of the mentioned disadvantages was that the role of the parallel coordinate plot is small in this prototype. The PCP helps in choosing bands for the 3D plot

(based on the histograms); however, the PCP is not linked to the image and 3D plot, therefore, it is difficult to use it in classification. A dynamic link of the PCP with the other displays would be an improvement. Another disadvantage is the shape of the class spheres. It might falsely suggest equal variance in every band and it implies a very ‘smooth’ class shape. Some classes can be very irregularly shaped and visualisation of these exact class shapes could be useful. Therefore, one should not compare the shape of a class cluster with the shape of a sphere, representing a membership function in 3D feature space.

The classification products like the confusion and maximum membership image displays provided a good overview of the geographical distribution of uncertainty in the classification. Detailed exploration of individual pixel values provided good insight into thematic pixel uncertainty. The prototype is not restricted to one type of application, like land cover mapping. In other applications like geological, soil or vegetation mapping, a tool like this might be very useful and helpful. In addition, the prototype is not restricted to one type of remotely sensed imagery. One of the main complaints about existing software was that ‘uncertainty tools’ are lacking in commercial remote sensing and GIS packages. *Parbat* bridges the gap between classification and uncertainty visualisation.

It can be concluded from this focus group session that the prototype complies with the objectives. Although, some detailed aspects of the user interface and functionality could be improved, the main objective of the prototype was clear. All participants found that the proposed geovisualisation prototype helped in clarifying the functioning of a supervised fuzzy classification algorithm. It also helped in understanding uncertainty and fuzzy class overlap.

## 2.10 Discussion

A Landsat ETM+ image contains seven bands; other sensors, like hyperspectral sensors, produce up to hundreds of bands. Choosing the three bands that describe most of the variance for the application at hand is a difficult task. Several techniques exist to reduce a multi-dimensional space to three dimensions. In this study, a principal component analysis was applied to reduce the dimensionality of the data. Alternatively, a projection of a hyper-dimensional feature space to three dimensions could be used. Other examples for dimensionality reduction techniques include projection pursuit, multi-dimensional scaling, self organising map (SOM), or other statistical techniques like a discriminant analysis. The visual classification results show, however, that dimensionality reduction technique like a principal

components analysis only improve overall accuracy with a small percentage. Other visualisation techniques for visualisation of hyper-dimensional spaces exist, for example the hyperbox or starplot. However, these techniques are not suitable for classification purposes.

The membership function used in *Parbat* is a triangular shaped function. A useful addition to the prototype would be an option to choose the shape of the membership function, either globally or per class. For example, the user should be able to select a trapezoidal or Gaussian membership function. This makes it possible to assess the effect of different membership functions on the classification result. Additionally, the centroids of the class spheres (i.e. centre of the membership functions, where membership equals 1.0) are fixed. A user might want to change the location of a class sphere to assess the effect of relocation of reference class clusters on fuzzy overlap for example.

Class clusters in the 3D feature space plot are visualised by semi-transparent spheres. However, a sphere is a very rough approximation of the shape of a class cluster. By using a sphere, one assumes equal variance in every direction. In fact, the maximum standard deviation of the three bands is used to set the radius of a class sphere. A better approximation of the shape of a class cluster would be an ellipsoid. A 3D ellipsoid could be constructed from the mean vector and covariance matrix of a class. The mean vector provides the centre of the ellipsoid and from the covariance matrix, eigenvalues and eigenvectors can be calculated. Eigenvalues represent the length of the axes; eigenvectors represent the direction of the axes of an ellipsoid. In this way, for every reference class ellipsoids can be constructed and visualised. However, an ellipsoid is also an approximation of the shape of a class cluster. Evaluation of the prototype showed that users would like to see the 'real' shape of a class clusters in feature space. They argued that it would help in the interpretation of reference classes and assessing their overlap.  $\alpha$ -shapes provide a technique for calculating a shape from a set of points in feature space. Therefore,  $\alpha$ -shapes provide a way of visualising irregular and even concave shaped clusters in a 3D feature space plot. In the next chapter,  $\alpha$ -shapes will be discussed.

Visualisation of uncertainty in the final classification result is done by depicting maximum membership or confusion values in a separate grey-scale map. Alternatively, the map containing hard land cover classes can be combined with the uncertainty map. Colour hue can be used to describe the classes and colour saturation or lightness can be used to visualise uncertainty information. One of the visualisation techniques as described in section 2.3 could be used to present the final classification result combined with uncertainty information. The focus of this study, however, is on explorative visualisation of a fuzzy classification and not on

presentation of uncertainty in a classification result.

The effectiveness of the geovisualisation tool not only depends on the visualisation techniques used but also on the knowledge of the user (a geoscientist). The selection of reference or ground truth pixels is an important step in the classification process. Sufficient knowledge of the area under consideration is essential for good classification results.

## 2.11 Conclusions

Uncertainty plays an important role in land cover classification of remotely sensed imagery. Classification of areas where transition zones between vegetation types occur, usually results in high classification uncertainty. Fuzzy classification provides a technique for quantifying this uncertainty. Visualisation provides an excellent means of exploring the functioning of a fuzzy classification algorithm and related uncertainty. In this study, a geovisualisation tool was proposed and discussed. With this tool a geoscientist can visually interact with the parameters of a supervised fuzzy classification algorithm. The user can find an optimal classification result and derive insight into classification uncertainty. The tool consists of three basic plots: an image display, a parallel coordinate plot, and a 3D feature space plot. The user can interactively adjust the membership functions of classes and fuzzy overlap zones in the 3D feature space plot. All plots are dynamically linked and have geographic brushing functionality to stimulate exploration and, consequently, improve insight into classification and uncertainty. To test the proposed prototype, a Landsat 7 ETM+ image of an area in Southern France was used. In this area, transition zones between semi-natural vegetation types dominate. A visual fuzzy classification resulted in a hard land cover map and uncertainty maps, showing membership layers, maximum membership per pixel and the confusion index per pixel. The user can adapt reference class spheres in the 3D feature space plot to fine-tune the classification. Good classification results were obtained with an overall classification accuracy of 85.16%. A visual fuzzy classification in 3D principal component space, provided good classification results with an overall accuracy of 88.25%. A focus group user test showed that remote sensing users find the described visualisation techniques very valuable. Users noted that the main advantage of the visual classifier is an improvement of insight into the classification algorithm and related uncertainty. Exploring the relations between classes and pixels and the relations between the (crisp) classification result and uncertainty information, and corresponding thematic or spectral information

in the 3D feature space plot provides important information for understanding a fuzzy classification and related uncertainty.

## 2.11. Conclusions

---

## Chapter 3

# Alpha-shapes for Visualisation and Classification\*

*There are some minds like either convex or concave mirrors,  
which represent objects such as they receive them,  
but never receive them as they are*

J. Joubert

### 3.1 Introduction

In chapter 2, a new interactive visualisation tool for visualising a fuzzy classification of remotely sensed imagery was proposed. Lucieer and Kraak (2002) and Lucieer and Kraak (2004) focused on visual exploration of a fuzzy classification algorithm and interaction with its parameters. A geovisualisation tool together with a supervised fuzzy classification algorithm was implemented to demonstrate the use of exploratory visualisation techniques in assessing classification uncertainty.

---

\*This chapter is based on the following paper:

Lucieer, A. and Kraak, M. J. (2004a). Alpha-shapes for visualising irregular shaped class clusters in 3D feature space for classification of remotely sensed imagery, *Proceedings Visualisation and Data Analysis 2004, San Jose, USA*.

---

This tool allowed a geoscientist to interact with the parameters of a fuzzy classification algorithm by adjusting fuzzy transition zones between classes in a 3D feature space plot. The purpose of this tool was to improve a geoscientist's understanding of uncertainty in remotely sensed image classification. Good classification results were obtained with visual fuzzy classifications.

Class clusters in the 3D feature space plot were visualised by semi-transparent spheres. A sphere is a very rough approximation of the shape of a class cluster. By using a sphere one assumes equal variance in every direction, however, often this is not the case. Evaluation of the software prototype revealed that users would like to see the 'real' shape of a class cluster in feature space, because it would help in interpretation of reference classes and assessing their overlap.  $\alpha$ -shapes provide a way of visualising irregular shaped clusters in 2D and 3D space.

The aim of this chapter is to propose and implement  $\alpha$ -shapes for visualisation of reference class clusters.  $\alpha$ -shapes are expected to improve visualisation of class clusters in a remote sensing image classification, therefore, it is argued that  $\alpha$ -shapes will also improve insight into classification and related uncertainty, providing a way of visualising class clusters more accurately. The position of an unclassified pixel in feature space in relation to one or more reference classes (i.e.  $\alpha$ -shape of a cluster of reference pixels) can be assessed more accurately. Uncertainty arises from vagueness in the attribution of classes to unclassified pixels and visualisation can be helpful in communicating this vagueness. The more accurate the representation of classes in feature space, the better the uncertainty assessment of a classification.

The second objective of this study is to propose and implement a classification algorithm based on  $\alpha$ -shapes. Most classification algorithms cannot cope with concave cluster shapes in feature space.  $\alpha$ -shapes can deal with irregular or even concave clusters in a classification.

## 3.2 Class cluster shape

For a supervised remote sensing classification, reference data is used. An important step in a supervised classification of remote sensing imagery is the choice of reference pixels for the representation of classes. Usually, reference pixels are selected from the image or from external data like aerial photography or field data. In this study, reference pixels are selected and extracted from the image by digitising polygons in the image display. Each polygon depicts a land cover class and

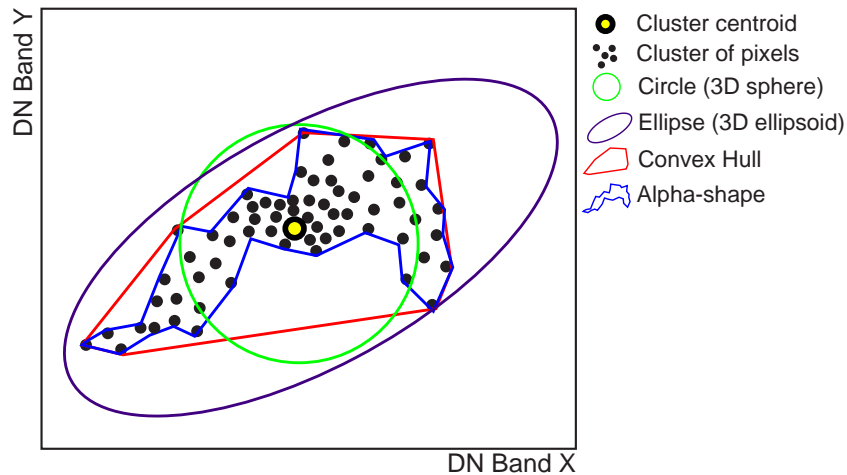


Figure 3.1: Irregular shaped cluster in a 2D feature space. Comparison of cluster representation by a circle, an ellipse, a convex hull, and an  $\alpha$ -shape.

is displayed in a unique class colour. Class statistics, extracted from the selected pixels, are used to classify all unlabelled pixels. Visualisation of class information in feature space gives a user valuable information about the location of classes and about possible overlap or vagueness between classes.

In chapter 2, spheres are plotted in the 3D feature space plot to depict reference classes. These spheres provided simple representations of class reference clusters. A better approximation of the shape of a class cluster is an ellipsoid, as it takes into account difference in variance in different bands. A 3D ellipsoid can be constructed from the mean vector and covariance matrix of a class. The mean vector gives the centre of the ellipsoid. From the covariance matrix, eigenvalues and eigenvectors can be calculated. Eigenvalues represent the length of the axes and eigenvectors represent the direction of the axes of an ellipsoid. Although an ellipsoid gives a better representation of the shape of a cluster, it is still inaccurate when a cluster is irregular with concave shaped sections.  $\alpha$ -shapes can be used to overcome this problem and to improve the visualisation of irregular shaped clusters. Figure 3.1 shows an example of a 2D feature space with a class cluster of pixels represented by a circle, an ellipse, a convex hull, and an  $\alpha$ -shape.

### 3.3 $\alpha$ -shapes

The geometric notion of ‘shape’ has no associated formal meaning. Edelsbrunner and Mücke (1994) introduced  $\alpha$ -shapes as a definition and computation of the shape of a finite point set in three-dimensional Euclidean space.  $\alpha$ -shapes can be viewed as generalisations of the convex hull of a point set. It formalises the intuitive notion of shape, and for varying parameter alpha, it ranges from crude to fine shapes. Let  $S$  be a finite set of points in  $\mathbf{R}^d$  (where  $d$  is the dimension) and  $\alpha$  a real number with  $0 \leq \alpha \leq \infty$ . The  $\alpha$ -shape of  $S$  is a polytope that is neither necessarily convex nor connected. For  $\alpha = \infty$ , the  $\alpha$ -shape is identical to the convex hull of  $S$ . However, as  $\alpha$  decreases, the  $\alpha$ -shape shrinks by gradually developing cavities. These cavities may join to form tunnels, and even holes may appear (Edelsbrunner and Mücke, 1994).

Fischer (Fischer, 2004) metaphorically describes  $\alpha$ -shapes as ice-cream containing chocolate pieces. He writes the following: “One can intuitively think of an  $\alpha$ -shape as a huge mass of ice-cream making up the space  $\mathbf{R}^d$  and containing the points  $S$  as ‘hard’ chocolate pieces. Using one of these sphere-formed ice-cream spoons we carve out all parts of the ice-cream block we can reach without bumping into chocolate pieces, thereby even carving out holes in the inside (e.g. parts not reachable by simply moving the spoon from the outside). We will eventually end up with a (not necessarily convex) object bounded by caps, arcs and points. If we now straighten all ‘round’ faces to triangles and line segments, we have an intuitive description of what is called the  $\alpha$ -shape of  $S$ .” An example for this process in 2D (where the ice-cream spoon is simply a circle) is shown in figure 3.2.

### 3.4 $\alpha$ -shape implementation and visualisation

To illustrate the proposed  $\alpha$ -shape class visualisation, the Landsat 7 ETM+ image of the ‘Peyne’ river catchment in Southern France was used (section 2.8). The following land cover classes can be found in the study area: water (lake), maquis, garrigue, pine forest, agriculture (mostly vineyard) and urban area.

$\alpha$ -shapes were implemented to improve the visualisation of the shape of these class clusters in the 3D feature space plot. For the implementation of  $\alpha$ -shapes in *Parbat*, external open-source software called *hull* was used. *Hull* was programmed in the C-programming language by Clarkson (2004). *Hull* calculates the (3D) coordinates of vertices that make up the  $\alpha$ -shape from a set of (3D) points based

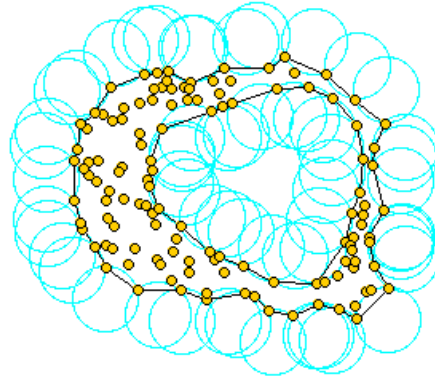


Figure 3.2: Example of a 2D  $\alpha$ -shape. Parameter  $\alpha$  determines the radius of the disc connecting two outer points (source: CGAL (2004))

on a Delauney triangulation. The parameter  $\alpha$  is calculated by finding the smallest value of  $\alpha$  so that all points in the cluster are contained in the  $\alpha$ -shape without forming holes. It is possible, however, to set a value of  $\alpha$  to obtain different realisations of an  $\alpha$ -shape. For every reference class, pixel values were extracted from the corresponding reference areas in the image scene. These reference pixels form a cluster for each class in 3D feature space. *Hull* computes the coordinates of the corresponding  $\alpha$ -shapes for every cluster.

Next, the  $\alpha$ -shapes were visualised (using Java3D) in the 3D feature space plot. Directional lighting and shading were added to the plot and a shiny material appearance was applied to the  $\alpha$ -shapes, to improve visibility of pockets and voids. Transparency of the shapes could be changed interactively so that pixels inside  $\alpha$ -shapes were still visible.  $\alpha$ -shapes could be selected and queried to obtain information about their class label, mean values and colour. Figure 3.3 shows four different visualisations of class urban and class agriculture to show the difference in class representation. The convex hull and  $\alpha$ -shape depict the class shape more accurately than a sphere and ellipsoid do. The shapes of these two classes are elongated, showing that variance is not equal in every direction. Figure 3.4 shows  $\alpha$ -shapes for all land cover classes. Classes maquis, garrigue, pine and water are more compact, but show nevertheless very irregular shapes.

### 3.4. $\alpha$ -shape implementation and visualisation

---

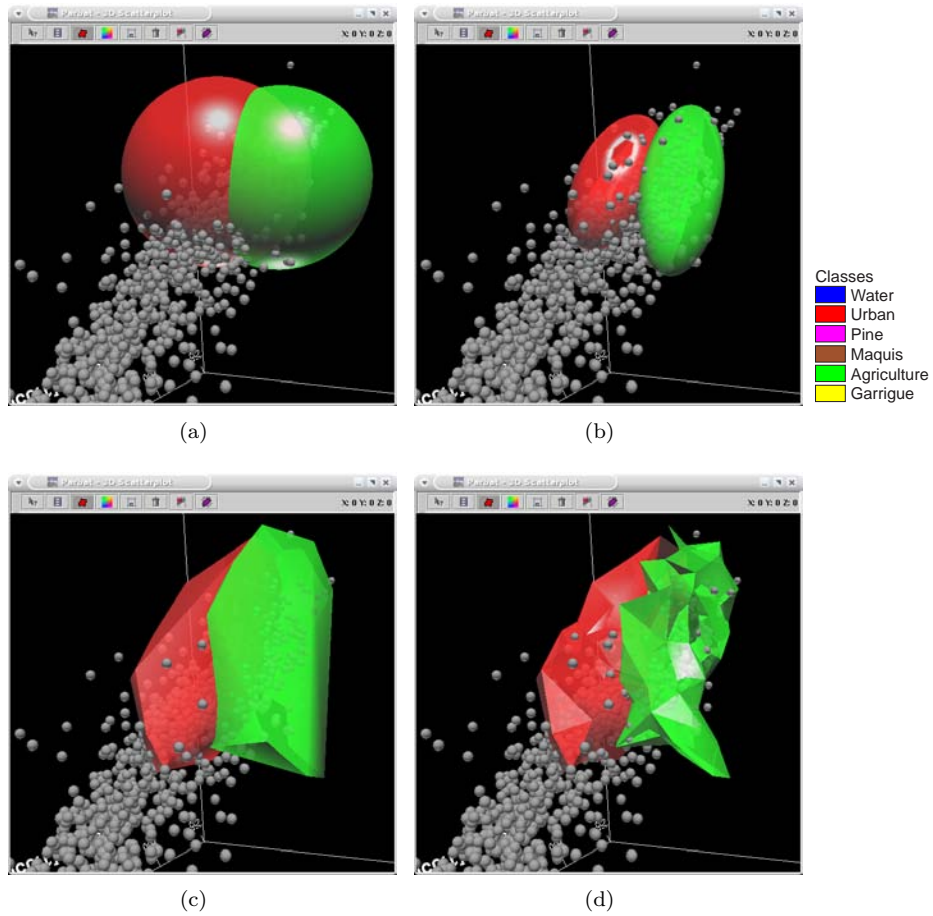


Figure 3.3: Comparison of class shape representation for class urban and class agriculture: (a) Classes visualised as spheres. Sphere radius is based on two times the maximum standard deviation; (b) Classes visualised as ellipsoids. Ellipsoid parameters are based on class covariance matrices; (c) Classes visualised as convex hulls; (d) Classes visualised as  $\alpha$ -shapes.

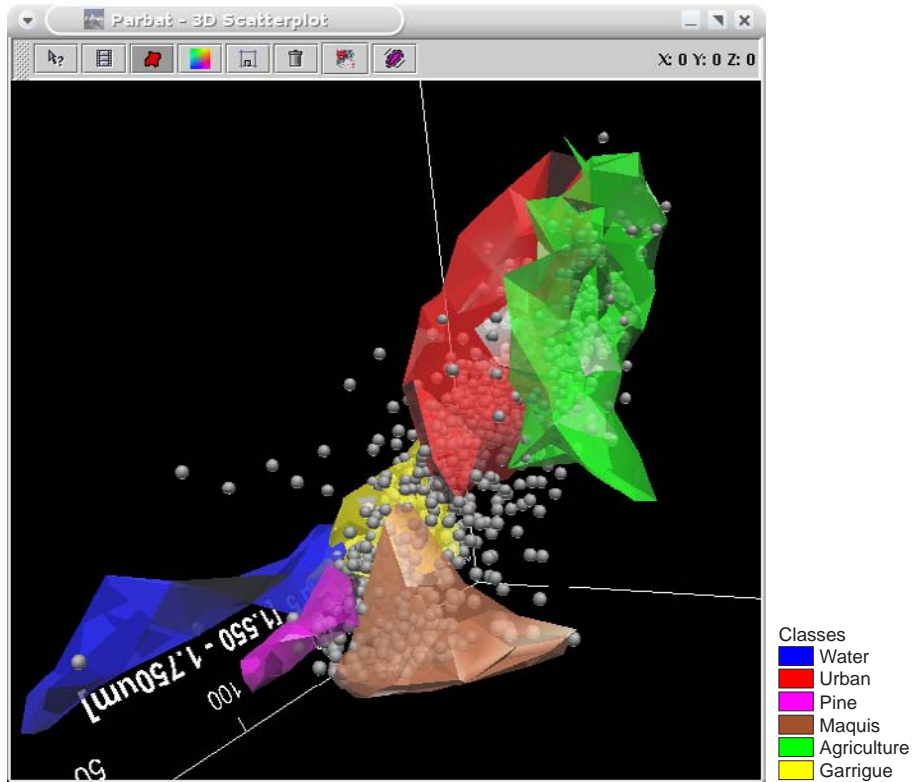


Figure 3.4:  $\alpha$ -shapes based on reference pixels for every land cover class.

### 3.5 $\alpha$ -shape based classification

Most classification algorithms make assumptions about class statistics. The most frequent used distance metrics are the Euclidean distance and the Mahalanobis distance, taking into account (co)variance of the reference clusters. A minimum distance to mean classifier applies the Euclidean distance and models a class cluster as a sphere around the mean vector in a 3D feature space. The Mahalanobis distances models a class cluster as an ellipsoid, assuming a normal distribution of cluster pixels. The frequently applied maximum likelihood classifier assumes that reference class clusters are characterised by a normal distribution, however, this is often not the case. Making invalid assumptions about class distributions

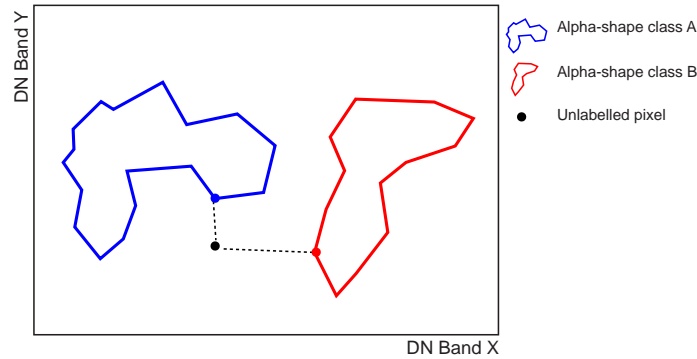


Figure 3.5: Euclidean distance from a pixel to the closest point on an  $\alpha$ -shape is used for fuzzy classification.

can lead to incorrect classification results, introducing errors and uncertainties. These conventional classifiers do not take into account concave or irregular cluster shapes, however, irregular clusters often occur in remotely sensed data. Figure 3.4 shows that most, if not all, class clusters are very irregular, not conforming to a normal distribution. A classifier that takes into account irregularities in class cluster shape might improve classification results and reduce uncertainties. In addition to visualisation of class clusters in 3D feature space,  $\alpha$ -shapes can be used to guide a fuzzy classification.

In this chapter, the fuzzy  $c$ -means classifier (equation 2.1) is adapted based on  $\alpha$ -shapes. For every (unclassified) pixel in the image the Euclidean distances from the pixel to the closest point on each of the  $\alpha$ -shapes are calculated (figure 3.5). Equation 2.1 is then used to compute membership values for every pixel to every land cover class. Fuzzy overlap  $q$  is set to 2.0. The classification result is ‘defuzzified’ based on the maximum membership and a crisp land cover map is obtained. The membership images for each class give valuable information about transition zones and uncertainty. To summarise thematic uncertainty of a pixel the confusion index is calculated (equation 2.2).

After classification, the results (hard classes, class memberships, maximum membership and confusion index) can be displayed as images. Dynamic links between the classification image displays and the 3D plot with the  $\alpha$ -shapes are valuable, as they give the user the possibility to explore and discover relations between the class of a pixel, its uncertainty, and its location in feature space. Based on the visual information a user can get a better impression of the spatial

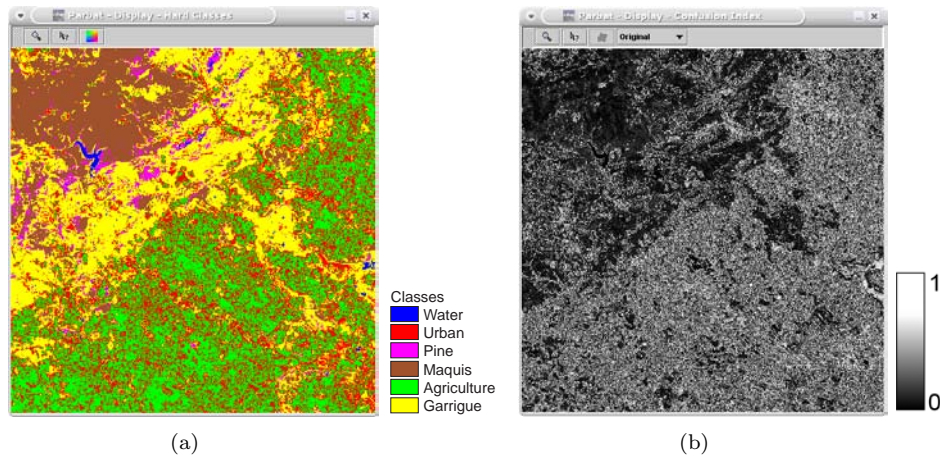


Figure 3.6:  $\alpha$ -shape based fuzzy classification result: (a) 'defuzzified' classification result; (b) image with the confusion index.

and thematic aspect of class uncertainty compared to traditional classification and visualisation techniques.

### 3.6 $\alpha$ -shape classification results

Similar to the classification in chapter 2, bands 4 (NIR), 5 (MIR) and 3 (RED) from the Landsat 7 image of the 'La Peyne' catchment are used to test the  $\alpha$ -shape based classifier. Figure 3.4 shows that classes agriculture and urban overlap considerably, but none of the other reference classes overlap.

Figure 3.6 and table 3.1 show that the urban class is over-classified and the agricultural class is under-classified, compared to what has been observed in the field. Furthermore, the image display with the confusion index visualises the spatial distribution of uncertainty. It shows that there is considerable confusion in agricultural and urban areas. This corresponds to the overlapping  $\alpha$ -shapes of these classes in the 3D feature space plot. In addition, in regions affected by shadow, confusion is high. Some shadow patches are classified as pine. This can be tested by selecting a pixel with high confusion in the confusion image display and by exploring its position in the feature space plot (it is highlighted, it flashes and the position of the viewer changes to the optimal location). Overall, the  $\alpha$ -shape

Table 3.1: Classification accuracy % for a classification based on  $\alpha$ -shapes

<i>Class</i>	<i>Reference</i>						
	Maquis	Garrigue	Urban	Agriculture	Water	Pine	Total
Maquis	100.00	0.00	0.00	0.00	0.00	0.00	39.16
Garrigue	0.00	99.46	0.96	4.59	0.00	0.00	21.18
Urban	0.00	0.00	72.49	25.25	0.00	0.00	13.23
Agriculture	0.00	0.00	26.56	70.16	0.00	0.00	20.94
Water	0.00	0.11	0.00	0.00	99.17	0.00	2.60
Pine	0.00	0.43	0.00	0.00	0.83	100.00	2.88
Total	100.00	100.00	100.00	100.00	100.00	100.00	100.00

Table 3.2: Classification accuracy for  $\alpha$ -shapes and convex hulls

Classifier	Bands	Distance	Accuracy %	Kappa
<i>Visual Classifier</i>	3, 4 and 5	$\alpha$ -shapes	69.92	0.63
<i>Visual Classifier</i>	3, 4 and 5	convex hull	68.40	0.61

classifier gives good results with an overall classification accuracy of 69.92%. Accuracy assessment results in table 3.2 show that the  $\alpha$ -shape based classifier performs slightly better than standard supervised fuzzy  $c$ -means classifiers. The confusion matrix shows that the overlapping classes Urban and Agriculture are difficult to separate. The visual classifier based on spheres, however, performs much better (see chapter 2 and table 2.4). The reason for this lower accuracy value might be due to the choice of the distance metric. In the next section, possible improvements are proposed.

### 3.7 Distance metrics for $\alpha$ -shape based classifier

The distance metric for the  $\alpha$ -shape based classification is taken as the Euclidean distance from a pixel to the nearest point on an  $\alpha$ -shape. In fact, this classification is similar to a nearest neighbour classifier, the main difference being that the representation of the reference class can be changed, by changing parameter  $\alpha$ . This is an important aspect, as these different class representations emphasise the fuzzy concept of classes.

A crucial aspect for the performance of a classifier is the choice of a distance metric. Ideally, the distance metric should account for the shape of the class clusters. The Euclidean distance to an  $\alpha$ -shape, as proposed in the previous section, is not an ideal distance metric for  $\alpha$ -shapes since it does not take into account the

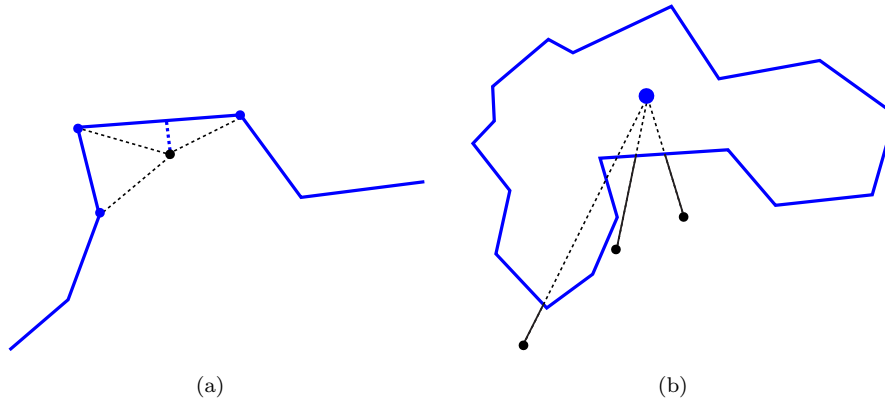


Figure 3.7: Problems with distance metric for  $\alpha$ -shape classifier: (a) The distance from a pixel to a pixel on the  $\alpha$ -shape might be incorrect, as the surface of an  $\alpha$ -shape might be closer; (b) The distance to an  $\alpha$ -shape centroid can give incorrect classification results. The 'real' distance might be much shorter or the projected line might intersect the shape at several positions.

central concept of the shape. Ideally, the distance metric should depict the shortest distance to the  $\alpha$ -shape. Since the distance from a pixel to the closest pixel on an  $\alpha$ -shape is used, the obtained distance does not always reflect the closest distance (figure 3.7(a)). In the case of  $\alpha$ -shapes, the distance metric could be calculated based on the  $\alpha$ -shape's centroid. A line could be projected from a pixel to the  $\alpha$ -shape's centroid. Then, the distance from to pixel to the line's intersection point with the shape could be used as a distance metric in classification (figure 3.7(b)). However, in some cases this technique might fail as the centroid might be located outside the shape (e.g. in case of a horseshoe shape) or the distance to the shape might be much closer than calculated. Additionally, the line might intersect the shape several times (figure 3.7(b)). Therefore, this distance metric might not reflect the actual situation and it might result in incorrect classification results.

Therefore, a distance measure based on the  $\alpha$ -shape as a representation of a membership function is proposed (figure 3.8). To use the  $\alpha$ -shape as a membership function the 'central concept' of the shape needs to be calculated. This central concept is defined as all locations in feature space where  $\mu = 1.0$ . The central concept can be modelled with the medial axis. The medial axis of a surface in 3D is the closure of all points that have two or more closest points on the surface (Dey and Zhao, 2002). A possible improvement of the  $\alpha$ -shape based classifier is a fuzzy

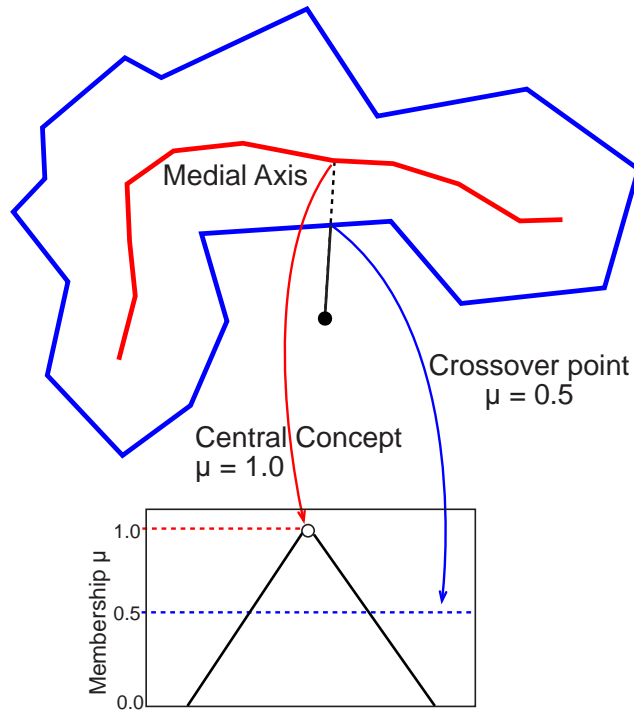


Figure 3.8:  $\alpha$ -shape used as representation for a membership function. The medial axis represents values with  $\mu = 1.0$ . The  $\alpha$ -shape itself is the cross-over point ( $\mu = 0.5$ ) of the membership function

classification algorithm, based on an  $\alpha$ -shape and its medial axis, representing a membership value of 1.0. The surface of the  $\alpha$ -shape represents the crossover point with a membership value of 0.5. Basically, every  $\alpha$ -shape represents an irregular membership function. For every unclassified pixel, a membership value can be calculated based on these membership functions, accounting for irregular class shapes. Figure 3.9 shows an example of a 3D medial axis of an  $\alpha$ -shape of the urban class.

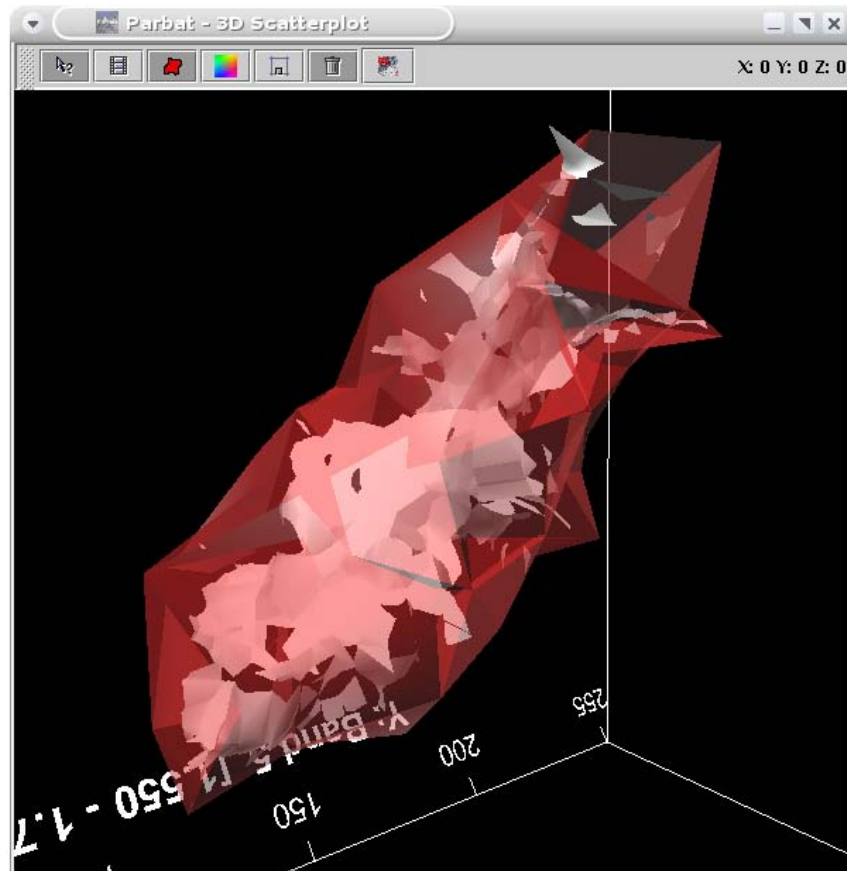


Figure 3.9: A 3D medial axis (shown in white) of an  $\alpha$ -shape (shown in semi-transparent red) for class urban

### 3.8 Discussion

For calculation of  $\alpha$ -shapes a parameter  $\alpha$  is required. It determines the resolution of the shape. Currently, the value for  $\alpha$  is chosen such that  $\alpha$  is as small as possible (i.e. shape described with highest accuracy), but all points in the reference pixel cluster are included in the shape. Thus, areas with a low density of reference pixels are still included in the  $\alpha$ -shape. A valuable addition would be an option to interactively change the value of parameter  $\alpha$  for each shape individually. This

function would provide much information on the density of points in class clusters.

The effectiveness of  $\alpha$ -shapes for remote sensing classification is not assessed in this study. However, a previous focus group user test showed that users are interested in visual class representations. All users made a comment about class shapes, saying that they would have liked to see the ‘real’ shape of a class cluster, because it would give more (accurate) information about the shape, position and overlap of classes. In this study, classes are represented by  $\alpha$ -shapes to show their irregularity in feature space. A visual classifier based on these shapes is a valuable addition to *Parbat* and traditional classifiers. Different users, however, might prefer different visualisations. For some users it might be more convenient to use spheres or ellipsoids for class interpretation, as  $\alpha$ -shapes might be too complex.

## 3.9 Conclusions

This chapter shows that  $\alpha$ -shapes provide a good technique for visualising class clusters in 3D feature space.  $\alpha$ -shapes show that class clusters are often irregularly shaped in a 3D feature space.  $\alpha$ -shapes are expected to be helpful in the interpretation and exploration of a remote sensing image classification and in assessing classification uncertainty. In addition to visualisation,  $\alpha$ -shapes were used to adapt the distance metric in a supervised fuzzy classification algorithm. Irregular or even concave shapes of class clusters were taken into account. A classification based on  $\alpha$ -shapes was implemented in *Parbat*. Classification results showed that a fuzzy classifier based on  $\alpha$ -shapes performs well with an overall accuracy of 70%, which was slightly higher than standard FCM classifiers but lower than the visual classifier discussed in chapter 2. However, several suggestions were given to improve the visual classifier based on  $\alpha$ -shapes. A possible improvement might include the use of a medial axis and an  $\alpha$ -shape for representation of a membership function. Future research should focus on usability and effectiveness issues for  $\alpha$ -shape visualisation.

**Part II**

**Segmentation**





## Chapter 4

# Segmentation of Spatial Objects and their Uncertainty\*

*Uncertainty and mystery are energies of life.  
Don't let them scare you unduly, for they keep boredom at bay and spark creativity.*

R. I. Fitzhenry

### 4.1 Introduction

In chapters 2 and 3, the focus was on visualisation of pixel-based classification techniques and thematic uncertainty. Object-oriented approaches to satellite sensor image processing have become increasingly popular with the growing amount of high-resolution satellite imagery and the increase in computing power (Sande et al., 2003; Zhan, 2003; Walter, 2004). The basic processing units of object-oriented image analysis are segments (image objects), as opposed to single pix-

---

\*This chapter is based on the following paper:

Lucieer, A. and Stein, A. (2002). Existential uncertainty of spatial objects segmented from satellite sensor imagery, *IEEE Transactions on Geoscience and Remote Sensing* **40**(11): 2518–2521.

---

els. Object-oriented analysis can provide useful information on object statistics, texture, shape (e.g. length, area, convexity, roundness, compactness), and topological features (e.g. neighbouring objects, super-object). Additionally, a close relation between real-world objects and image objects might exist. This relation can improve the value of the final classification and cannot be fulfilled by common, pixel-based approaches (Sande et al., 2003).

Segmentation techniques can help to extract spatial objects from an image scene. Image segmentation is primarily used to subdivide an image into meaningful segments. These segments may or may not correspond to objects as observed in the terrain. Image segmentation is in a sense related to spectral classification, which puts pixels into classes defined either *a priori* or during classification. Segmentation differs from classification, however, as spatial contiguity is an explicit goal of segmentation whereas it is only implicit in classification. Spectral classification of satellite sensor images applied on a pixel basis ignores potentially useful spatial information between pixels. Several studies have shown that segmentation techniques can help to extract spatial objects from an image (Gorte and Stein, 1998; Gorte, 1998; Sande et al., 2003; Benz et al., 2004; Li and Peng, 2004). A novel region growing segmentation algorithm was applied to identify land cover objects, forming the basis for classification for the land cover map 2000 (LCM2000) of Great-Britain. eCognition (eCognition, 2004) was the first commercial tool for segmentation and object-oriented classification for remote sensing and aerial imagery. It is a powerful tool for using image semantics in a classification procedure and it has been shown to give good classification results (Benz et al., 2004). However, an analysis of object uncertainty is lacking and no tools for quantification of object uncertainty are readily available.

Uncertainty will be present in any segmented image and can have a significant effect on further image processing. Therefore, existential uncertainty is of a major importance for spatial objects, expressing the uncertainty that an object, as identified by a segmentation procedure, exists (Molenaar, 1998). Quantification of existential uncertainty is essential to evaluate segmentation quality. Recently, probabilistic and fuzzy techniques have been used to quantify and model uncertainty in classification procedures (Wel et al., 1997; Zhang and Foody, 2001; Foody and Atkinson, 2002). This has mainly been applied on a pixel basis and no attention has been given to uncertainty related to image objects.

The objective of this study is to quantify existential uncertainty of spatial objects derived from high-resolution satellite sensor imagery with a split-and-merge image segmentation algorithm. The study is applied on an IKONOS image of an agricultural area near Enschede, the Netherlands. An essential step of image

segmentation is its validation. The existence of objects, however, depends upon the context of a study: for example, topographical objects may differ from geological objects or land cover objects. In this study the approach is taken that an object with a high existential certainty corresponds to an object as represented on a topographic map.

## 4.2 Image segmentation with a split-and-merge algorithm

Commonly, three approaches are distinguished towards segmentation (Haralick and Shapiro, 1985): edge-based segmentation, region-based segmentation and split-and-merge segmentation. Split-and-merge segmentation, as applied in this study, consists of a region splitting phase and an agglomerative clustering phase. In the splitting phase the image  $B$  is initially considered as a square block of pixel values with mean vector  $M_B$  and covariance matrix  $S_B$ . The dimension is determined by the number of bands in the image; in case of IKONOS this equals 4. This block is split into four square sub-blocks ( $B_1, B_2, B_3$  and  $B_4$ ), characterised by vectors of mean pixel values  $M_{B_1}, M_{B_2}, M_{B_3}$  and  $M_{B_4}$  and covariance matrices  $S_{B_1}, S_{B_2}, S_{B_3}$  and  $S_{B_4}$  in the sub-blocks.

To define homogeneity, a threshold  $\epsilon_{ms}$  for the mean and thresholds  $\epsilon_{ss}$  for the covariance matrix are considered. These values are chosen in advance and kept constant during segmentation. An image block  $B$  is homogeneous if

$$|M_{B_i} - M_B| < \epsilon_{ms} \quad \text{for } i = 1, 2, 3, 4 \quad (4.1)$$

and

$$|S_{B_i} - S_B| < \epsilon_{ss} \quad \text{for } i = 1, 2, 3, 4 \quad (4.2)$$

and heterogeneous if one of these equations does not apply. Heterogeneous sub-blocks are split recursively until homogeneity occurs or a minimum block size of one pixel is reached. The resulting data structure is a regular quadtree. In the clustering phase adjacent block segments are merged if the combined segment is homogeneous. The homogeneity rules 4.1 and 4.2 are applied in a similar way. Thresholds for mean and covariance matrix are denoted by  $\epsilon_{mm}$  and  $\epsilon_{sm}$ , respectively (Panjwani and Healey, 1995).

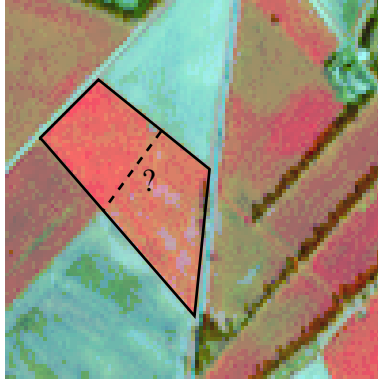


Figure 4.1: Existential uncertainty of the dotted object boundary is high, whereas the solid line represents an object with a low degree of existential uncertainty.

### 4.3 Quantifying existential object uncertainty

The final result of a segmentation procedure depends upon the thresholds  $\epsilon_{ms}$ ,  $\epsilon_{ss}$ ,  $\epsilon_{mm}$  and  $\epsilon_{sm}$ . For various thresholds, objects of different sizes emerge. Small  $\epsilon$  values lead to small objects, whereas large values result in large objects. Some objects are insensitive to threshold values, whereas some objects disappear beyond a particular threshold and others expand in size. It is hypothesised that objects emerging in a uniform shape irrespective of threshold values correspond to real world objects as represented on a topographic map. Objects disappearing at a specific threshold have a high degree of existential uncertainty and are called ‘unstable objects’. Objects which remain the same at different segmentation levels are ‘stable’ objects and have a low degree of existential uncertainty. Object uncertainty can be represented by their boundaries (figure 4.1).

To quantify existential uncertainty in a segmentation procedure, ranges for the splitting thresholds  $\epsilon_{ms}$  and  $\epsilon_{ss}$  and merging thresholds  $\epsilon_{mm}$  and  $\epsilon_{sm}$  are chosen. These ranges are divided into  $n$  steps. At each step, object boundaries, in the form of segment edge pixels, are determined. At step  $k$  these boundary pixels are assigned the value 1 and non-boundary pixels the value 0 and are represented on a segment-boundary image  $I_k$ . This results in an image with boundary stability index ( $BSI$ ) values, defined as

$$BSI = \frac{\sum_{k=0}^n I_k}{n} \quad (4.3)$$

*BSI* contains values between 0.0 and 1.0, the value 0.0 emerging in the absence of a boundary at each step, the value 1.0 in the presence of a boundary at each step, and intermediate values in between. Segment boundaries with large *BSI*-values are boundaries with a high existential certainty, small *BSI*-values represent boundaries with high existential uncertainty.

## 4.4 Segmentation validation measures

Segmentation validation is necessary to assess segmentation accuracy. To quantitatively assess a segmentation result,  $m$  objects from a reference data set are identified and the percentage of overlap of the largest segments inside these objects is calculated. The image is over-segmented if overlap is less than one hundred percent and under-segmented if overlap is more than one hundred percent. To quantify the fit of each of the reference objects with the largest segments overlapping these objects, the area fit index (*AFI*) is used,

$$AFI = \frac{A_{\text{reference object}} - A_{\text{largest segment}}}{A_{\text{reference object}}} \quad (4.4)$$

where  $A$  is the area in pixels. For a perfect fit overlap is 100% and *AFI* equals 0.0. A reference object is over-segmented if overlap is less than 100% and *AFI* is greater than 0.0. A reference object is under-segmented if overlap is 100% and *AFI* less than 0.0. In some situations overlap can be less than 100% and *AFI* is less than 0.0, then the object is over-segmented but the largest segment is larger than the reference object.

Another technique for segmentation validation is to quantitatively compare segment boundaries with boundaries on a reference map. Following Delves et al. (1992), let  $p$  be a boundary pixel of a region in the reference map and  $D(p)$  be the shortest (Euclidean) distance, measured in pixels, between  $p$  and any boundary pixel in the segmented image. Then,

$$D(b) = \frac{\sum_{\text{boundary pixels}} D(p)}{N} \quad (4.5)$$

where the sum is taken over all boundary pixels in region  $b$ , and  $N$  is the number of boundary pixels in the reference data set. As such,  $D(b)$  measures the average distance between a segment boundary pixel and the reference boundary. For a perfect fit,  $D(b)$  equals 0.0. If the region  $b$  equals the whole image, the image segmentation accuracy measure is obtained, denoted by  $D(B)$ . The number of

boundary pixels in the segmented image  $M$ , however, is not taken into account. For high values of  $M$  many boundary pixels in the neighbourhood of  $p$  occur and therefore, low  $D(B)$  values are obtained. A boundary image with a high  $M$  value may be extremely over-segmented. To correct for  $M$  in the calculation of  $D(B)$  the following correction factor is proposed

$$D(B)_{corr} = \frac{|N - M|}{N} + D(B) \quad (4.6)$$

Recently, Prieto and Allen (2003) introduced the closest distance metric (CDM) for evaluation of similarity between boundary images. For each boundary pixel in the segmented boundary image, the reference image is inspected for a possible matching boundary pixel within a certain radius. The closest distance is then used to define a cost function

$$CDM = 100 \left( 1 - \frac{D(M, N)}{|M \cup N|} \right) \quad (4.7)$$

$D(M, N)$  is the cost of matching boundary pixels based on the closest distance metric, and  $|M \cup N|$  is the union of boundary pixels in the two images. The advantage of  $CDM$  is that it provides a normalised value in percentage accuracy. In addition, it takes into account the difference between the number of boundary pixels in the segmented image and the reference map.

## 4.5 Study area

The study area, characterised by agriculture, is located south-west of Enschede, the Netherlands. Six land cover types occur in the area: water, grassland, woodland, bare soil, crops and build up area. Both homogeneous and heterogeneous parcels occur, with crisp objects dominating the region. A subset of 512 by 512 pixels of an IKONOS image, covering all major land cover types, acquired on April the 3<sup>rd</sup> of 2000 is used for this study (figure 4.2).

A vector-based topographic map on scale 1:10 000 is used as a reference data set for segmentation validation. The vector map is converted to raster format with a spatial resolution equal to the IKONOS image. The image is geometrically corrected with ground control points derived from the topographic map. The root mean squared error (RMSE) of geometric correction was 0.349 pixel. A first

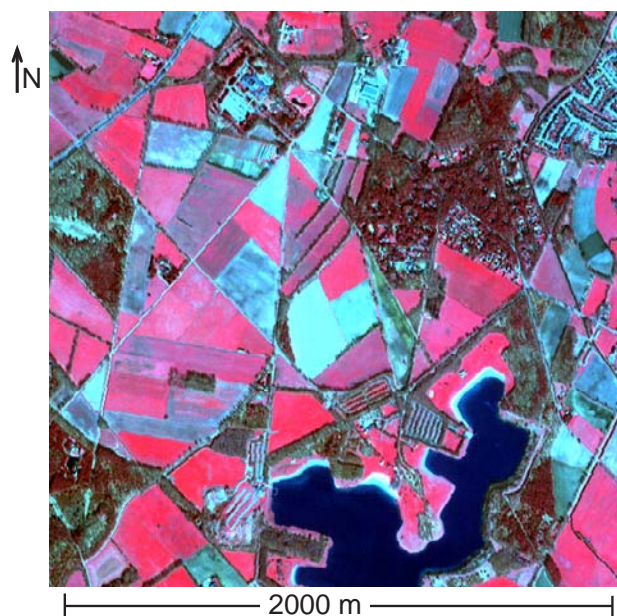


Figure 4.2: False colour composite of a subset of an IKONOS image of an area southwest of Enschede, the Netherlands (acquired 3<sup>rd</sup> of April, 2000).

degree polynomial function was used to register the image to the topographic map coordinate system.

## 4.6 Segmentation results

Figure 4.3 presents a single segmentation of the image. For this segmentation the following values were used:  $\epsilon_{ms} = 10.0$ ,  $\epsilon_{ss} = 300.0$ ,  $\epsilon_{mm} = 20.0$  and  $\epsilon_{sm} = 100.0$ . In the splitting phase 60355 homogeneous blocks were formed. After merging 18387 objects remained. An initial visual assessment showed that forested areas and urban regions contained a large number of very small segments, caused by the large variance in reflectance in these areas. Homogeneous parcels and the water body were correctly segmented, whereas heterogeneous parcels were over-segmented.

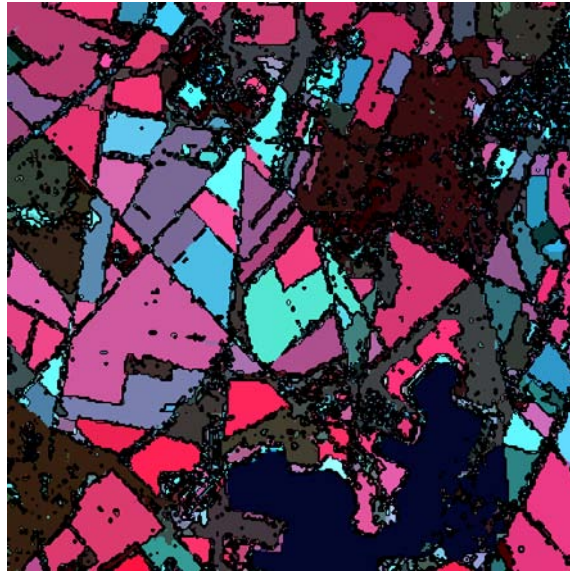


Figure 4.3: Segmented IKONOS image after splitting and merging phase. Object colours are determined by their mean DN-value. Object boundaries are shown in black.

As crisp objects dominate the image scene it is assumed that objects can be represented by their boundaries. An image with *BSI*-values was calculated to depict object stability. The number of segmentation steps  $n$  was 100. Thresholds for splitting were kept small  $\epsilon_{ms} = 10.0$  and  $\epsilon_{ss} = 300.0$ , and constant for all steps to avoid blocky artifacts in the segmentation result. Thresholds for merging ranged from  $\epsilon_{mm} = 12.0$  to 42.0 and  $\epsilon_{sm} = 25.0$  to 275.0. Figure 4.4 shows the resulting *BSI*-values in grey-scale. Bright values depict high boundary stability, while low stability is represented by darker values, non-boundary pixels are black. Boundaries of heterogeneous parcels and boundaries of small objects in urban and forested areas are characterised by low stability, and therefore, high uncertainty values. Boundaries of the water body, homogeneous parcels and roads can be clearly identified in the image and are depicted by high *BSI*-values.



Figure 4.4: BSI in grey-scale; high stability boundaries are bright, while low stability boundaries are dark, non-boundary pixels are black.

## 4.7 Segmentation validation

The first step in segmentation validation was a visual comparison of object boundaries from a segmentation result with object boundaries from the topographic reference map. Figure 4.5 shows the boundaries of a segmentation result (thresholds:  $\epsilon_{ms} = 10.0$ ,  $\epsilon_{ss} = 300.0$ ,  $\epsilon_{mm} = 20.0$  and  $\epsilon_{sm} = 100.0$ ). The boundaries of the topographic map are given in figure 4.6. It shows that the main object boundaries match with the topographic map, the forested and urban areas are over-segmented as a lot of small segments occur.

To quantitatively assess segmentation results seven reference objects were selected from the topographic raster map (figure 4.6). These objects represented the land use in the study area. Seven objects that are easy to segment (e.g. water body) and difficult to segment (e.g. forest and a heterogeneous parcel) were chosen. These seven reference objects are described in table 4.1.

For each segmentation step, three object properties provided an indication of segmentation accuracy. A first indication was the number of segments inside each



Figure 4.5: Object boundaries from segmentation result.

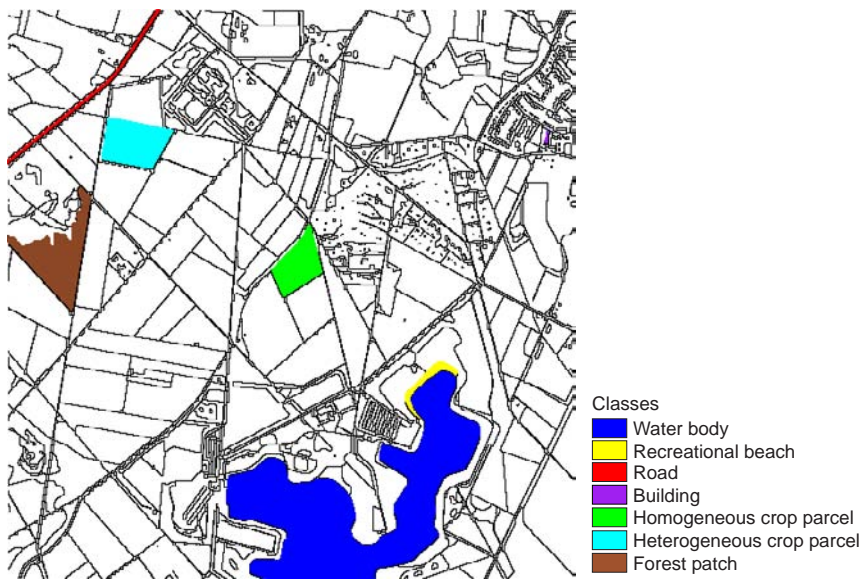


Figure 4.6: Boundaries from topographic map and seven reference objects.

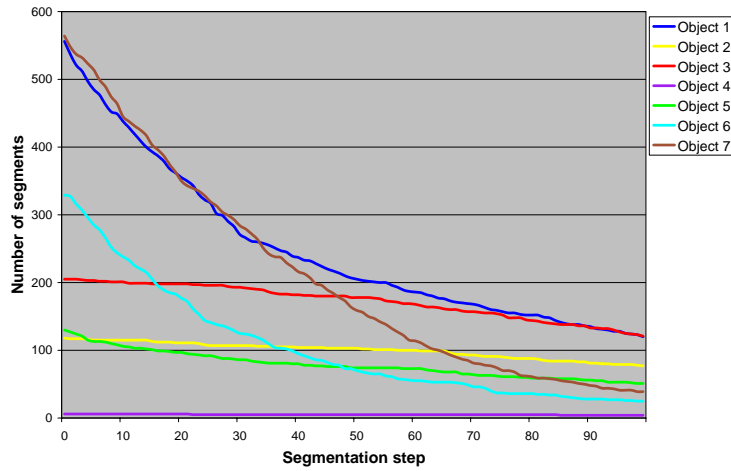


Figure 4.7: The number of segments within each reference object.

of the reference objects for each segmentation step (figure 4.7). The largest segment best approximates the reference object, but segments can be very small. A second accuracy indication was the area of the largest segment inside a reference object. With this property the overlap percentage was calculated. For a perfect fit overlap should be a 100% (figure 4.8). The largest overlap occurred at segmentation steps with the highest thresholds. To quantify segmentation accuracy using area information the Area Fit Index  $AFI$  was used (equation 4.4).  $AFI$ -values for the 7 reference objects are given in figure 4.9.

The number of segments inside a reference objects decreased for each object

Table 4.1: Description of seven reference objects used for validation

Object	Area [pixels]	Description
object 1	16453	Water body (lake)
object 2	421	Recreational beach
object 3	560	Road
object 4	33	Building
object 5	1540	Homogeneous crop parcel
object 6	2101	Heterogeneous crop parcel
object 7	2823	Forest patch

#### 4.7. Segmentation validation

---

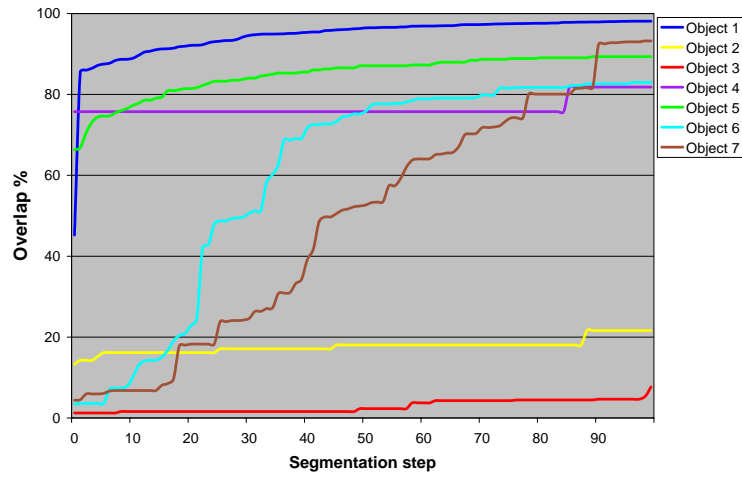


Figure 4.8: Overlap percentages of the largest segment inside each reference object.

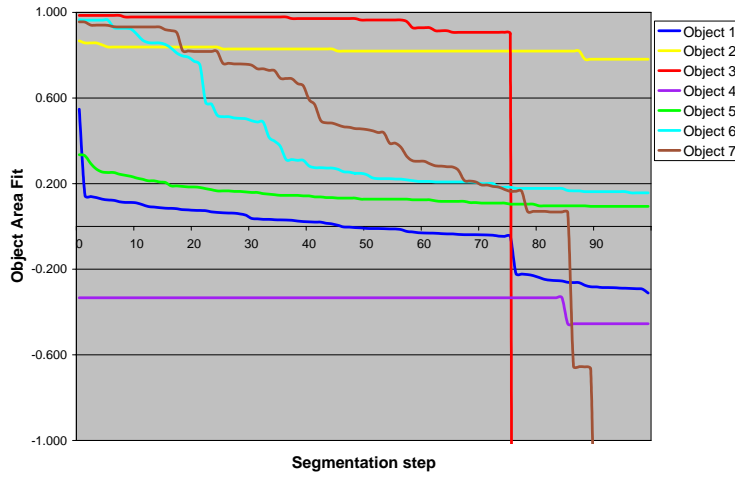


Figure 4.9: *AFI* values for the largest segment inside each reference object.

(figure 4.7). Generally, these segments were very small and for calculation of overlap percentage the largest segments were used. For each reference object the overlap percentage increased with higher threshold values (figure 4.8). For objects 1 (lake) and 7 (forest) overlap percentages were higher than 93% at segmentation steps with the highest thresholds. Objects 4 (building), 5 (homogeneous parcel) and 6 (heterogeneous parcel) contained overlap values between 80% and 90%. Object 2 (recreational beach) and object 3 (road) contained overlap values less than 22%. To determine the fit of segments  $AFI$ -values were calculated (figure 4.9). For an ideal fit  $AFI$  equals 0.0 and overlap equals 100%. For none of the 7 objects this situation occurred. If  $AFI$  is greater than 1.0 and overlap is less than 100% a reference object is over-segmented. Object 1 (lake) reached an  $AFI$ -value of 0.0 at segmentation step 50, its overlap was 96% at this step. Objects 2 and 3 did not reach an  $AFI$ -value of 0.0. Object 2 was over-segmented for all steps. At segmentation step 76 the largest segment of object 3 was merged with an agricultural parcel resulting in a large negative  $AFI$ -value. The bad fit for object 2 and 3 can be explained by the fact that neighbour adjacency was calculated based on 4 directions (north, east, south, west), also known as a 4-adjacency model. The 8-adjacency model also takes into account the diagonal neighbours. This adjacency model might be useful in segmenting long shaped objects with a diagonal orientation, like object 2 and 3. Object 4 (building) showed negative  $AFI$ -values between -0.36 and -0.44. Thus, the largest segment was larger than the reference object (under-segmented), but did not entirely overlap (maximum overlap was 82%). The resolution of the multi-spectral IKONOS bands was too coarse for detection of individual buildings, therefore, the accuracy for the building object was poor. Segmentation of object 5 (homogeneous crop) was best for the final segmentation step (overlap was 90% and  $AFI$  was 0.10). This also occurred for object 6 (heterogeneous crop), but overlap was 83% and  $AFI$  was 0.17. At segmentation step 85, object 7 (forest) was segmented best, with an  $AFI$ -value of 0.08 and an overlap of 82%. After segmentation step 86, object 7, was under-segmented.

Segmentation validation for the whole image was carried out using a boundary matching procedure. The  $D(B)$  measure (equation 4.5) was used to describe a segment's fit to a reference object by means of its boundaries. Thus, all boundaries from each segmentation step were compared to the boundaries of objects in the topographic reference map.  $D(B)$  values in figure 4.10 show that the best fit of segment boundaries was obtained at the first segmentation step. Most objects, however, were severely over-segmented in the first step. Therefore, a corrected value  $D(B)_{corr}$  (equation 4.6) was applied to correct for the number of boundary pixels in the segmented image. Where  $D(B)_{corr}$  was equal to  $D(B)$ , the number of boundary pixels was equal in both the segmented image and topographic map

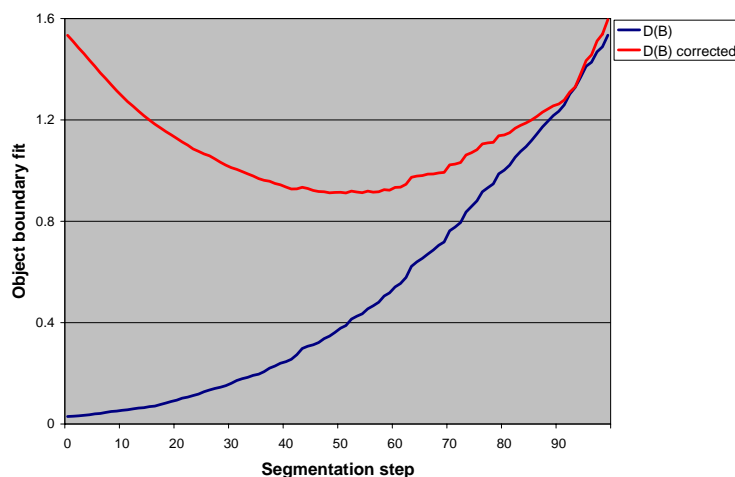


Figure 4.10: Boundary fit  $D(B)$  and  $D(B)_{corr}$  values for the whole image for each segmentation step.

and the correction factor was 1.0. At this step  $D(B)$  was equal to 1.33.  $D(B)_{corr}$  values showed that an optimal segmentation result, for a best boundary fit and an optimal number of boundary pixels, was obtained at segmentation step 55 for  $D(B)_{corr} = 0.91$ .

Additionally,  $CDM$  provided an accuracy percentage for boundary matching for the whole image. Figure 4.11 shows a  $CDM$  value for every segmentation step. The best match with the topographic map was obtained at segmentation step 64, with a  $CDM$  value of 53.38%.

## 4.8 Discussion

The split-and-merge algorithm used in this study generally produced good segmentation results. Glasbey (Glasbey and Horgan, 1995) found that boundaries derived with split-and-merge segmentation are rough and retain some of the artifacts of blocks from the splitting phase. If the thresholds for splitting are kept small, however, these blocky artifacts are no longer present in the final segmentation result. Texture measures could be used to improve segmentation in texture rich areas such as forested and urban regions in the IKONOS image. The use of texture will be

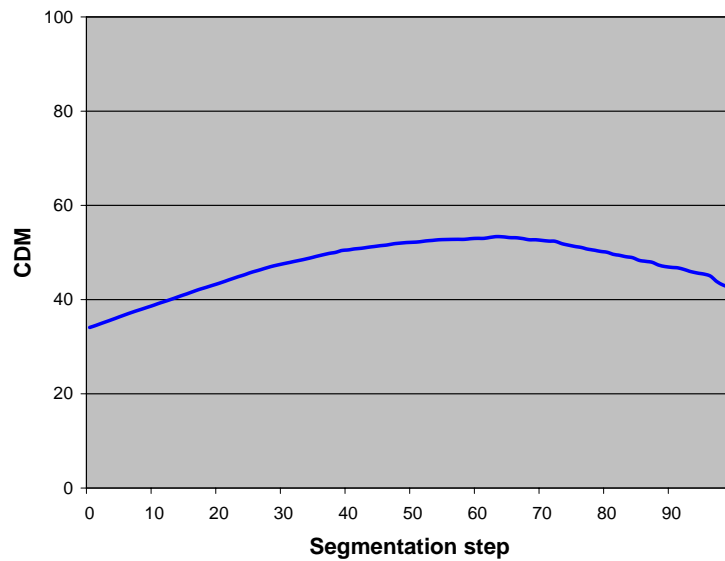


Figure 4.11: Boundary fit *CDM* values for the whole image for each segmentation step.

discussed in the following chapters. Additionally, elongated objects (e.g. object 2 and 3) give difficulties in segmentation. An 8-adjacency neighbourhood model as opposed to a 4-adjacency model might be useful in segmenting elongated objects with a diagonal orientation, like object 2 and 3. Under-segmentation of small objects, like object 4, can be explained by the fact that the spatial resolution of the multi-spectral IKONOS bands (4m) is too coarse for detection of small buildings. Incorporation of information from the panchromatic band could be helpful in this case.

In this study existential uncertainty of image objects was discussed. Other types of uncertainty, like extensional uncertainty (Molenaar, 1998; Cheng and Molenaar, 2001), can be distinguished as well. This type of uncertainty refers to the uncertainty in spatial extent of an object. Extensional uncertainty is important for the spatial representation of fuzzy objects. For crisp objects existential uncertainty, as described here, plays the most important role.

In this chapter, different accuracy assessment techniques were applied. Consequently, different accuracy values for the same segmentation result were generated. Hence, even the validation procedure is subjected to uncertainty. The context of

the validation map is an important issue, as topographic objects used as reference are likely to provide other segmentation accuracy values as objects derived from a soil map or geological map. This factor should be taken into account for interpretation of validation results.

## 4.9 Conclusions

In this chapter, a method to quantify existential uncertainty of spatial objects derived from satellite sensor imagery with a split-and-merge image segmentation algorithm is proposed. Objects disappearing at a specific segmentation threshold have a high degree of existential uncertainty and are called ‘unstable objects’. Objects which remain the same at different segmentation levels are ‘stable’ objects. These objects have a low degree of existential uncertainty, characterised by a boundary stability index  $BSI$  derived from a range of segmentations generated with different threshold values.

Seven reference objects were selected from a topographic map for segmentation validation. The percentage of overlap and the area fit index  $AFI$  are measures for quantification of segmentation accuracy. To determine segmentation accuracy for the whole image, segment boundaries were used to calculate the fit  $D(B)$  with the topographic boundaries. A correction factor  $D(B)_{corr}$  was proposed to correct for the number of boundary pixels in the segmented image. Additionally, the  $CDM$  metric was used to calculate a normalised accuracy percentage, taking into account the number of boundary pixels. The boundary stability index ( $BSI$ ) allows for a quantification of existential uncertainty and is suitable for its visualisation. The area fit index ( $AFI$ ) and the closest distance metric ( $CDM$ ) are suitable measures for validation of segmentation results.

## Chapter 5

# Texture-based Segmentation to Identify Fuzzy Objects\*

*When the only tool you have is a hammer,  
everything begins to look like a nail.*

L. Zadeh

### 5.1 Introduction

The focus of the previous chapter, was on identification of image objects using segmentation. Existential uncertainty was quantified by the object boundary stability index. The study area was characterised by crisp objects, therefore, object uncertainty could be depicted by object boundaries. Many geographical phenomena, however, are characterised by indeterminate boundaries (Burrough and

---

\*This chapter is based on the following papers:

Lucieer, A., Fisher, P. F. and Stein, A. (2004). *GeoDynamics*, CRC Press LLC, chapter Texture-based Segmentation of Remotely Sensed Imagery to Identify Fuzzy Coastal Objects.

Lucieer, A., Stein, A. and Fisher, P. F. (2003). Texture-based segmentation of high-resolution remotely sensed imagery for identification of fuzzy objects, *Proceedings of GeoComputation 2003*, Southampton, UK.

Lucieer, A., Fisher, P. F. and Stein, A. (2003). Fuzzy object identification using texture-based segmentation of high-resolution DEM and remote sensing imagery of a coastal area in England, *Proceedings of the Second International Symposium on Spatial Data Quality*, Hong Kong.

---

Frank, 1996; Fisher, 2000). Extensional uncertainty, depicting uncertainty in spatial extent of objects (Molenaar, 1998), is often very high for objects with indeterminate boundaries, also known as fuzzy objects (Cheng and Molenaar, 1999; Molenaar and Cheng, 2000; Molenaar, 2000; Cheng and Molenaar, 2001). In areas where fuzzy objects dominate, an indication of object uncertainty is important.

A straightforward approach to identify fuzzy objects is to apply a (supervised) fuzzy *c*-means classification (FCM), or similar soft classifier (Bezdek, 1981; Foody, 1996; Zhang and Foody, 2001). This classifier gives the class with the highest membership for each pixel, and membership values of belonging to any other class. However, pixel-based classifiers, like the FCM, do not take spatial relations between pixels into account, also known as pattern or texture.

Texture analysis has been addressed and successfully applied in remote sensing studies in the past. An interesting overview paper concerning texture measures is from Randen and Husøy (1999). Bouman and Liu (1991) studied multiple resolution segmentation of texture images. A Markov random field (MRF) model-based segmentation approach to classification for multi-spectral images was carried out by Sarkar et al. (2002). For multi-spectral scene segmentation and anomaly detection, Hazel (2000) applied a multivariate Gaussian MRF. Recently, Ojala and his co-workers have further pursued an efficient implementation and application towards multi-scale texture-based segmentation (Ojala et al., 1996; Ojala and Pietikäinen, 1999; Pietikäinen et al., 2000; Ojala, Pietikäinen and Mäenpää, 2002). Their Local Binary Pattern (LBP) measure outperforms most of the traditional texture measures in classification of texture images (Ojala et al., 1996). LBP is a rotation invariant grey scale texture measure.

In identifying spatial objects from remotely sensed imagery, the use of texture is important. Texture reflects the spatial structure of pixels in an image, and it is therefore indispensable in segmenting an area into sensible geographical units. The aim of this study is to present a supervised texture-based image segmentation technique that identifies objects from fine spatial resolution Light Detection And Ranging (LiDAR) imagery and from multi-spectral Compact Airborne Spectral Imager (CASI) imagery. It is applied to a coastal area in northwest England. Information on coastal land cover and land form units is required for management of this conservation area. Since this environment is highly dynamic, (semi-) automatic and objective techniques are required to update information and maps. This chapter further explores the use of texture in segmentation. Additionally, a focal point is quantification of object uncertainty to identify transition zones.

## 5.2 Study area

The study area is on the coast of Northwest England, known as the Ainsdale Sands. The Ainsdale Sand Dunes National Nature Reserve (NNR) totals 508 ha and forms part of the Sefton Coast. The NNR is within the coastal Special Protection Area. It is also within the Sefton Coast candidate Special Area of Conservation. The NNR contains a range of habitats, including intertidal sand flats, embryo dunes, high mobile yellow dunes, fixed vegetated dunes, wet dune slacks, areas of deciduous scrub and a predominantly pine woodland. Management of this area consists of extending the area of open dune habitat through the removal of pine plantation from the seaward edge of the NNR, maintaining and extending the area of fixed open dune by grazing and progressively creating a more diverse structure within the remaining pine plantation with associated benefits for wildlife (Sefton Coast Partnership, 2004). Therefore, mapping of this coastal area can be useful for protection and management of the environment as a major and threatened habitat type and as a defence against coastal flooding.

In 1999, 2000 and 2001 the Environment Agency, UK, collected fine spatial resolution digital surface models (DSM) by LiDAR, and simultaneously, acquired multi-spectral Compact Airborne Spectral Imager (CASI) imagery (one flight each year). The aircraft was positioned and navigated using Global Positioning System (GPS) corrected to known ground reference points. The aircraft flew at approximately 800 m above ground level, acquiring 2 m spatial resolution LiDAR scenes and 1 m spatial resolution CASI imagery. In this study, the imagery of 2001 was used. These images, geometrically corrected by the Environment Agency, were spatial composites of multiple flight strips. The area covered by these images was approximately 6km<sup>2</sup>. Figure 5.1(a) displays a subset of 512 by 512 pixels of band 12 (Near Infrared) of the CASI image. Figure 5.1(b) shows the LiDAR DSM of the same area.

A relevant distinction exists between land cover and land form, both characterising coastal objects. Land form properties can be extracted from digital elevation, the LiDAR DSM of the area. Four land form classes can be distinguished: beach plain, dune, dune slack and woodland. Land cover is obtained from spectral information from the CASI imagery. Four land cover classes can be distinguished: sand, marram grass, willow shrub and woodland. Detailed mapping of these units is required, because knowledge about the location and dynamics of these object types is important for monitoring the rare habitats in this area, as well as, the coastal defence against flooding.

## 5.2. Study area

---

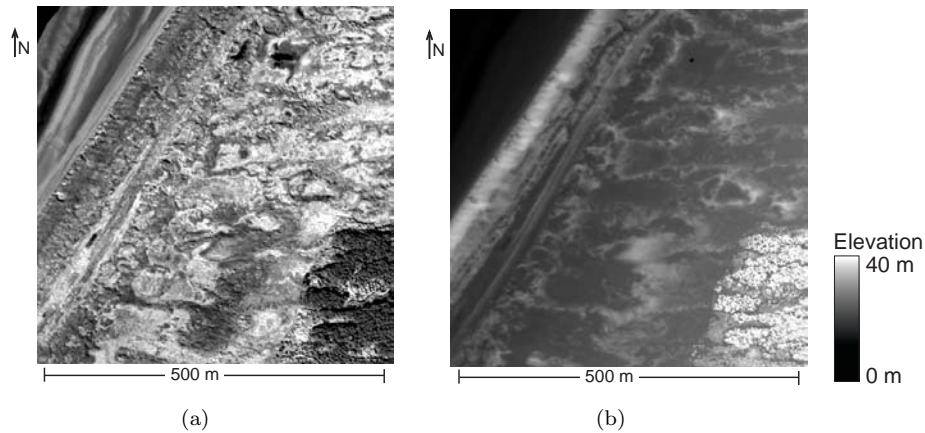


Figure 5.1: Overview of the study area: (a) Band 12 (NIR, 780 nm) of a CASI image of the Ainsdale Sands; (b) LiDAR DSM of the study area.

Coastal objects are characterised by fuzzy boundaries. Therefore, information on uncertainty is required to identify transition zones and to map these objects. Cheng and Molenaar (2001) proposed a fuzzy analysis of dynamic coastal land forms. They classified the beach, foreshore and dune area as fuzzy objects based on elevation data using a semantic import model. Some classification errors, however, are likely to occur when using elevation as diagnostic information alone. For example, an area of low elevation behind the fore dune was classified as beach, whereas it is almost certainly an area of sand removal by wind like a blowout or an inter dune area. These types of errors can be reduced by using spatial or contextual information (by looking at morphometry or land forms). Cheng et al. (2002), Fisher et al. (in press) and Fisher et al. (2004) proposed a multi-scale analysis for allocating fuzzy memberships to morphometric classes. This technique can be used to model objects, which are vague for scale reasons. The morphometry classes modelled at different scale levels were: channel, pass, peak, pit, plane, and ridge. Although this analysis fails to identify positions of dunes, it is possible to identify dune ridges and slacks and to monitor their changing positions. The use of textural information might improve identification of these coastal objects.

### 5.3 Texture

Regions with similar reflectance can be identified easily as objects on a remote sensing image. Additionally, texture is an important property of geospatial objects and should be taken into account in image analysis. In this study, texture is defined as a pattern or characteristic spatial variability of pixels over a region. The pattern may be repeated exactly, or as a set of small variations, possibly as a function of position. There is also a random aspect to texture, because size, shape, colour and orientation of pattern elements can vary over the region.

Measures to quantify texture can be split into structural (transform-based), statistical and combination approaches. Well-known structural approaches are the Fourier and wavelet transform. Several measures can be used to describe these transforms, including entropy, energy and inertia (Nixon and Aguado, 2002). A well known statistical approach is the grey level co-occurrence matrix (GLCM) (Haralick et al., 1973) containing elements that are counts of the number of pixel pairs for specific brightness levels. Other texture descriptors are Markov random fields (MRF), Gabor filter, fractals and wavelet models. A comparative study of texture classification is given in (Randen and Husøy, 1999). They concluded that a direction for future research is the development of powerful texture measures that can be extracted and classified with low computational complexity. A relatively new and simple texture measure is the local binary pattern operator (LBP) (Ojala et al., 1996; Pietikäinen et al., 2000; Ojala, Pietikäinen and Mäenpää, 2002). It is a theoretically simple yet efficient approach to grey scale and rotation invariant texture classification based on local binary patterns.

### 5.4 Texture measure - the Local Binary Pattern Operator (LBP)

Ojala, Pietikäinen and Mäenpää (2002) derived LBP by defining texture  $T$  in a local neighbourhood of a grey scale image as a function  $t$  on the grey levels of  $P$  ( $P > 1$ ) image pixels

$$T = t(g_c, g_0, \dots, g_{P-1}) = t(g_c, \vec{g}_P) \quad (5.1)$$

where  $g_c$  corresponds to the value of the centre pixel  $p_c$  and  $\vec{g}_P = (g_0, \dots, g_{P-1})$  represents the values of pixels in its neighbourhood. The neighbourhood is defined

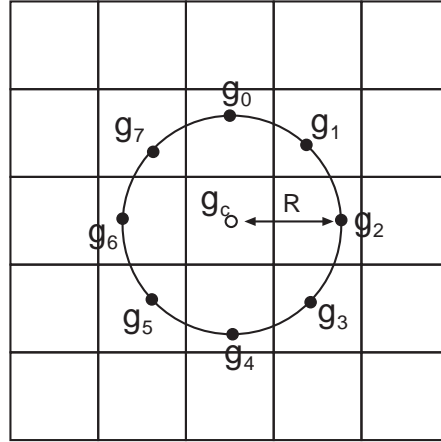


Figure 5.2: Circular pixel neighbourhood set for  $P = 8$  and  $R = 1$

by a circle of radius  $R$  with  $P$  equally spaced pixels that form a circularly symmetric neighbourhood set (figure 5.2). The coordinates of the neighbouring pixels in a circular neighbourhood are given by

$$\{x_{c,i}, y_{c,i}\} = \{x_c - R \sin \frac{2\pi}{P}, y_c + R \cos \frac{2\pi}{P}\} \quad (5.2)$$

Invariance with respect to the scaling of pixel values or illumination differences is achieved by considering the signs of the differences instead of their numerical values

$$T^* = t(\text{sign}(g_0 - g_c), \text{sign}(\vec{g}_P - g_c)) \quad (5.3)$$

This results in the following operator for grey scale and rotation invariant texture description

$$LBP_c = \sum_{i=0}^{P-1} \text{sign}(g_i - g_c) \quad (5.4)$$

Ojala, Pietikäinen and Mäenpää (2002) found that not all local binary patterns describe properties of texture well. LBP captures the uniformity of the central pixel towards its neighborhood, but it does not capture the uniformity of the neighborhood itself. Therefore, they introduced a uniformity measure  $U$  to define uniformity in patterns, corresponding to the number of spatial transitions or bitwise 0/1 changes in the pattern. With  $g_P = g_0$ ,  $U_c$  is defined as

$$U_c = \sum_{i=1}^P |\text{sign}(g_i - g_c) - \text{sign}(g_{i-1} - g_c)| \quad (5.5)$$

Patterns with  $U_c \leq j$  are designated as uniform. Ojala, Pietikäinen and Mäenpää (2002) found that for  $j = 2$  the best LBP measure is obtained for describing texture images. This results in the following operator for grey scale and rotation invariant texture description

$$LBP_{c,j} = \begin{cases} \sum_{i=0}^{P-1} \text{sign}(g_i - g_c), & \text{if } U_c \leq j \\ P + 1, & \text{otherwise} \end{cases} \quad (5.6)$$

The LBP operator thresholds the pixels in a circular neighbourhood of  $P$  equally spaced pixels on a circle of radius  $R$ , at the value of the centre pixel. It allows for detecting uniform patterns for any quantisation of the angular space and for any spatial resolution. Non-uniform patterns are grouped under one label,  $P + 1$ .

## 5.5 Texture-based image classification

Most approaches to supervised texture classification or segmentation assume that reference samples and unlabelled samples are identical with respect to texture scale, orientation, and grey scale properties. This is often not the case, however, as real world textures can occur at arbitrary spatial resolutions, rotations and illumination conditions. The LBP operator is very robust in terms of grey scale variations, since the operator is by definition invariant against any monotonic transformation, and it is rotation invariant. The operator is an excellent measure of the spatial structure of local image texture, but by definition, it discards the other important property of local image texture, contrast. Therefore, the LBP measure can be further enhanced by combining it with a rotation invariant variance

measure that characterises the contrast of local image texture. Local variance is defined as

$$VAR_c = \frac{1}{P} \sum_{i=0}^{P-1} (g_i - \mu_c), \text{ where } \mu_c = \frac{1}{P} \sum_{i=0}^{P-1} g_i \quad (5.7)$$

Most approaches to texture analysis quantify texture measures by single values (e.g. mean, variance, entropy). However, much important information contained in the distributions of feature values might be lost. In this study, the final texture feature is the histogram of  $LBP_{c,j}$  occurrence, computed over an image or a region of an image. Additionally, the joint distribution of the two complementary  $LBP_{c,j}$  and  $VAR_c$  operators is taken. This joint distribution is approximated by a discrete two-dimensional histogram of size  $b(P+2)$ , where  $P$  is the number of neighbours in a circular neighbourhood and  $b$  is the number of bins for  $VAR_c$ . Ojala, Pietikäinen and Mäenpää (2002) show that this is a powerful tool for rotation invariant texture classification. The number of bins used in quantisation of the feature space plays a crucial role. Histograms with too modest a number of bins fail to provide enough discriminative information about the distributions. If the number of entries per bin is very small (i.e. too many bins), histograms become sparse and unstable. In this study, following Ojala et al. (1996), the feature space is quantised by computing the total feature distribution of  $LBP_{c,j}, VAR_c$  for the whole image. This distribution is divided into 32 bins having an equal number of entries.

In texture classification the (dis)similarity of sample and model histograms as a test of goodness-of-fit is evaluated using a nonparametric statistic, the log-likelihood ratio statistic, also known as the  $G$ -statistic (Sokal and Rohlf, 1987). The  $G$ -statistic is defined as

$$G = 2 \left( \left[ \sum_{s,m} \sum_{i=1}^{tb} f_i \log f_i \right] - \left[ \sum_{s,m} \left( \sum_{i=1}^{tb} f_i \right) \log \left( \sum_{i=1}^{tb} f_i \right) \right] - \left[ \sum_{i=1}^{tb} \left( \sum_{s,m} f_i \right) \log \left( \sum_{s,m} f_i \right) \right] + \left[ \left( \sum_{s,m} \sum_{i=1}^{tb} f_i \right) \log \left( \sum_{s,m} \sum_{i=1}^{tb} f_i \right) \right] \right) \quad (5.8)$$

where, the sample  $s$  is a histogram of the texture measure distribution of an image window, the model  $m$  is a histogram of a reference image window of a particular class,  $tb$  is the total number of bins and  $f_i$  is the probability in a bin.

By using a nonparametric test, no assumptions (possibly erroneous) about the feature distributions have to be made. The value of the  $G$ -statistic indicates the probability that two sample distributions come from the same population: the higher the value, the lower the probability that the two samples are from the same population. The more alike the histograms are, the smaller is the value of  $G$ .

The window size should be appropriate for the computation of the texture features. However, as windows of increased size are considered, the probability that regions contain a mixture of textures is increased. This can bias the comparison, since the reference textures contain only features of individual patterns. On the other hand, if the window size is too small it is impossible to calculate a texture measure. Within this constraint, it is impossible to define an optimum size for segmenting the entire image, therefore, classifying regions of a fixed window size is inappropriate (Aguado et al., 1998). Alternatively, a top-down hierarchical segmentation process, as discussed in the next section, offers a very suitable framework for classifying image regions based on texture.

## 5.6 Texture-based image segmentation

Split-and-merge segmentation, as described in the previous chapter, consists of a region-splitting phase and an agglomerative clustering (merging) phase (Horowitz and Pavlidis, 1976; Haralick and Shapiro, 1985; Lucieer and Stein, 2002). Objects derived with unsupervised segmentation have no class labels. Class labels can be assigned in a separate labelling or classification stage. In the unsupervised approach of Lucieer and Stein (2002) (also see chapter 4), the image was initially considered as a block of pixel values with mean vector and covariance matrix. This block was split into four sub-blocks characterised by vectors of mean pixel values and covariance matrices. To define homogeneity, a threshold for the mean and thresholds for the covariance matrix were considered. These values were chosen in advance and kept constant during segmentation. Heterogeneous sub-blocks were split recursively until homogeneity or a minimum block size was reached. The resulting data structure was a regular quadtree. In the clustering phase, adjacent block segments were merged if the combined object was homogeneous. The homogeneity rules were applied in a similar way. However, texture was not taken into account in this approach. Recently, Ojala and Pietikäinen (1999) applied a similar unsupervised split-and-merge segmentation with splitting and merging criteria based upon the  $LBP_{c,j}$ ,  $VAR_c$  texture measure.

Supervised segmentation uses explicit knowledge about the study area to train

the segmentation algorithm on reference texture classes. In a supervised approach, segmentation, objects with class labels are obtained. Aguado et al. (1998) introduced a segmentation framework with a top-down hierarchical splitting process based on minimising uncertainty. In this study, the  $LBP_{c,j}$ ,  $VAR_c$  texture measure and the segmentation framework as suggested by Aguado et al. (1998) are combined. Similar to split-and-merge segmentation each square image block in the image is split into four sub-blocks forming a quadtree structure. The criterion used to determine if an image block is divided is based on a comparison between the uncertainty of a block and the uncertainty of its sub-blocks.

Similar to split-and-merge segmentation each square image block in the image is split into four sub-blocks forming a quadtree structure. The criterion used to determine if an image block is divided is based on a comparison between uncertainty of a block and uncertainty of its sub-blocks. The image is segmented such that uncertainty is minimised, where uncertainty is defined as the ratio between the similarity values (G-statistic), computed for an image block  $B$ , of the two most likely reference textures. The reference textures are histograms of  $LBP_{c,j}$  and  $VAR_c$  of characteristic regions in the image. To test for similarity between an image block texture and a reference texture, the G-statistic is applied. Uncertainty  $U_B$  is then defined as

$$U_B = \frac{1 - G_2}{1 - G_1} \quad (5.9)$$

where  $G_1$  is the lowest  $G$  value of all classes (highest similarity) and  $G_2$  is the second lowest  $G$  value.  $U_B$  can contain values between 0.0 and 1.0.  $U_B$  is close to 1.0 if  $G_1$  and  $G_2$  are similar. In this case, the decision of classifying the region is vague. Segmentation uncertainty decreases if the difference between these two texture similarities increases. The subdivision of each image block is based on this uncertainty criterion. An image block is split into four sub-blocks if

$$U_B > \frac{1}{4}(U_{SB1} + U_{SB2} + U_{SB3} + U_{SB4}) \quad (5.10)$$

where the left side of equation 5.10 defines uncertainty when the sub-blocks are segmented according to the class obtained by considering the whole block  $B$ . The right side of equation 5.10 defines uncertainty obtained if the sub-blocks ( $U_{SB1}$ ,  $U_{SB2}$ ,  $U_{SB3}$  and  $U_{SB4}$ ) are segmented into the classes obtained by the subdivision. Thus, the basic idea is to subdivide an image block only if it is composed of several textures. Additionally, segmentation is always uncertain at the boundaries

of textures because the image block contains a mixture of textures. Accordingly, blocks that have at least one neighbouring region of a different class are subdivided until a minimum block size is reached (Aguado et al., 1998). Finally, a partition of the image with objects labelled with reference texture class labels can be obtained.

The building blocks of each of the objects give information about object uncertainty. The measure  $U_B$  is used to depict the uncertainty with which an object sub-block is assigned a class label. The spatial distribution of block uncertainty values within an object provides information about uncertainty in the spatial extent of objects. Therefore, high uncertainty values are expected for object boundary blocks, caused by mixed textures or transition zones.

## 5.7 Texture image example

To illustrate the problem of classifying regions of different texture an image (512 by 512 pixels) with a composition of photographs of five different textures from the Outex library (Ojala, Mäenpää, Pietikäinen, Viertola, Kyllönen and Huovinen, 2002) (figure 5.3(a)) was used. Each of these classes is unique in terms of their texture. It shows that the human visual system not only can distinguish image regions based on grey scale or colour, but also based on pattern. Five classes could be distinguished in figure 5.3(a), labelled class NW (granite), class NE (fabric), class SW (grass), class SE (stone) and class Centre (reed mat). A pixel-based classifier does not take into account texture or spatial information. This is shown in figure 5.3(b), which gives the result of a pixel-based classifier. In this case a supervised fuzzy  $c$ -means classifier using a Mahalanobis distance measure and a fuzziness value of 2.0 was applied (Bezdek, 1981; Zhang and Foody, 2001). Five reference regions of 40 by 40 pixels were selected in the centre of the five texture regions to train the classifier. Figure 5.3(b) shows that, although the patterns are still visible, no clear spatial partition of classes was found.

Figure 5.4 shows the results of two segmentations of figure 5.3(a). Figure 5.4(a) shows that a split-and-merge segmentation without texture characterisation, as described in chapter 4, cannot identify regions of homogeneous texture. It should be noted that this approach was unsupervised (no reference data were used to train the algorithm) (Lucieer and Stein, 2002). Random grey values were used to depict different objects. Figure 5.4(b) shows a segmentation result from an unsupervised split-and-merge segmentation algorithm with the  $LBP_{c,j}$ ,  $VAR_c$  histograms to model texture (Ojala and Pietikäinen, 1999). Good results were obtained since the spatial partition corresponds to the five different texture classes in the texture

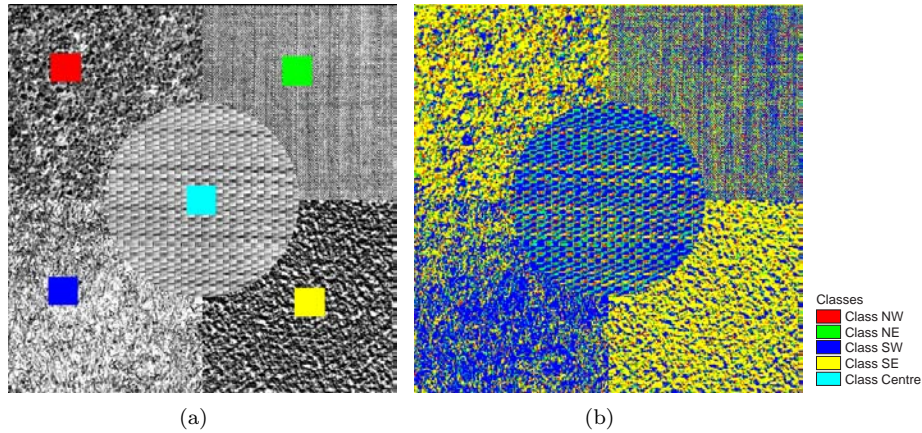


Figure 5.3: Pixel-based classification of texture image: (a) Artificial composition of five different natural textures (source: Ojala, Mäenpää, Pietikäinen, Viertola, Kyllönen and Huovinen (2002)); (b) Pixel-based supervised fuzzy  $c$ -means classification.

composite.

Figure 5.5 shows the results of a supervised texture-based segmentation of figure 5.3(a). The uncertainty criteria proposed by Aguado et al. (1998) were applied to obtain this result. Five reference regions were selected in the image, corresponding to the five different texture classes (similar to the supervised fuzzy  $c$ -means classification). Values for  $P$  and  $R$  were 8 and 1 respectively (corresponding to the 8 adjacent neighbours). Figure 5.5(a) shows the segmented objects with their corresponding class label. In figure 5.5(b) uncertainty values ( $U_B$ ) for each of the objects' building blocks are given. Class NE was segmented with lowest uncertainty values, between 0.3 and 0.4. The centre class was segmented with uncertainty values between 0.4 and 0.5. Class SE was segmented correctly, but with higher uncertainty values, between 0.5 and 0.7. Confusion of this class occurred with class SW. Class NW was segmented correctly, but with high uncertainty values between 0.5 and 0.75. In class NW a cluster of small objects was segmented as class SW. The building blocks of these objects showed uncertainty values of 0.95 and higher. Confusion of this class occurred with class SE. The main area of class SW was segmented correctly. In this class, small objects were segmented as class NW, SE and Centre, however, block uncertainty values were higher than 0.94 for these objects. This type of texture, however, was very irregular (i.e. its pattern was not repetitive and the reference area did not fully represent the whole texture

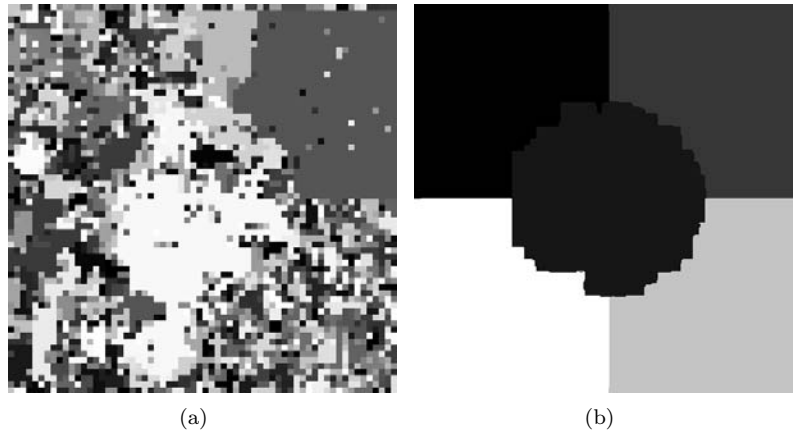


Figure 5.4: Unsupervised split-and-merge segmentation: (a) Segmentation of figure 5.3(a) based on mean and variance; (b) Segmentation based on  $LBP_{c,j}, VAR_c$  texture histograms

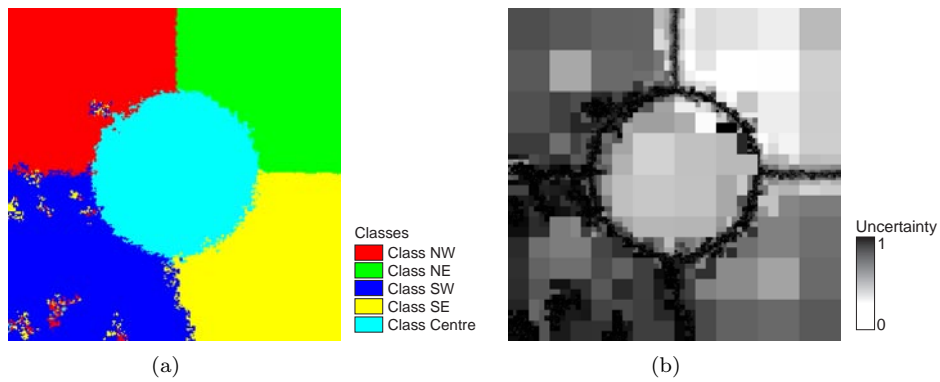


Figure 5.5: Supervised texture-based segmentation: (a) Texture-based segmentation of figure 5.3(a) with five reference classes; (b) Related uncertainty for all object building blocks.

area). In addition, all small blocks at the boundaries of textures showed high uncertainty values ( $> 0.9$ ), because they contained mixtures of different textures.

An accuracy assessment of the segmentation results provided an overall accuracy of 96.20% and a Kappa coefficient of 0.95. The confusion matrix with per-class accuracy percentages is given in table 5.1. These accuracy values show that good segmentation results can be obtained with the LBP texture measure.

Table 5.1: Confusion matrix with per-class accuracy values % for segmentation of texture image

Class	Reference					Total
	Class NW	Class NE	Class Centre	Class SW	Class SE	
Class NW	97.03	0.67	0.93	1.97	0.00	20.34
Class NE	0.00	96.37	0.02	0.00	0.00	19.44
Class Centre	0.59	1.62	95.99	0.39	0.24	19.48
Class SW	2.08	0.00	1.17	94.79	2.97	20.18
Class SE	0.30	1.34	1.89	2.85	96.79	20.56
Total	100.00	100.00	100.00	100.00	100.00	100.00

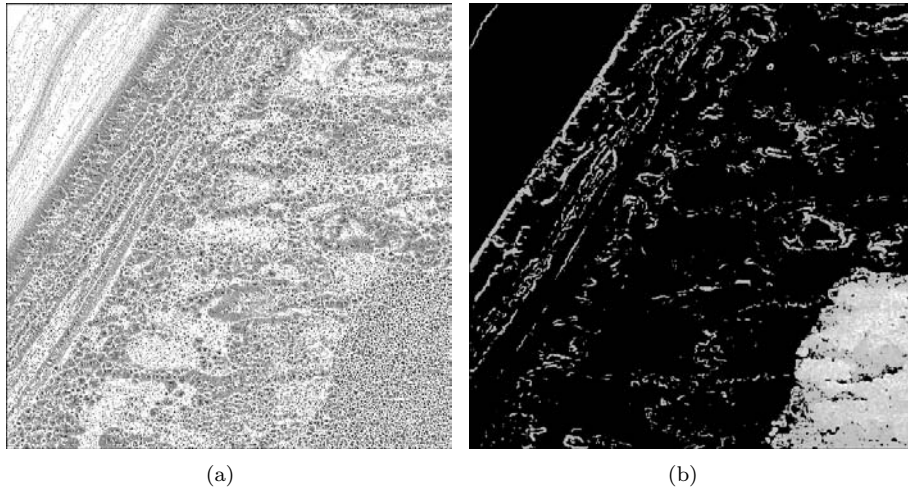


Figure 5.6: Texture measures for LiDAR DSM: (a) Image of the  $LBP_{c,j}$  measure for  $P = 8$  and  $R = 1$ ; (b) Image of the  $VAR_c$  measure for  $P = 8$  and  $R = 1$ .

## 5.8 Segmentation of LiDAR DSM

Figure 5.6 shows two images of the  $LBP_{c,j}$  and  $VAR_c$  texture measures of the LiDAR DSM of the study area (figure 5.1(b)). These images provided a basis for the texture-based segmentation algorithm to segment the area into meaningful land form objects.

Figure 5.7 shows the result of a supervised segmentation of a 512 by 512 pixel subset of the LiDAR DSM of the study area (figure 5.1(b)). Four reference areas of 40 by 40 pixels were selected for training. These areas represented the following

land form classes: beach, dune, dune slack and woodland. Values for  $P$  and  $R$  were 8 and 1 respectively. Figure 5.7(a) shows the segmented objects with class labels and figure 5.7(b) shows the corresponding uncertainty values ( $U_B$ ). Woodland was used as one of the land form classes, as it showed a characteristic texture in the LiDAR DSM. The woodland area was segmented correctly, with low uncertainty values ranging from 0.02 to 0.35. Uncertainty values increased at the border of the woodland area. Fieldwork showed that zones of willow trees occurred at the border of the main pine woodland area, which explained the higher uncertainty because of their slightly different texture. Dune slacks and blowouts are very similar in form. Blowouts are active, however, and not vegetated. Dune slacks are often stable, because they are vegetated. These texture differences could not be observed in the LiDAR DSM. Therefore, these units were segmented as a single class type, called dune slacks. The core of these areas was segmented correctly, with uncertainty values between 0.2 and 0.5. The boundaries of these objects, however, showed uncertainty values of 0.8 and higher. These high values can be explained by the transition zones from dune slacks to dune. No crisp boundary can be observed between these object types. Furthermore, figure 5.7 shows that no distinction could be made between the fore dune and the inland dune field. These areas have similar textures and, therefore, were segmented as one class. The (steep) fore dune showed, as expected, a short transition zone to the beach, depicted by high uncertainty values ( $> 0.8$ ) shown as a thin black line in the upper left corner of figure 5.7(b). The dune area was segmented with low uncertainty values ( $< 0.4$ ), except for the transition zones with the dune slacks. In the southwest and centre part of the image, small objects (with uncertainty values of 0.95) were incorrectly segmented as beach. This can be explained by observations in the field showing that this area is an active flat and bare sand area, with similar texture to the beach area. The beach flat was segmented early in the segmentation process, as can be concluded from the large building blocks. Uncertainty related to the segmentation of these building blocks varied between 0.1 and 0.5. Within the beach area, highest uncertainty occurred in areas where sand was wet and showed a different texture from dry sand.

Fieldwork provided reference data for segmentation validation. An accuracy assessment of the segmentation results provided an overall accuracy of 85.59% and a Kappa coefficient of 0.81. The confusion matrix with per-class accuracy percentages is given in table 5.2. It can be concluded from this table that small areas of both beach and dune were incorrectly labelled as dune slack.

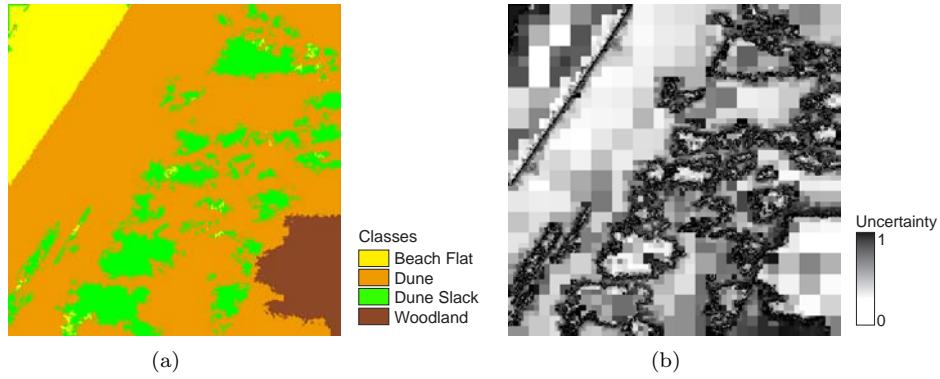


Figure 5.7: Segmentation result LiDAR DSM: (a) Supervised texture-based segmentation of the LiDAR DSM with four reference land form classes; (b) Related uncertainty for all object building blocks.

Table 5.2: Confusion matrix with per-class accuracy values % for segmentation of LiDAR DSM

Class	Reference				Total
	Beach Flat	Dune	Dune Slack	Woodland	
Beach Flat	100.00	0.00	3.24	0.00	27.16
Dune	0.00	100.00	1.56	0.00	16.54
Dune Slack	0.00	0.00	95.20	0.00	25.07
Woodland	0.00	0.00	0.00	100.00	31.24
Total	100.00	100.00	100.00	100.00	100.00

## 5.9 Segmentation of CASI image

Figure 5.8 shows two images of the  $LBP_{c,j}$  and  $VAR_c$  texture measures of band 12 of the CASI image of the study area (figure 5.1(a)). These images provided a basis for the texture-based segmentation algorithm to segment the area into meaningful land cover objects.

In figure 5.9, the results of the segmentation of the CASI image (figure 5.1(a)) are shown. The image was resampled to a spatial resolution of 2 m to match the spatial resolution of the LiDAR DSM. Again, a subset of 512 by 512 pixels was used for segmentation. Band 12 at 780 nm (NIR) was chosen for this study, as it is suitable for discrimination of land cover types. Figure 5.9(a) shows the segmentation result for four land cover types: sand, marram grass, willow shrub, woodland. Four reference areas of 50 by 50 pixels were selected to train the

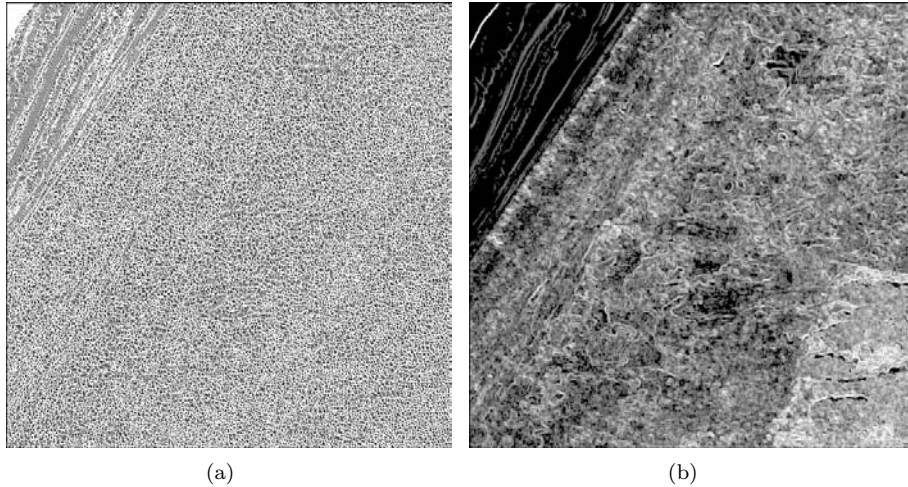


Figure 5.8: Texture measures for band 12 of CASI image: (a) Image of the  $LBP_{c,j}$  measure for  $P = 8$  and  $R = 1$ ; (b) Image of the  $VAR_c$  measure for  $P = 8$  and  $R = 1$ .

algorithm. Values for  $P$  and  $R$  were 8 and 1 respectively. The woodland area in the southeast corner of the image was correctly segmented with uncertainty values between 0.1 and 0.5 (figure 5.9(b)). The northeastern corner of the image and several small objects in the northern part of the image were also segmented as woodland. However, fieldwork showed that no woodland occurred in this area. This area was characterised by a chaotic pattern of dune slacks and dune ridges with a mixture of vegetation types. No homogeneous textures could be found, therefore this area showed high uncertainty values ( $> 0.7$ ) in the segmentation result. The main part of the dune field was segmented as willow shrub land. Fieldwork showed that marram grass is mainly found on the fore dune and on the highest parts of the dune ridges in the dune field. Only a few small patches of marram grass occur in figure 5.9(a) in the fore dune area. Willow shrub was found all over the dune field, but mainly in the dune slacks. Image texture for these two classes, however, was very similar. Marram grass fields were characterised by a mixture of grass and sand; willow shrub areas were characterised by a mixture of small willow shrubs and sand or low grass. High uncertainty values (higher than 0.7 in the dune field and higher than 0.95 in the fore dune and dune ridge areas) in figure 5.9(b) confirmed the confusion between these two classes. The sand cover on the beach was correctly segmented, because of its characteristic texture. Uncertainty values were lower than 0.2. Again, figure 5.9(b) shows a

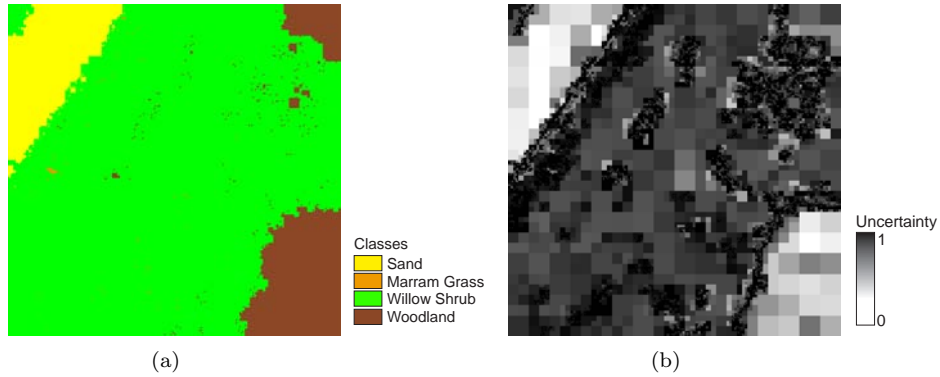


Figure 5.9: Segmentation result band 12 CASI image: (a) Supervised texture-based segmentation of band 12 of the CASI image with four reference land cover classes; (b) Related uncertainty for all object building blocks.

Table 5.3: Confusion matrix with per-class accuracy values % for segmentation of CASI image

<i>Class</i>	<i>Reference</i>					<i>Total</i>
	<i>Sand</i>	<i>Marram Grass</i>	<i>Willow Shrub</i>	<i>Woodland</i>		
<i>Sand</i>	100.00	0.00	0.00	0.00	0.00	26.42
<i>Marram Grass</i>	0.00	0.00	0.22	0.00	0.00	0.06
<i>Willow Shrub</i>	0.00	98.94	99.78	0.00	0.00	41.99
<i>Woodland</i>	0.00	1.06	0.00	100.00	100.00	31.54
<i>Total</i>	100.00	100.00	100.00	100.00	100.00	100.00

short transition zone from the fore dune to the beach with a decreasing marram grass coverage (narrow zone with uncertainty values of 0.95 and higher southeast of the sand area).

An accuracy assessment of the segmentation results provided an overall accuracy of 70.53% and a Kappa coefficient of 0.61. The confusion matrix with per-class accuracy percentages is given in table 5.3. It can be concluded from this table that major marram grass areas were incorrectly segmented as willow shrub.

## 5.10 Discussion and conclusions

In this chapter, a texture-based supervised segmentation algorithm derived labelled objects from remotely sensed imagery. Texture was modelled with the joint

distribution of LBP and local variance. The segmentation algorithm was a hierarchical splitting technique, based on reducing uncertainty at the level of the image blocks that are obtained. By applying this technique, one does not only obtain a texture-based image segmentation, but also an indication of uncertainty for all object building blocks. The spatial distribution of uncertainty values provided information about the location and width of transition zones. This study showed that object uncertainty values provide important information to identify transition zones between fuzzy objects.

The proposed algorithm provided good segmentation results for a test case study with a composite image of five different textures. An overall accuracy of 96.20% was obtained. To illustrate the algorithm for mapping coastal objects, a LiDAR DSM and CASI image of a coastal area on the northwest coast of England were used. Good segmentation results were obtained for the extraction of land form objects from the LiDAR DSM, depicted by an overall accuracy of 86%. Uncertainty values provided meaningful information about transition zones between the different land forms. Land cover objects derived from the CASI image showed high uncertainty values and many incorrectly labelled objects. The overall accuracy was 71%. The woodland area showed a characteristic texture in both data sources, however, the woodland object showed a different spatial extent and area in both segmentation results. This difference was caused by the occurrence of small patches of willow trees in, and on the border of, the woodland area. The texture of these willow trees is different from the pine trees in the area in the LiDAR DSM. The segmentation result of the LiDAR DSM correctly depicted the spatial extent of the pine area. However, the texture difference did not occur in the CASI image, resulting in a different segmentation result.

This and other segmentation errors can possibly be prevented by taking into account spectral information from more than one band. The combination of textural and spectral information from all 14 CASI bands could greatly improve segmentation results. This combination could be useful for mapping other land cover types in the area, like grasses, herbaceous plants, mosses, and shrubs. Additionally, the resolution of the neighbourhood set of the LBP measure affects the segmentation result. In this study, a neighbourhood set of the nearest eight neighbouring pixels ( $P = 8, R = 1$ ) was used. A multi-resolution approach with different combinations of  $P$  and  $R$  might improve texture description.

*5.10. Discussion and conclusions*

---

## Chapter 6

# Multivariate Texture-based Segmentation\*

*For those who have seen the Earth from space . . .  
the experience most certainly changes your perspective.  
The things that we share in our world are far more valuable  
than those which divide us.*

D. Williams

### 6.1 A multivariate texture model

The LBP texture measure, as described in chapter 5, allows a texture description of a single band. Most remote sensing images, however, consist of multiple bands. Segmentation of land cover objects based on a single CASI band in chapter 5 showed that unsatisfactory results were obtained. Including multiple bands might

---

\*This chapter is based on the following papers:

Lucieer, A., Stein, A. and Fisher, P. F. (in review ). Multivariate texture-based segmentation of remotely sensed imagery for extraction of objects and their uncertainty, *International Journal of Remote Sensing* . in review.

Lucieer, A., Orkhonselenge, T. and Stein, A. (2004). Texture based segmentation for identification of geological units in remotely sensed imagery, in A. Frank and E. Grum (eds), *Proceedings of the 3<sup>rd</sup> International Symposium on Spatial Data Quality ISSDQ'04*, Technical University of Vienna, Bruck an der Leitha, Austria, pp. 117–120.

---

improve segmentation considerably, as a combination of bands provides more spectral information for identification of different land cover types.

In their psychophysical study Poirson and Wandell (1996) showed that colour and pattern information are processed separately by the human visual system. Mojsilovic et al. (2000) extracted colour-based information from the luminance and chrominance colour components. The achromatic pattern component was utilised as texture pattern information. Another approach is that of Panjwani and Healey (1995) which captured spatial relations both within and between colour bands with Markov random fields (MRFs). More recently, Pietikäinen et al. (2002) showed that the powerful LBP texture measure can also be applied to colour images. They processed colour information and texture information separately and obtained good classification results for colour texture images. Most research on colour texture is focused on images of different materials with a well-defined texture. In standard RGB-images the pattern in the different colour bands is often highly correlated. This makes it possible to summarise pattern information in a single band and process it separately from colour information. In remote sensing images information is recorded from different parts of the spectrum, therefore, texture in these bands is not necessarily similar. In between band relations should be taken into account when looking at multivariate texture measures for remotely sensed imagery. The LBP texture measure, described in chapter 5 is a robust, rotation invariant and flexible texture measure. An extension to the multivariate case is expected to provide good segmentation results.

In this chapter the new Multivariate Local Binary Pattern operator,  $MLBP_c$ , is introduced and implemented. It is based on the univariate  $LBP_{c,j}$  measure, describing local pixel relations in three bands, also known as colour texture. In addition to spatial relations of pixels within one band, pixel relations between bands are also considered. Thus, the neighbourhood set for a pixel consists of the local neighbours in all three bands. The local threshold is taken from these bands, which makes up a total of nine different combinations (figure 6.1). This results in the following operator for a local colour texture description

$$MLBP_c = \sum_{i=0}^{P-1} \begin{matrix} sign(g_i^{b1} - g_c^{b1}) + sign(g_i^{b2} - g_c^{b1}) + sign(g_i^{b3} - g_c^{b1}) + \\ sign(g_i^{b1} - g_c^{b2}) + sign(g_i^{b2} - g_c^{b2}) + sign(g_i^{b3} - g_c^{b2}) + \\ sign(g_i^{b1} - g_c^{b3}) + sign(g_i^{b2} - g_c^{b3}) + sign(g_i^{b3} - g_c^{b3}) \end{matrix} \quad (6.1)$$

where  $b1$  is the first band,  $b2$  is the second band, and  $b3$  is the third band. The first part of the equation calculates LBP values for the center pixel of the first

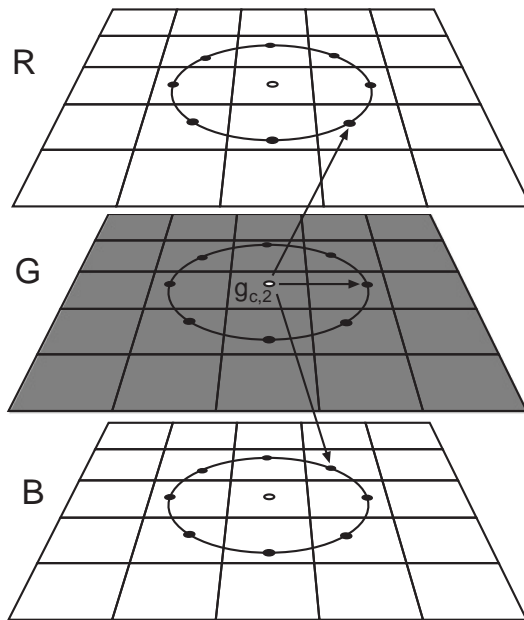


Figure 6.1: The neighbourhood set for the multivariate (three band) case not only takes into account the spatial relations within each of the bands, but also the relations between the bands.

band based on relations with the neighbors in the first band and the two other bands. The second part of the equation calculates LBP values for the center pixel of the second band and the third part of equation 6.1 calculates LBP values for the center pixel of the third band. Each of the three central pixels is, therefore, compared with neighborhood pixels in the other bands.  $MLBP_c$  is not just a summation of  $LBP_{c,j}$  of individual bands, it also models pixel relations between bands. These cross-relations can be important in the distinction of different color textures. A total of nine LBP values is obtained and summed to derive  $MLBP_c$ . The color texture measure is the histogram of  $MLBP_c$  occurrence, computed over an image or a region of an image. This single distribution contains  $3^2P$  bins (for  $P = 8$  resulting in 72 bins).

$MLBP_c$  measures the binary colour pattern of a texture. To complete this measure with contrast and variance information the colour histogram RGB-3D is

included, adopted from Pietikäinen et al. (2002). Each 8-bit band is quantised into 32 levels by dividing the pixel values on each band by 8, resulting in a three-dimensional histogram with  $32^3$  entries. The similarity measure for the  $MLBP_c$  and RGB-3D histograms is the G-statistic (equation 5.8). The sum of these two G-statistic values is used as a similarity measure in a top-down hierarchical splitting segmentation to obtain image block class labels and uncertainty values (Aguado et al., 1998).

## 6.2 Colour texture example

To illustrate the solution for classifying regions of different colour texture, a three-band image (512 by 512 pixels) with a composition of six different colour textures (figure 6.2(a)) was used. This colour texture image was composed of textures from the Outex library (Ojala, Mäenpää, Pietikäinen, Viertola, Kyllönen and Huovinen, 2002). The following textures were used: Upper Left (UL) = fur, Upper Right (UR) = carpet, Middle Left (ML) = wood, Middle Right (MR) = pasta, Lower Right (LR) = flour, Lower Left (LL) = seeds. Segmentation of this image provided a complex task as textures at different scale levels occur and variation in colour is high in this image. Six reference regions of 40x40 pixels were selected, corresponding to the six different texture classes. Values for  $P$  and  $R$  were 8 and 1 respectively. Figure 6.2(b) shows the segmentation result. All regions were identified correctly with only a few small object blocks incorrectly segmented. In the lower left object some dark spots were segmented as fur (Upper Left), most likely caused by similarity in colour distributions. Additionally, in the lower right object some dark shadow spots were (mis-)segmented as flour (Lower Left). Uncertainty for incorrectly segmented object blocks and boundary zones was high ( $> 0.9$ ) (figure 6.2(c)).

An accuracy assessment of the segmentation results provided an overall accuracy of 98.32% and a Kappa coefficient of 0.98. The confusion matrix with per-class accuracy percentages is given in table 6.1. These accuracy values show that good segmentation results can be obtained with the multivariate LBP texture measure.

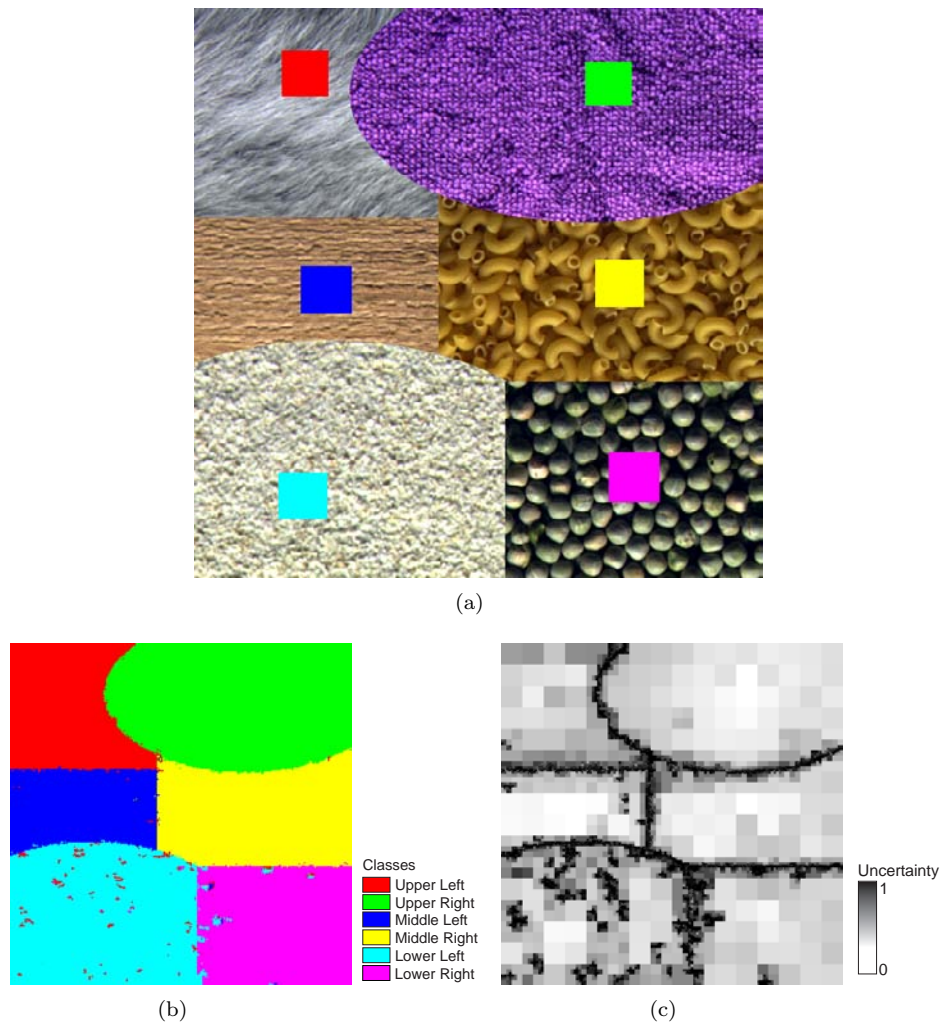


Figure 6.2: Segmentation of colour textures: (a) Artificial composition of six different natural colour textures; (b) Supervised texture-based segmentation based on the multivariate  $MLBP_c$  distribution and RGB-3D colour histogram with six reference classes; (c) Related uncertainty for all object building blocks.

Table 6.1: Confusion matrix with per-class accuracy values % for segmentation of texture image

Class	Reference						Tot.
	UL	UR	ML	MR	LL	LR	
UL	99.93	0.56	1.31	0.26	1.91	0.38	12.72
UR	0.02	99.41	0.03	1.59	0.02	0.02	24.11
ML	0.05	0.00	98.09	0.05	0.12	0.21	9.62
MR	0.00	0.02	0.02	97.82	0.02	0.09	16.44
LL	0.00	0.01	0.55	0.10	97.68	2.30	21.77
LL	0.00	0.00	0.00	0.16	0.26	97.00	15.35
Tot.	100.00	100.00	100.00	100.00	100.00	100.00	100.00

### 6.3 Multivariate texture segmentation of a CASI image

In chapter 5 land cover units were segmented from a single CASI image band. Segmentation with one CASI band (band 12 in section 5.9) discarded valuable information in other bands. Fieldwork showed that these single band segmentation results were generally poor. The willow shrub area was over-segmented, whereas, marram grass on the dune ridge did not occur in the segmentation result. A multivariate approach towards texture segmentation might improve segmentation. The combined  $MLBP_c$  and RGB-3D texture measure, models texture in three bands. CASI band 1, 8 and 12 explain most of the variance in the image scene and characterise land cover classes well. Figure 6.3 shows a supervised segmentation based on the multivariate  $MLBP_c$  measure, and the three-dimensional colour histogram RGB-3D. Figure 6.3(b) shows that segmentation of the marram grass class has improved considerably. The fore dune area and the dune ridges are segmented as marram grass, as was observed in the field. The core areas show low uncertainty values, whereas the boundaries show high uncertainty values. This corresponds to observations that marram grass gradually changes to willow shrub land and sandier terrain. The woodland area is segmented correctly. In addition, segmentation of the north-eastern part of the area (marram grass and willow shrub) has improved, as the incorrect segmentation result of a single band showed woodland in this area. The beach area was correctly segmented with low uncertainty values. Some small incorrectly segmented blocks (marram, willow and woodland) occurred in the beach area where the sand was wet. This wet area showed a lower reflectance in the image. High uncertainty values ( $> 0.9$ ) occurred in all transition areas, indicating occurrence of fuzzy objects with indeterminate boundaries.

An accuracy assessment of the segmentation results provided an overall ac-

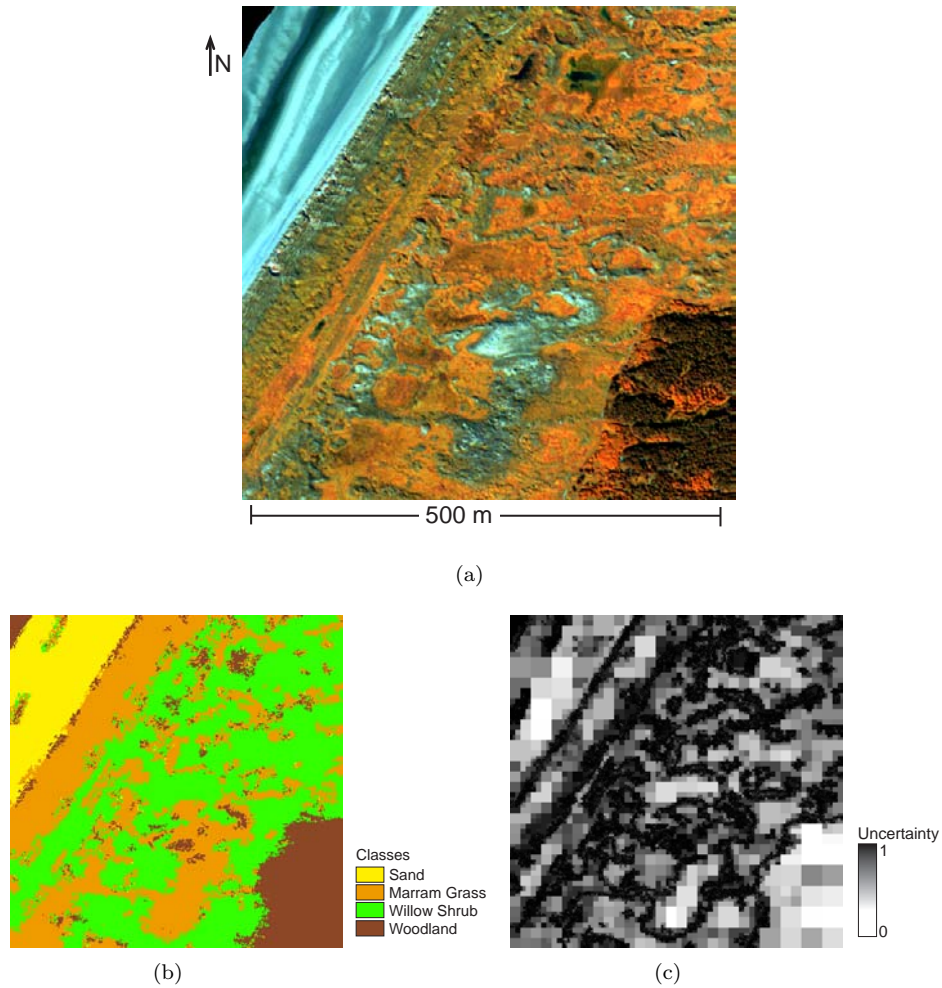


Figure 6.3: Segmentation of land cover from a 3-band CASI image: (a) Colour composite of band 12, 8 and 1 of CASI image (b) Supervised texture-based segmentation based on the multivariate  $MLBP_c$  distribution and RGB-3D colour histogram with four land cover classes; (c) Related uncertainty for all object building blocks.

Table 6.2: Confusion matrix with per-class accuracy values % for multivariate texture-based segmentation of CASI image

<i>Class</i>	<i>Reference</i>				Total
	Sand	Marram Grass	Willow Shrub	Woodland	
Sand	100.00	0.00	2.38	0.00	26.96
Marram Grass	0.00	96.92	20.29	0.00	20.98
Willow Shrub	0.00	2.11	64.77	0.00	17.34
Woodland	0.00	0.97	12.55	100.00	34.73
Total	100.00	100.00	100.00	100.00	100.00

curacy of 77.09% and a Kappa coefficient of 0.71. The confusion matrix with per-class accuracy percentages is given in table 6.2. It can be concluded from this confusion matrix that segmentation of marram grass and willow shrub improved considerably compared to segmentation based on one CASI band. However, some of these areas remain incorrectly segmented.

## 6.4 Identification of geological units in Mongolia

To illustrate the use of texture-based segmentation for identification of objects, an additional study was carried out. Textural information derived from remotely sensed imagery can be helpful in identification of geological units. These units are often mapped based on field observations or interpretation of aerial photographs. Geological units often show characteristic image texture features, for example in the form of fracture patterns. Pixel-based classification methods might, therefore, fail to identify these units. A texture-based segmentation approach, taking into account spatial relations between pixels, can be helpful to identify geological units from an image scene.

### 6.4.1 Study area and geological map

The study area is located in Dundgovi Aimag, Southern Mongolia ( $105^{\circ}50'$ – $106^{\circ}26'$  E and  $46^{\circ}01'$ – $46^{\circ}18'$  N). The total area is 1415.58 km<sup>2</sup>. The area is characterised by an arid, mountainous-steppe zone with elevations between 1300 m and 1700 m. The area is sparsely vegetated and weathering and erosion are intensive.

In the 1950's and 1970's, geological mapping and surveying was carried out at a scale of 1:200 000 and 1:1000 000. In 2004 an accurate image interpretation was

carried out to derive a recent geological map. The following geological units can be found in the area:

1. Sedimentary rocks

- Q4 — Quaternary Lakes sediments
- Q — Quaternary sediments
- E2 — Eocene (middle Paleogene)
- E1 — Miocene (lower Paleogene)
- P-T — Permian & Triassic formation

2. Volcanic rocks

- K2 — Upper Cretaceous basalt
- K1 — Lower Cretaceous basalt
- aT3-J1 — Upper Triassic & Lower Jurassic andesite

3. Intrusive rocks

- yT3-J1 — Upper Triassic & Lower Jurassic granite
- yPR — Proterozoic granite

### 6.4.2 Remote sensing imagery

Spectral data gathered through remote sensing can provide information about many features of the Earth's surface that are of interest to a geologist. Furthermore by combining surface observations with geologic knowledge and insights, geologists are able to make valid inferences about subsurface materials. Remote sensing imagery is useful for mapping geological units at a regional scale in isolated and inaccessible areas. Additionally, frequent updating of existing maps is possible with modern sensors like Landsat TM and the Advanced Spaceborne Thermal Emission and Reflection Radiometer (ASTER). In this study, two images were used for identification of geological units. Shortwave infrared (SWIR) bands are particularly useful for identification of these units (Richards and Jia, 1999; Drury, 1993). A Landsat 5 TM scene was acquired on the 13<sup>th</sup> of May, 1993. A colour composite of band 7, 5 and 4 of the Landsat TM scene of the study area is shown in figure 6.5(a).

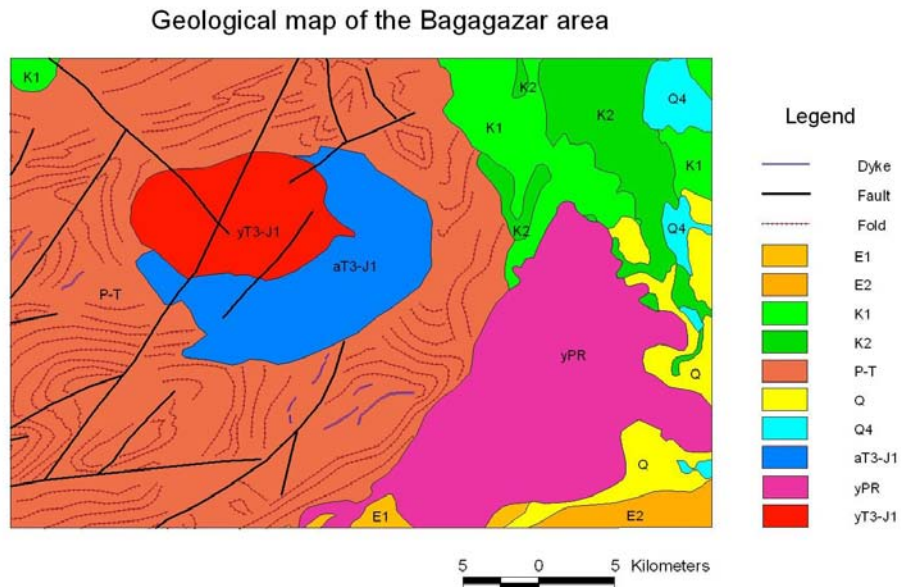


Figure 6.4: Geological map of the study area derived from image interpretation, 2004.

An ASTER scene was acquired on the 21<sup>st</sup> of May, 2002. ASTER Level 1B product contains radiometrically calibrated and geometrically co-registered data for all bands. The SWIR bands can detect spectral features of many common anionic constituents of minerals. These various anion groups form the bulk of the Earth's surface rocks. Since this case study focuses on identification of geological units, the ASTER SWIR bands provide most information for the extraction of information on rock and soil types. In figure 6.5(b) a colour composite of ASTER SWIR bands 9, 6 and 4 is given.

### 6.4.3 Segmentation results

Based on fieldwork a number of areas were selected as reference areas for supervised texture-based segmentation. The multivariate texture-based segmentation algorithm based on the  $MLBP_c$  and RGB-3D texture measure was applied to identify geological units in both images. Figure 6.6 shows the segmentation result

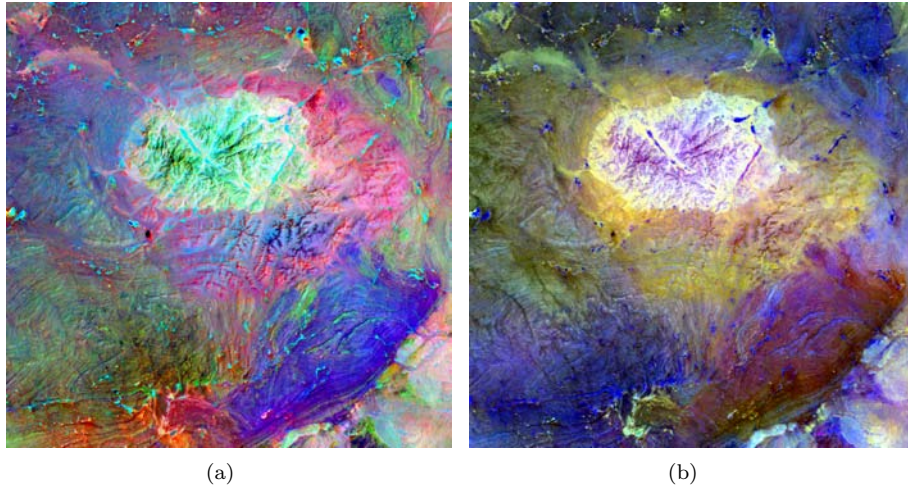


Figure 6.5: Landsat and ASTER images of the study area in Mongolia: (a) Colour composite of Landsat TM bands 7, 5 and 4; (b) Colour composite of ASTER SWIR bands 9, 6 and 4.

for the Landsat TM image. Visual comparison of figure 6.6(a) with the geological map (figure 6.5) shows that, overall, geological units were correctly identified. The main difference between the segmentation result and the geological map was that the segmented image showed more detail than the geological map. The aT3-J1, yPR and K2 units were correctly identified, but the K1 unit is more abundant in the segmentation result. High uncertainty values occurred in the wide transition zones (figure 6.6(b)).

SWIR bands 9, 8 and 4 were used for segmentation of the ASTER image. In this geological application this ASTER band combination is expected to give better segmentation results. ASTER Band 4 covers the same spectral region as Landsat band 5. ASTER band 5–8 are within the range of Landsat band 7, whereas ASTER band 9 is out of the Landsat spectral range. A visual comparison of the segmentation result in figure 6.7(a) with the geological map (figure 6.4) and the segmentation result based on the Landsat bands (figure 6.6(a)), showed that this result is better than the Landsat result. Units aT3-J1 and P-T were segmented correctly, however, some small objects surrounding the yT3-J1 unit were incorrectly segmented. This might have been caused by weathering processes, as the P-T unit was covered by deposited sediment. This area was segmented as K1. As expected, uncertainty was high in the transition zones, however, these zones were less wide than in the Landsat segmentation result.

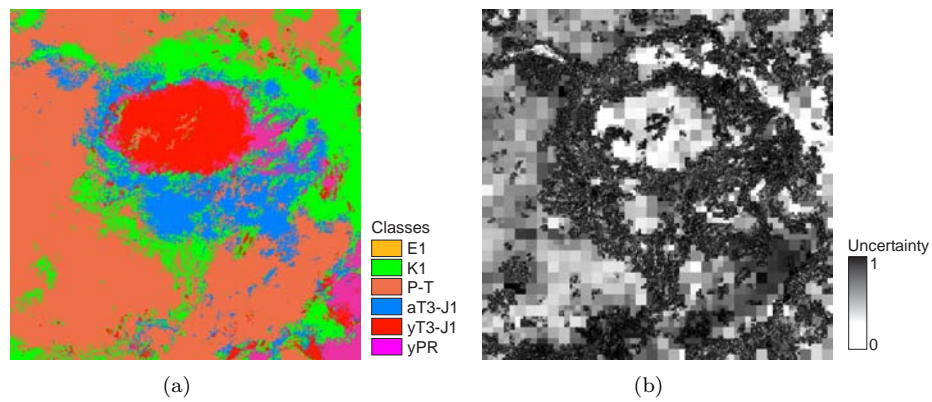


Figure 6.6: Segmentation of geological units from the Landsat TM image: (a) Geological units as identified by the multivariate texture-based segmentation algorithm; (b) Uncertainty values for each of the building blocks of the objects.

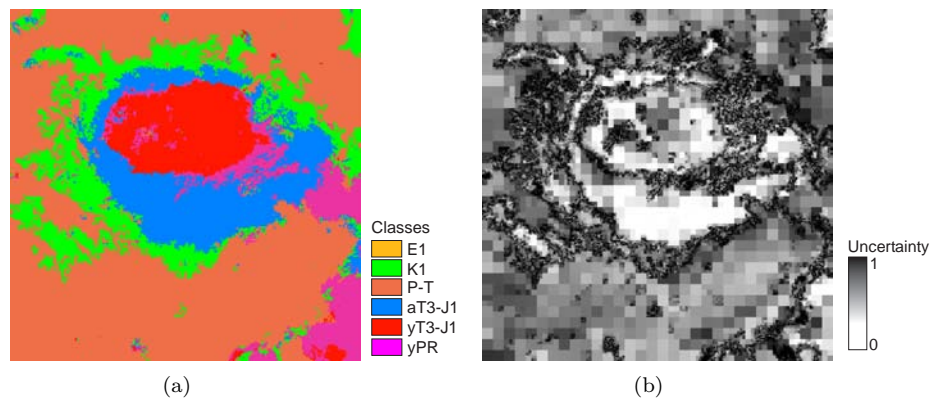


Figure 6.7: Segmentation of geological units from the ASTER image: (a) Geological units as identified by the multivariate texture-based segmentation algorithm; (b) Uncertainty values for each of the building blocks of the objects.

Table 6.3: Confusion matrix with per-class accuracy values % for segmentation of Landsat TM image

Class	Reference					Total
	PT	yT3J1	K1	aT3J1	yPR	
PT	67.29	2.79	23.02	6.63	5.86	49.28
yT3J1	1.41	80.11	0.43	1.53	15.79	9.55
K1	22.88	2.31	70.11	24.79	25.92	22.17
aT3J1	7.39	2.76	2.86	52.46	10.73	12.95
yPR	1.03	12.03	3.58	14.59	41.70	6.05
Total	100.00	100.00	100.00	100.00	100.00	100.00

Table 6.4: Confusion matrix with per-class accuracy values % for segmentation of ASTER image

Class	Reference					Total
	PT	yT3J1	K1	aT3J1	yPR	
PT	70.6	0.31	49.33	2.39	24.69	52.28
yT3J1	0.11	88.24	0	2.08	6.93	8.99
K1	19.13	0.1	45.68	10.02	6.84	15.95
aT3J1	6.92	3.07	4.65	69.93	4.72	14.65
yPR	3.24	8.28	0.34	15.58	56.83	8.14
Total	100	100	100	100	100	100

#### 6.4.4 Segmentation validation

For validation of the segmentation results the geological map (figure 6.4) was used as reference data. An initial visual comparison showed that most large objects correspond with the units in the geological map. However, many small objects occurred in the segmentation result. An accuracy assessment of the segmentation results of the Landsat TM segmentation provided an overall accuracy of 65.23% and a Kappa coefficient of 0.44. The confusion matrix with per-class accuracy percentages is given in table 6.3. An accuracy assessment of the segmentation results of the ASTER segmentation showed better results and provided an overall accuracy of 71.00% and a Kappa coefficient of 0.51. The confusion matrix with per-class accuracy percentages is given in table 6.4.

The main source for incorrect segmentation is the difference in detail between the segmentation results and the geological map. In the map, only the main geological units are given, however, the segmentation results provided more detail. A majority filter of 15 by 15 pixels was applied to filter out the smallest objects from the ASTER segmentation result. Visually, the segmentation result is very similar to the geological map (figure 6.8). However, the K1 unit is much more

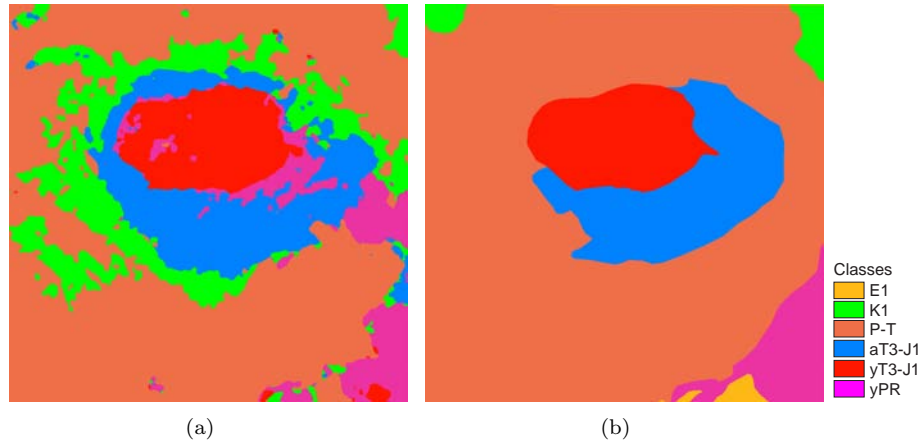


Figure 6.8: Comparison ASTER segmentation result with geological map: (a) Segmentation result based on ASTER SWIR bands after a 15 by 15 majority filter to reduce the amount of small objects; (b) Subset of the geological reference map corresponding to the area of the images.

abundant in the segmentation result. The original image clearly shows a distinctly different texture from the surrounding area, therefore, this area is segmented as a K1 instead of a P-T unit. The majority filtering operation did not provide higher accuracy values, as the total accuracy only increased by 0.5%.

## 6.5 Discussion and conclusions

In this chapter, a new texture measure was proposed to model multivariate texture or colour texture. The univariate  $LBP_{c,j}$  texture measure was extended to a multivariate measure, to model within and between band pixel relations in three bands. This multivariate extension,  $MLBP_c$ , in combination with the three-dimensional colour histogram, RGB-3D, models colour texture as registered on different bands. An artificial image with a composition of colour textures was used to demonstrate the use of colour texture in segmentation. Good segmentation results were obtained with the combined  $MLBP_c$  and RGB-3D texture measures, depicted by an overall accuracy of 98%. The first real world case study involved segmentation of a multi-spectral CASI image of a coastal area in England into four coastal land cover classes. Univariate segmentation of a single band of the CASI image,

as described in chapter 5, proved unsatisfactory. The multivariate texture model provided good segmentation results based on three CASI bands with an overall accuracy of 77%. Additionally, object uncertainty was quantified for each object building block. These uncertainty values provided information to identify transition zones between fuzzy objects, like marram grass on the dune ridges and willow shrub in the dune troughs.

The second case study involved identification of geological units from Landsat TM and ASTER imagery. Good segmentation results were obtained with the multivariate texture-based segmentation algorithm. Validation of the segmentation result of the ASTER image with a geological map provides an overall accuracy of 77%. The detail in the segmentation result, however, was much higher than in the geological reference map. The quality of the geological map is questionable as these type of maps are often obtained from a combination of field observations and image interpretation. Segmentation accuracy is only an indication of the correspondence between the geological map and the segmentation result, rather than an absolute accuracy value. Because of the higher detail in the segmentation result, segmentation might help to update existing geological maps.

The diversity of applications and images used in the case studies, shows that the described multivariate texture-based segmentation algorithm can be applied in a range of remote sensing applications. The segmentation performance, however, depends on the types of texture in the image. An image with regular homogeneous texture will be better segmented than a heterogeneous image with irregular textures. The univariate and multivariate LBP measures can also be used in a different framework. For example, contextual classification using the LBP texture measure might provide valuable results. The multivariate LBP measure was limited to three bands. More bands could have been used in both  $MLBP_c$  and RGB-3D texture models. However, a higher number of bands do not necessarily add more texture information. Additionally, increasing dimensionality, will result in a much higher computational demand. From a multivariate dataset, like hyper-spectral imagery for example, one could select three bands that explain most variance. Another option is to select the bands that are suitable for the application, like the SWIR bands for identification of geological units and the NIR bands to map land cover.

In chapter 5, a uniformity measure was defined for the univariate LBP measure. Ojala, Pietikäinen and Mäenpää (2002) showed that more than 90% of the patterns in a texture image are uniform. In remote sensing images non-uniform patterns occur as well and some of these may be characteristic for a specific land cover class. Hence, an extension of the uniformity measure to the multivariate case may provide more information on pattern uniformity. A multivariate uniformity

measure could be calculated by summation of uniformity in each band or by combining the uniformity measure for each of the nine components in the multivariate LBP measure (equation 6.1). The effect of a multivariate uniformity measure on segmentation of multispectral remote sensing imagery will be assessed in future research.

In this study, a neighbourhood set of the nearest eight neighbouring pixels was used. A multi-resolution approach with different combinations of neighbourhood sets might improve description of large-scale textures. A multi-scale approach to texture description is the focus of the next chapter.

## Chapter 7

# Multi-scale Texture for Land Form Segmentation \*

*There is nothing worse than a sharp image of a fuzzy concept.*

A. Adams, photographer

### 7.1 Introduction

Regions with similar reflection can easily be identified as objects on a remote sensing image. In case of a digital surface or elevation model (DSM or DEM) similarity in elevation could be used as a criterion to identify land form objects. These objects, however, are often characterised by more than just elevation. A dune ridge, for example, has a characteristic profile and/or shape, which shows a unique texture on a DEM. Therefore, it is argued that texture is an important property of land form objects and it should be taken into account in land form

---

\*This chapter is based on the following papers:

Lucieer, A. and Stein, A. (in press). Texture-based land form segmentation of LiDAR imagery, *International Journal of Applied Earth Observation and Geoinformation*.

Werff, H. M. A. v. d. and Lucieer, A. (2004). *Remote Sensing Image Analysis: Including the Spatial Domain*, Vol. 5 of *Remote Sensing and Digital Image Processing*, Kluwer Academic Publishers, Dordrecht, chapter A Contextual Algorithm for Detection of Mineral Alteration Halos with Hyperspectral Remote Sensing.

---

analysis.

The results from a land form segmentation in chapter 5 provided an initial coarse segmentation of the coastal study area into four general land form classes. One of the main shortcomings of this algorithm was the resolution at which the texture model operated. Only one neighbourhood set with  $P = 8$  and  $R = 1$  was used (equation 5.2). To identify land form objects with more detail and higher accuracy, patterns should be modelled at different scales, i.e. different values for  $P$  and  $R$  can be used to describe local patterns at different circle radii. Ojala, Pietikäinen and Mäenpää (2002) show that a multi-resolution LBP texture measure outperforms well-known texture models in segmenting texture images similar to figure 5.3(a). In land form analysis a multi-resolution or multi-scale approach might prove beneficial. For example, a small local neighbourhood set might fail to capture the pattern of a dune ridge on a DSM. The characteristic pattern of a dune ridge could, therefore, be described by combining pixel information from several neighbourhood sets at different scale levels.

Fisher et al. (2004) and Fisher et al. (in press) proposed a multi-scale analysis for allocating fuzzy memberships to morphometric classes. This technique was used to model objects, which are vague for scale reasons. The morphometry classes modelled at different scale levels were: channel, pass, peak, pit, plane, and ridge. Although this analysis failed to identify positions of dunes, it was possible to identify dune ridges and slacks and to monitor their changing positions. The use of textural information might improve identification of these coastal objects, as a description of texture reflects the spatial structure of elevation and slopes. This information is indispensable in classifying an area into sensible land form units. However, a multi-scale approach to texture description is required.

In this chapter, a region growing algorithm is implemented and applied. It is based on textural information from the LBP operator to extract landform objects from a DSM. A description of texture reflects the spatial structure of elevation and slopes, and is therefore indispensable in segmenting an area into sensible landform units. Land form segmentation is started by modelling texture using the LBP operator at different scales. Then, objects are formed by seeded region growing. This process starts at the finest pixel level and it clusters pixels to form objects based on textural homogeneity. Growing of objects is stopped if a certain threshold is exceeded. A similarity measure is used to determine whether a pixel can be merged with an object. This measure also provides useful information on extensional uncertainty of objects, expressing uncertainty in their spatial extent. It is expected that pixels in transition zones show higher uncertainty values than pixels in core areas with homogeneous textures. To illustrate the use of texture-based

segmentation for identification of landform objects, a LiDAR DSM of a coastal area in northwest England is used. This chapter builds on work presented in chapters 4 and 5 and further explores the use of multi-scale texture and generation of extensional object uncertainty in image segmentation to identify fuzzy land form objects. The main advantage of the approach taken in this study is that land form objects can be extracted from elevation data in an objective and fully automated manner.

## 7.2 Multi-scale texture model

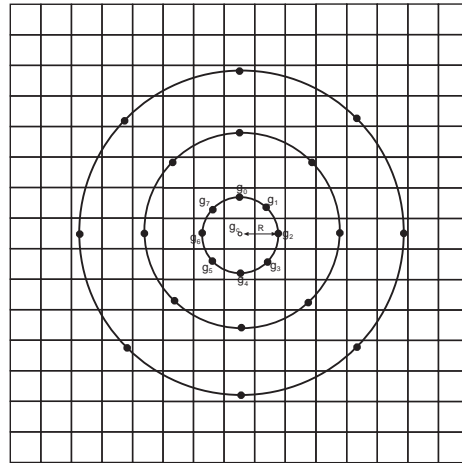
The LBP texture measure as described in chapter 5 proved to be a suitable description for local image texture. The definition for the local neighbourhood set in equation 5.2 allows for selection of neighbourhood sets at different scale levels, i.e. different combination of  $P$  and  $R$  (for example  $P=8, R=1$ ;  $P=8, R=5$ ;  $P=8, R=10$ ). The LBP measure, defined in equation 5.4 can be extended to a multi-scale texture measure taking into account spatial information at more than one scale level. To include texture at different scale levels,  $N$  neighbourhood sets at different resolutions are taken to calculate local binary patterns (figure 7.1(a)). For each neighbourhood set  $LBP_c$  (equation 5.4) and  $VAR_c$  (equation 5.7) are calculated. The multi-scale texture measure is defined by

$$LBP_c^N = \sum_{n=1}^N LBP_c^n \quad (7.1)$$

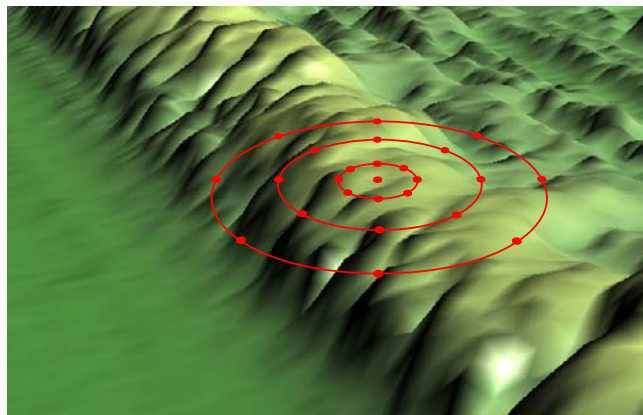
where  $n$  is a combination of  $P$  and  $R$ . The multi-scale variance measure  $VAR_c^N$  is calculated over all neighbours at the different scale levels. Figure 7.1(b) illustrates why a multi-scale neighbourhood might be seen appropriate for land form description.

## 7.3 Seeded region growing

In this study, a seeded region growing image segmentation algorithm (Haralick and Shapiro, 1985; Horowitz and Pavlidis, 1976) is applied to identify and extract land form objects. Initialisation of seed pixels is an important issue, because it strongly influences the segmentation result. A random initialisation of seeds is a



(a)



(b)

Figure 7.1: Multi-scale circular neighbourhood set: (a) Neighbourhood set for different values of  $P$  and  $R$ ; (b) Neighbourhood set super imposed on a 3D representation of a LiDAR DSM to show its usefulness for describing land forms.

first option, although for every segmentation a different result is obtained. Alternatively, segmentation can be started at locations with minimal local variance. To calculate local variance for every pixel in the image, equation 5.7 is applied with  $P = 8$  and  $R = 1$ , corresponding to a 3 by 3 kernel. Next, the list of pixels is sorted based on variance. Segmentation is started at pixels with the lowest variance values. A similarity criterion is used to merge adjacent pixels to form an image object. An initial similarity criterion for grey-scale images is the difference between the mean value of an object and a candidate pixel. If the difference is smaller than a certain threshold, the pixel is merged with the object. To deal with multi-spectral or hyper-spectral data, either the spectral angle or the Euclidean distance in feature space is used as similarity criteria. As an initial threshold, the mean angle difference or the mean Euclidean distance is applied. It is based on an image kernel of 3 by 3 pixels ( $P = 8$  and  $R = 1$ ) for every pixel in the image. The lower the threshold the more objects will be formed. A threshold close to 0 will segment every pixel as individual objects. A maximum threshold will segment the whole image as a single object. Thus, the threshold value determines the scale of segmentation.

After the initial growing phase new seeds are placed to form new objects. This process is continued until all image pixels are merged with an object. In the next phase, adjacent objects are merged according to the same similarity criterion. The spectral angle or Euclidean distance between mean spectra of objects is used to assess whether objects can be merged. This process is continued until a stable image segmentation is obtained.

In this approach, only spectral properties are used to form objects. Information on texture might provide useful information for identification of objects. In this chapter, an extension of the standard region growing algorithm is applied by using the multi-scale  $LBP_c^N$  and  $VAR_c^N$  texture measures. The purpose is to identify objects based on texture homogeneity. It is argued that basic land form elements can be described by a multi-scale texture measure and extracted by region growing based on this measure. Additionally, pixel similarity measures are used to depict uncertainty. To derive an uncertainty measure with values between 0.0 and 1.0, the similarity value is inverted and normalised based on the selected threshold. Thus, a pixel with a high uncertainty value is assigned to an object with low similarity, caused by a large angle or distance in feature space between the feature vectors of an object and an adjacent pixel. Transition zones between objects show high uncertainty values, as these zones are characterised by vagueness.

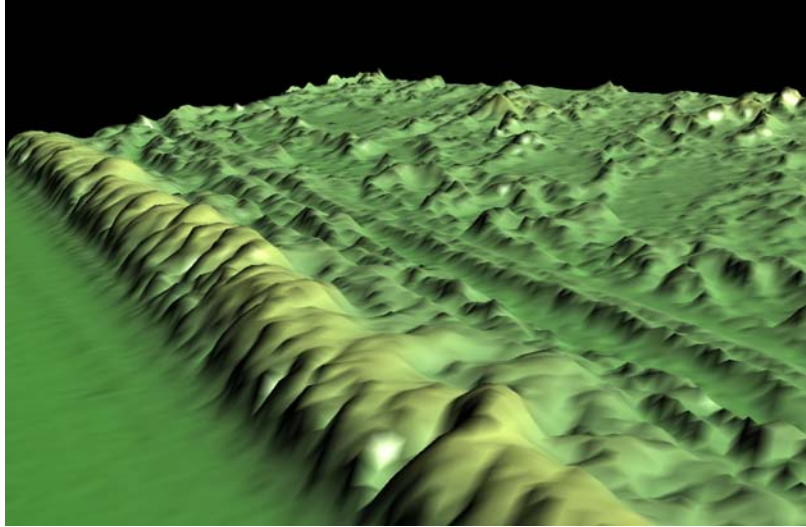


Figure 7.2: 3D view of LiDAR DSM of the study area. It clearly shows the beach, fore dune and other dune ridges in the dune fields

## 7.4 Multi-scale texture measures from a LiDAR DSM

In this study, the LiDAR surface model as described in chapter 5 was used to identify coastal land form objects. Figure 5.1(b) shows the LiDAR DSM of the study area. Figure 7.4 gives a 3D representation of the DSM to show the typical coastal land forms like dune ridges and troughs.

For every pixel in the LiDAR DSM, texture measures were calculated for three neighbourhood sets  $LBP_c^{8,1}$ ,  $LBP_c^{8,5}$  and  $LBP_c^{8,10}$  as well as  $VAR_c^{8,1}$ ,  $VAR_c^{8,5}$  and  $VAR_c^{8,10}$  ( $P = 8; R = 1, 5, 10$ ). The  $LBP_c$  values for the three circles were summed to calculate  $LBP_c^N$ . This value was then assigned to the centre pixel. Similarly for  $VAR_c$ , the variance of the pixels in all three sets was assigned to the centre pixel. The result of this operation is given in figure 7.3. Land forms are more pronounced in these texture images. The  $LBP_c^N$  7.3(g) and  $VAR_c^N$  7.3(h) images were combined with the original DSM to form a three-band image composite as input for the region growing algorithm (figure 7.4(a)).

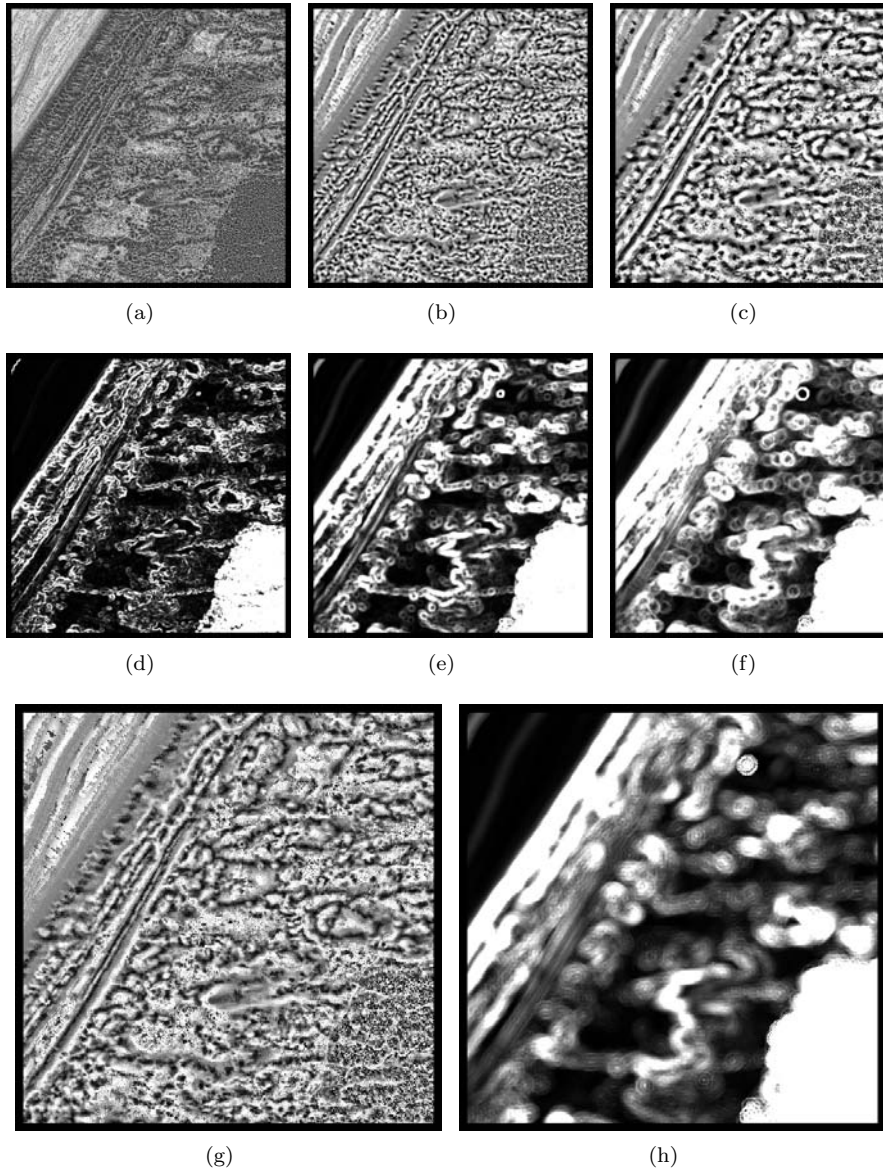


Figure 7.3:  $LBP_c$  and  $VAR_c$  texture values for the LiDAR DSM: (a)  $LBP_c^{8,1}$  image; (b)  $LBP_c^{8,5}$  image; (c)  $LBP_c^{8,10}$  image; (d)  $VAR_c^{8,1}$  image; (e)  $VAR_c^{8,5}$  image; (f)  $VAR_c^{8,10}$  image; (g) Total  $LBP_c^3$  image; (h) Total  $VAR_c^3$  image.

## 7.5 Texture-based region growing for identification of land form objects

For the identification of land form objects, a seeded region growing algorithm was applied to the texture composite image derived from the LiDAR DSM (figure 7.4(a)). As a similarity criterion, the angle in feature space between the mean vector of an object and the feature vector of an adjacent pixel was used. The threshold was 0.30 radians. Initially 6006 objects were formed. After merging neighbouring objects in four iterations, 1446 objects remained. The segmentation result is depicted as an object image; each object has been assigned an object number and objects are classified into colour classes (figure 7.4(b)). Object boundaries were extracted and overlaid with the original LiDAR DSM for object visualisation (figure 7.4(c)). Additionally, similarity measures for every pixel provided information about uncertainty, depicting pixels with high similarity values as a low uncertainty. Dark values in figure 7.4(d) depict pixels with high uncertainty.

Figure 7.4(b) clearly shows land form objects. The beach flat was segmented as one homogeneous object with low overall uncertainty values. Dune ridges were identified correctly, as these objects corresponded to observations in the field. The fore dune was segmented as one homogeneous object. The dune ridges southwest of the fore dune were depicted as long thin objects in the segmented image and several parabolic dune ridges could be observed. The lower parts of these dunes were segmented as separate objects, corresponding to blowout areas. The woodland area was different from the dune area as its variance in texture was very high, caused by the spiky signal of the laser return from the pine trees. The woodland area was identified as several homogeneous objects. Uncertainty values in figure 7.4(d) are high in boundary areas of dunes and dune troughs, depicting transition zones between these land form objects, as expected.

In figure 7.5 a detailed section of the fore dune area is shown. The steep slope of the fore dune was segmented as a separate land form object (figures 7.5(c) and 7.5(d)). The dune ridge itself was segmented as a wide object with several higher sub-ridges as separate objects in between, corresponding to observations in the field. High uncertainty values occurred in the boundary areas of objects (figure 7.5(e)), showing transition zones between the dune crest object, the dune slope object and the beach object. This was a meaningful result as land form objects are not crisp, they are vague in their definition, existence and spatial extent. Therefore, uncertainty values were expected to be high in transition zones between fuzzy land form objects.

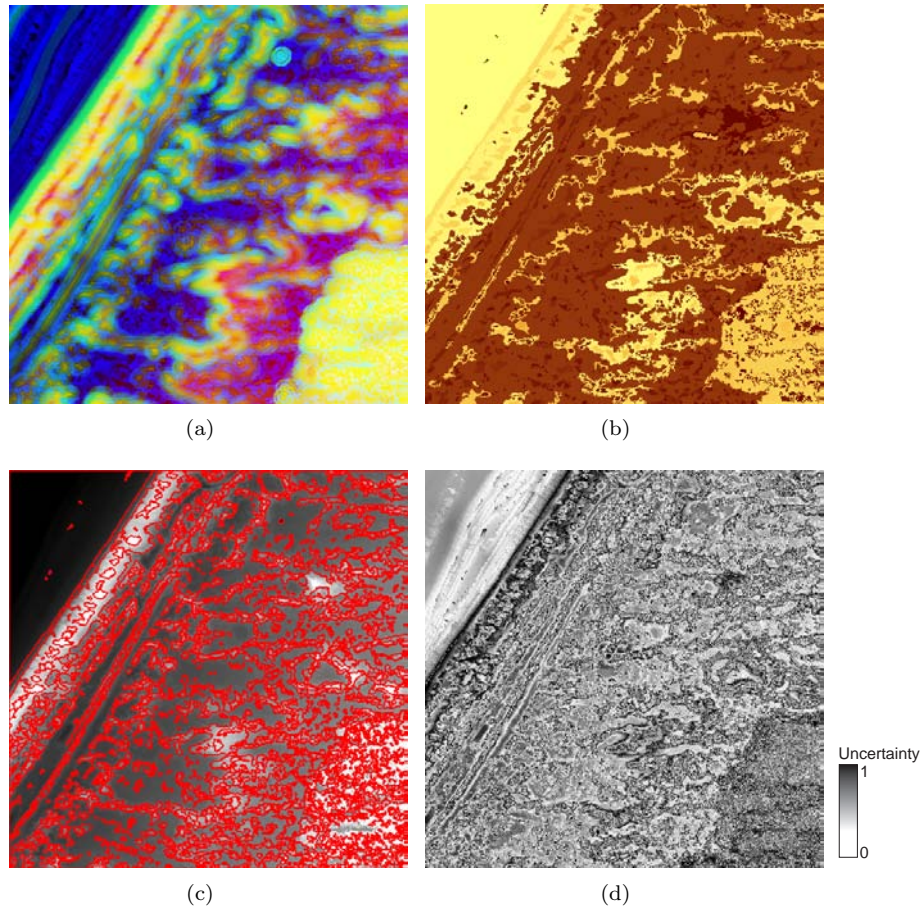


Figure 7.4: Region growing results: (a) Colour composite of combined elevation,  $LBP_c^3$  and  $VAR_c^3$  values used as input for region growing; (b) Objects as identified by region growing algorithm with numbered labels in order of identification; (c) Original elevation image with object contours; (d) Similarity values for each pixel depicting uncertainty. The darker the pixel, the higher the uncertainty.

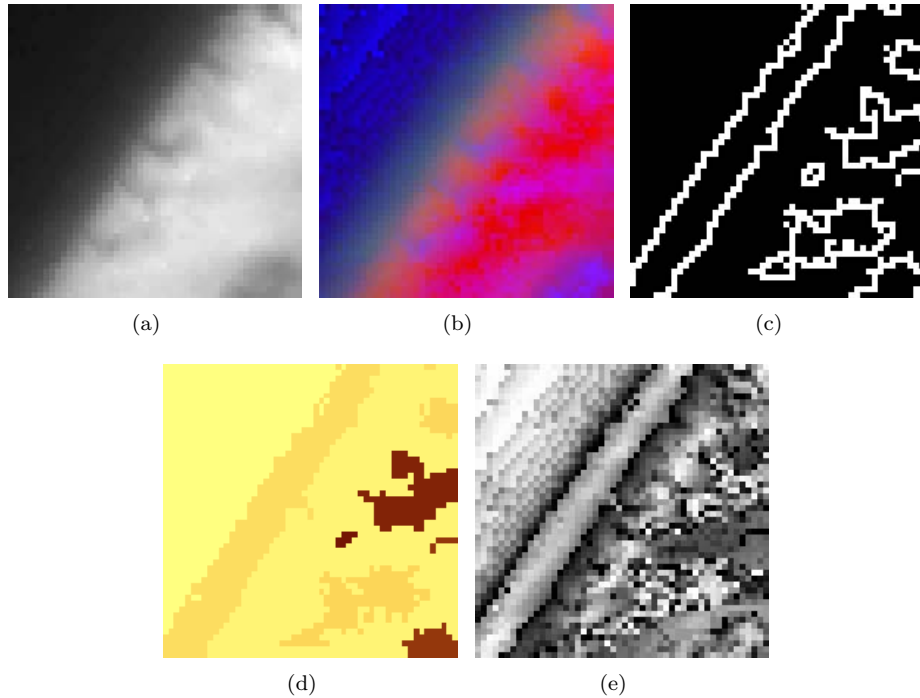


Figure 7.5: Detailed section of the fore dune: (a) LiDAR elevation of the fore dune; (b) Colour composite of multi-scale LBP, VAR and elevation; (c) Edges as defined by region growing; (d) Objects identified by segmentation; (e) Uncertainty for every pixel, boundary zones show high uncertainty values.

## 7.6 Discussion and conclusions

In this study, a region growing algorithm was implemented to derive land form objects from a LiDAR DSM based on multi-scale image texture. Image texture was modelled with the Local Binary Pattern operator (LBP) and local variance. The standard  $LBP_c$  and  $VAR_c$  texture measures were extended with a multi-scale neighbourhood set. Compared to a local texture measure, a multi-scale approach provided a better land form description. The combination of the multi-scale  $LBP_c^N$  and  $VAR_c^N$  measures and the original elevation data provided input for a region growing algorithm. Initial seed pixels were placed to form initial objects, based on minimum local variance. Merging of objects and adjacent pixels was based

on a similarity criterion of the angle between the mean vector of an object and the feature vector of an adjacent pixel. After all image pixels were assigned to an object, neighbouring objects were merged according to the same similarity criterion. This process continued until no more objects could be merged in the image. Since the procedure was unsupervised, the identified objects were assigned numeric labels in order of identification.

As an application, a LiDAR DSM of a coastal area in England was segmented into coastal land form objects. The texture-based region growing provided meaningful objects from the LiDAR DSM. Additionally, a pixel uncertainty value was based on a similarity measure, i.e. a large angle in feature space between an object mean vector and a neighbouring pixel feature vector was interpreted as a high uncertainty value. These uncertainty values provided valuable information about transition zones between fuzzy objects.

In this study, an unsupervised approach was taken towards object identification. The advantage is that it provides an objective and automated technique of land form mapping. The identified objects, however, do not have class labels. A subsequent step in land form analysis could be a classification stage using objects for an object-based classification. For example, information on elevation distribution, texture distribution, object shape, topology, and semantics could be used to classify objects into meaningful land form classes and label the objects accordingly.

Validation of land forms is a difficult task. In this study, the most up to date and most accurate elevation data available were used. Therefore, good reliable reference data could not be used for validation of the segmentation results. The changing nature of the coastal environment made validation even more complicated, since an accurate land form map of the same date was unavailable. Even if appropriate reference data would be available, validation itself is not straightforward. Object validation is often done based on boundaries (chapter 4). As shown in this chapter, coastal objects have a fuzzy nature, i.e. there are transition zones between objects. Therefore, boundary matching would be a difficult task as fuzzy objects only have an arbitrary boundary. Therefore, object validation was neither feasible nor meaningful. From field observations, however, it could be concluded that good segmentation results were obtained. The described texture-based region growing is not restricted to coastal land form mapping. It can easily be applied to other remote sensing images and other study areas.

7.6. Discussion and conclusions

---

## Part III

# Object uncertainty visualisation





## Chapter 8

# Visualisation of Thematic and Spatial Object Uncertainty \*

*We shall not cease from exploration and the end of all our exploring  
will be to arrive where we started . . . and know the place for the first time.*

T. S. Eliot

### 8.1 Introduction

In this chapter, the visualisation tool as described in part I is extended for visualisation of objects to show the relation between thematic uncertainty and spatial uncertainty. Uncertainty values derived for objects using either visual classification or segmentation provides information on the thematic content and spatial extent of objects. Static uncertainty images (figures 2.4(b) and 6.3(b)) give a limited and global overview of the distribution of uncertainty values.

---

\*This chapter is based on the following paper:

Lucieer, A. and Veen, L. E. (in prep.). Visualisation of object uncertainty in remotely sensed imagery by 3D interactive isosurfaces, *Information Visualization*. in prep.

---

Object uncertainty provides important information for the fitness for use of a remotely sensed image segmentation or classification. Uncertainty in the spatial extent of objects may indicate transition zones or indeterminate boundaries. Thematic uncertainty may provide information on vagueness due to object or class definition or overlap. Uncertainty can affect further data processing and eventually decision making. Effective communication can make users more aware of uncertainty in segmentation or classification. More specifically, exploration can provide valuable information on the relation between uncertainty in the spatial extent of objects and their thematic uncertainty.

In part I, spheres, ellipsoids, convex hulls and  $\alpha$ -shapes were used to visualise the shape of reference class clusters *prior* to a visual classification in a 3D feature space plot. Pixels derived from small reference areas in an image were used for a supervised classification. The same visualisation methods can be used to visualise reference areas used for supervised segmentation techniques as described in part II. Essentially, these visualisations can represent any cluster of pixels in 3D feature space. Therefore, these techniques are also suitable for visualising objects *after* classification or segmentation. They can help to explore uncertainty related to individual classes or objects. Interaction with a user-defined uncertainty threshold might improve insight into thematic uncertainty of objects, as their representation in 3D feature space might change for different uncertainty thresholds, effectively taking a subset from an object cluster by adding or removing pixels based on this threshold.

An initial step towards visualisation of an object in 3D feature space is a sphere, representing the mean and maximum standard deviation of an object. A more accurate object representation is an ellipsoid, taking into account different variances in different bands. Even more accurate representations of an object are convex hulls and  $\alpha$ -shapes. See chapter 3 figure 3.3 for a comparison of these shapes. Although  $\alpha$ -shapes are visually complex, their accurate representation is most suitable for detailed exploration of uncertainty, as the exact location and volume of class or object overlap can be visualised. Additionally, the exact shape of a pixel cluster may yield valuable information on irregularities and outliers. The algorithm to calculate an  $\alpha$ -shape from a pixel cluster, however, has high computational demands, making it difficult to visualise  $\alpha$ -shapes in real-time. Fast interaction and real-time visualisation are important for exploration of object uncertainty. If a user changes the uncertainty threshold, it should immediately be reflected in the object shape.  $\alpha$ -shapes and convex hulls have to be re-calculated for every change of the uncertainty threshold, making these shapes unsuitable for interactive visualisation. Similarly, for spheres and ellipsoids underlying statistics have to be recalculated for a changing threshold. To accurately visualise a chang-

ing object shape in real-time, an algorithm that takes advantage of the similarity between shapes is preferable. Isosurfaces (Bloomenthal and Wyvill, 1997) can approximate an  $\alpha$ -shape. They visualise objects in 3D feature space in real-time, enabling interaction.

This chapter aims to develop and implement visualisation methods for exploration of objects and their uncertainty, derived from visual classification or segmentation. Interaction with a user-defined uncertainty threshold is a focal point to explore the effect of changing uncertainty on the spatial extent of an object and its thematic uncertainty. A 3D feature space plot (section 2.4) is extended to visualise the shape or thematic content of objects. An image display (section 2.4) is extended to visualise the spatial extent of objects. It is hypothesised that the visual link between feature space and geographic space improves exploration of the relation between spatial and thematic uncertainty.

## 8.2 Isosurfaces

Pixel locations in feature space correspond to pixel values in an object. Pixels can be thresholded based on a user-defined uncertainty threshold, showing only pixels with an uncertainty value lower than the threshold. To visualise a cluster of pixels as a shape in feature space, each pixel is considered a potential source analogous to a planet in the universe. A source has a mass, and the potential  $p$  is calculated using the potential energy in a gravity field

$$p = -G \frac{m_1 m_2}{r} \quad (8.1)$$

where  $G$  is the gravitational acceleration ( $G = 9.8m/s^2$ ),  $m_1$  and  $m_2$  are masses and  $r$  is the distance between them. For a feature space plot, this is simplified to

$$p = \frac{m_1}{r^c} \quad (8.2)$$

where  $G = 1.0$ ,  $m_2 = 1.0$ , and  $p$  is the potential generated at a particular point in feature space  $(x, y, z)$ .  $m_1$  is the mass of a source determined by the distance to the closest neighbouring source. The mass is analogous to parameter  $\alpha$  for  $\alpha$ -shapes (section 3.3), as a higher mass pulls the surface closer to a source, possibly forming disjoint shapes. The constant  $c$  is used to determine the power of the potential function.

The potential at an arbitrary point in feature space is the sum over all sources of the potentials for that point. The potential is high in the vicinity of sources,

and low in areas without sources. The derivative of the potential, the gradient  $g$  at location  $(x, y, z)$ , is defined as:

$$g = \nabla p \tag{8.3}$$

Visualising the shape of a cluster of pixels now becomes a matter of rendering an isosurface corresponding to a surface with equal potential.

The most common algorithm for rendering isosurfaces is the marching cubes algorithm (Lorensen and Cline, 1987), subdividing space into cubes. For each cube it determines the intersection between the cube and the isosurface, generating one or more polygons that describe the isosurface within the cube. Generated polygons for all cubes are then connected into a mesh using a standard triangulation. Despite its name, the marching cubes method is not very dynamic, as for a change the entire mesh has to be regenerated. The position and number of sources change for different uncertainty thresholds. Exploration of object uncertainty relies on real-time interaction with various uncertainty thresholds. Therefore, an algorithm that takes advantage of the similarity between shapes would be preferable. Instead of a mesh, point rendering (Levoy and Whitted, 1985; Rusinkiewicz and Levoy, 2000) is considered to visualise an isosurface. This algorithm has as its main advantage that the geometry needs not to be generated and re-calculated. Therefore, it is faster and ultimately more interactivity is possible. Recently, QSplats were proposed to make the visualisation more appealing (Rusinkiewicz and Levoy, 2000). Instead of rendering a large number of points (in the order of  $10^6$  or more), each point is displayed as a small circle or pentagon visualising a shape as a continuous surface. To visualise an image object in 3D feature space, an isosurface is created based on object pixels using algorithm 8.1 given below.

```
Set uncertainty threshold;
Threshold object pixels and collect pixel values;
Set position of sources based on pixel values;
Randomly distribute pentagons in 3D feature space;
while All faces are not on isosurface do
    | Move pentagons towards isosurface based on potential and gradient;
    | Move pentagons away from neighbouring pentagons;
end
```

Algorithm 8.1: Algorithm for visualisation of an object isosurface.

To visualise the isosurface, pentagons are moved towards the isosurface into the direction of the potential gradient. Pentagons are regularly distributed over

the surface based on a repulsion force. This force depends on the distance between neighbouring pentagons and it works perpendicular to the direction of displacement of a pentagon towards the isosurface. Pentagons close together are pushed away in the opposite direction until a stable and regular distribution of pentagons over the isosurface is obtained. Each time the uncertainty threshold changes and sources appear or disappear, the algorithm is re-run to move all pentagons to the new isosurface. Algorithm 8.2 describes the procedure for moving pentagons towards an isosurface.

```

c = position of pentagon;
p = potential at position c;
i = 1.0 = isovalue (distance between source and isosurface);
g = gradient at position c;
g' = normalised gradient;
d = difference;
δ = magnitude of displacement towards isosurface;
x = X-coordinate at position c;
m = sum of forces at position c;
C1 = speed factor with which pentagons move towards isosurface;
C2 = speed factor with which pentagons move away from each other;
for c in all pentagons do
  | d = i - p;
  | δ = d/|g|;
  | for x in all pentagons do
  | | m = m + (c - x)/|(c - x)|2;
  | end
  | c = c + C1 * disp * g' + C2 * (m - g'm * g');
end

```

Algorithm 8.2: Algorithm for moving pentagons towards isosurface.

Initially, all object pixels are considered as a source. Pixel grouping is considered to reduce the number of sources, increasing the speed of an iteration. This method groups points that are close to each other in feature space into a single potential source by partitioning feature space into a regular grid of cubes. Pixels within a single cube are aggregated into a single source and its location is the mean of the locations of its pixels. Source uncertainty is the mean uncertainty of its pixels.

This algorithm is a hill-climbing algorithm, which may suffer from occurrence

of local maxima. This may happen if an object has a high variance of pixel values. In that case, sources can be spread across feature space, forming multiple unconnected isosurfaces for one object. For a single object with disconnected isosurfaces, pentagons may only move towards the nearest isosurface, making a distant isosurface invisible. A related problem occurs when a new source appears in a location at a large distance from any existing source. This situation may happen if additional sources are added for a growing object. Since all pentagons are close to an existing isosurface, pentagons will not move to the new source, making that part of the isosurface invisible. Firstly, a solution to this problem can be found by a correct initialisation of pentagons. During initialisation, pentagons should be placed near the sources, inside the isosurface, instead of at random locations. Secondly, pentagons should be dynamically added or removed near new sources as sources are added or removed. Thirdly, using only nearby sources instead of all sources to position pentagons can speed up the iteration process. Similarly, for a regular distribution of pentagons over an isosurface only neighbouring pentagons need to be considered.

Rendering of isosurfaces can be further enhanced by bending of pentagons. Initially, pentagons are flat surfaces, centered on the isosurface and oriented according to the gradient. The isosurface, however, is most often curved. A more accurate representation can be obtained if the pentagons can be bent by moving their outer points onto the isosurface. Fewer pentagons can then be used to get the same visual quality, thus speeding up the process.

## 8.3 Comparison of object representations

Figure 8.2 shows a comparison of representations for an image object containing 24,000 pixels. Computational speed is fastest for the sphere and the ellipsoid for this object. However, if the uncertainty threshold changes, all pixels in the object have to be revisited to recompute its statistics. For an isosurface (figure 8.2(e)) only the parts that are added or removed have to be computed. This speeds up the rendering process and it makes isosurfaces most suitable for fast interaction. The most accurate representation is given in figure 8.2(d) showing an  $\alpha$ -shape of the same object. This figure also shows that an isosurface provides a good approximation (figure 8.2(e)). Computation and rendering of the  $\alpha$ -shape on a Pentium III processor at 800 MHz took 1 minute and 19 seconds, making interaction practically impossible. The isosurface was computed and rendered within 1.2 seconds. Figure 8.1 shows a comparison of the computational speed, when interacting with an

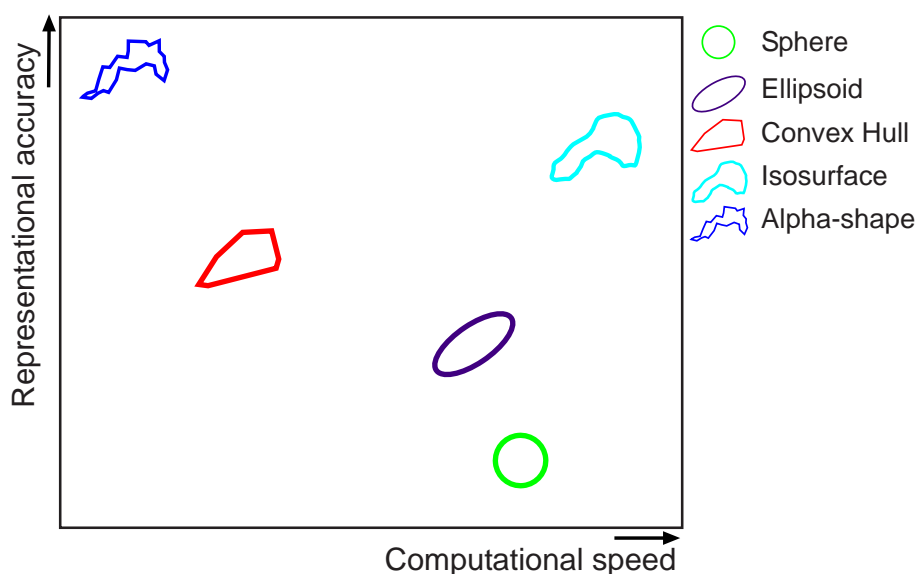


Figure 8.1: Computational speed for generation of each visualisation.

uncertainty threshold, versus the representation accuracy of the different shapes. Isosurfaces provide a trade off between speed and accuracy, and they are most suitable when fast interaction with object uncertainty is required.

## 8.4 Visual link between thematic uncertainty and spatial uncertainty

A classification or segmentation result is usually shown as a crisp map. Underlying uncertainty of object or class pixels can be stored and visualised in a separate map. Use of an uncertainty threshold may be helpful to explore parts of objects or classes with an uncertainty value lower than the threshold. By interacting with this uncertainty threshold, a user can explore the range in spatial extent and object shape. For example, all pixels belonging to an object with an uncertainty value between 0.0 and 0.3 may show the core area of an object that is identified with low uncertainty values. It shows the influence of uncertainty on the spatial extent

#### 8.4. Visual link between thematic uncertainty and spatial uncertainty

---

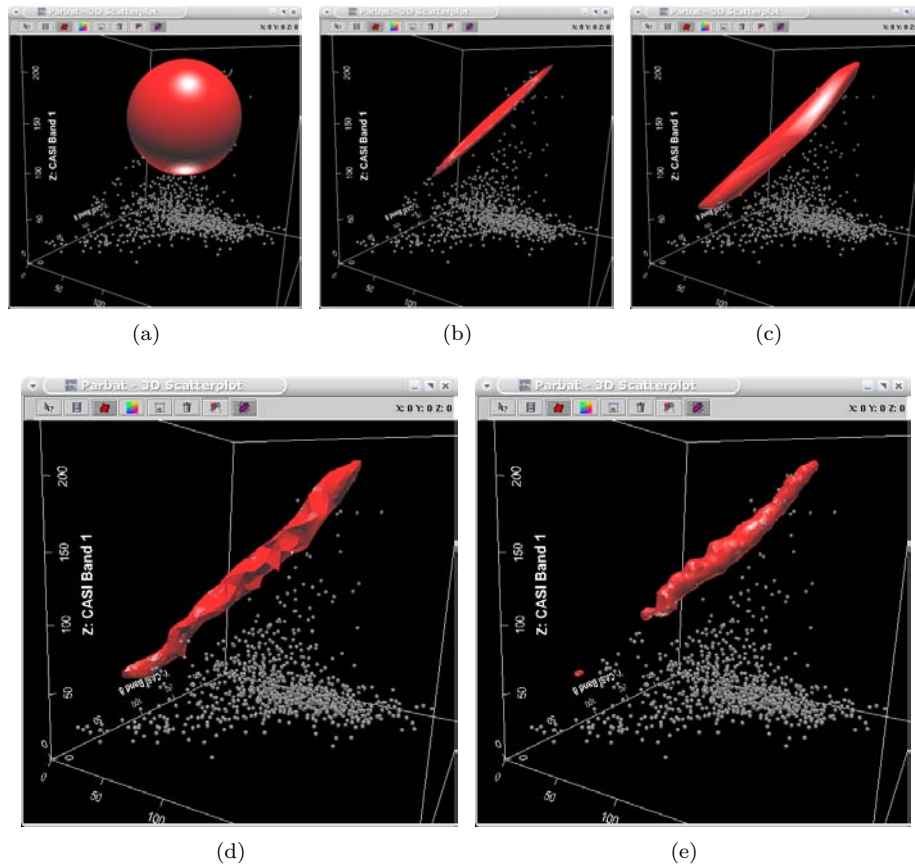


Figure 8.2: Comparison of shapes for object visualisation: (a) object sphere; (b) object ellipsoid; (c) object convex hull; (d) object  $\alpha$ -shape; (e) object isosurface.

of an object. The extent of some objects will change considerably, especially for objects with large transition zones, whereas for other objects it will change only slightly. Similarly, the shape of objects can be visualised in feature space using isosurfaces. By applying the same uncertainty threshold, the shape of the object in feature space will change. The amount of change of the object's shape in 3D feature space provides information about thematic uncertainty. Linking thematic and geographic visualisations, in the form of a 3D feature space plot and an image display, provides a powerful tool for analysis of object uncertainty. This tool is illustrated with two case studies, described earlier in part I and part II.

## 8.5 Case study: classification

The first case study concerns visualisation of uncertainty related to a visual fuzzy classification. In chapter 2, three bands of a Landsat 7 ETM+ image of the ‘La Peyne’ catchment in southern France (figure 8.3(a)) were used for classification. Figure 8.3(b) shows the classification after assigning class labels based on maximum membership values. Figure 8.3(c) and figure 8.3(d) give membership images for land cover class agriculture and class urban respectively. Figure 8.4 shows four isosurfaces for class agriculture using uncertainty thresholds corresponding to the following membership ranges, respectively 0.75–1.0 (figure 8.4(a)), 0.50–1.0 (figure 8.4(b)), 0.25–1.0 (figure 8.4(c)), and 0.05–1.0 (figure 8.4(d)).

Figure 8.5 shows the image displays with the spatial extent of class agriculture corresponding to the four uncertainty thresholds. Both isosurface and spatial extent increase with increasing uncertainty thresholds, but little change occurred between thresholds 0.75 and 0.95 (figure 8.4(c) and 8.4(d)). The spatial extent, however, increased considerably for this change in uncertainty (figure 8.5(c) and 8.5(d)). This exploration showed that many image pixels fall between uncertainty thresholds 0.75 and 0.95, depicted by a significant change in spatial extent. DN-values of these pixels, however, fall within the same location in feature space, showing no changes in the shape or size of the isosurface.

Next, classes agriculture and urban are visualised simultaneously to increase interaction and improve exploration of class overlap. Figure 8.6 shows isosurfaces and spatial extents of these classes, based on an uncertainty threshold of 0.50, corresponding to membership values between 0.50 and 1.0. Figure 8.6(a) shows that the two isosurfaces of these classes overlap. Small spatial overlap zones can be observed in figure 8.6(b), depicted in white. This visualisation method can help to explore transition zones and class overlap.

## 8.5. Case study: classification

---

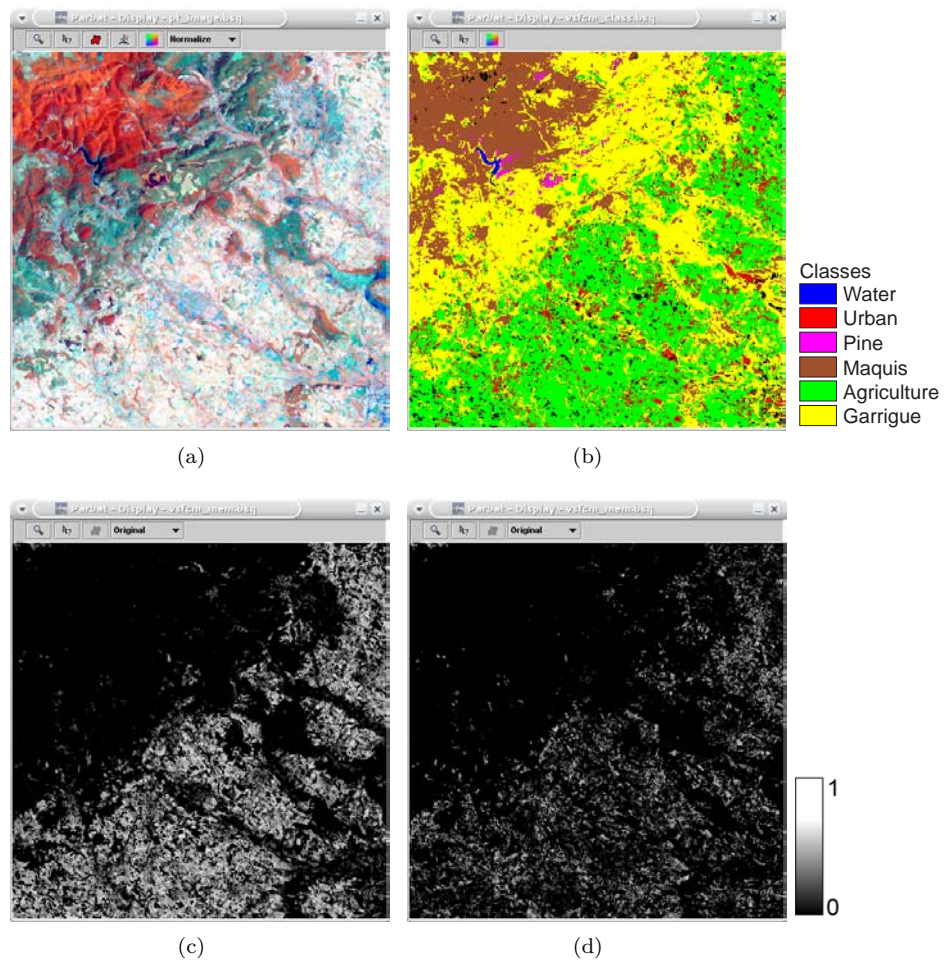


Figure 8.3: Visual fuzzy classification of Landsat image of the Peyne catchment, France: (a) Colour composite of bands 4,5 and 3 of a Landsat 7 ETM+ image; (b) Visual fuzzy classification result with land cover classes; (c) Image with membership values for class Agriculture; (d) Image with membership values for class Urban.

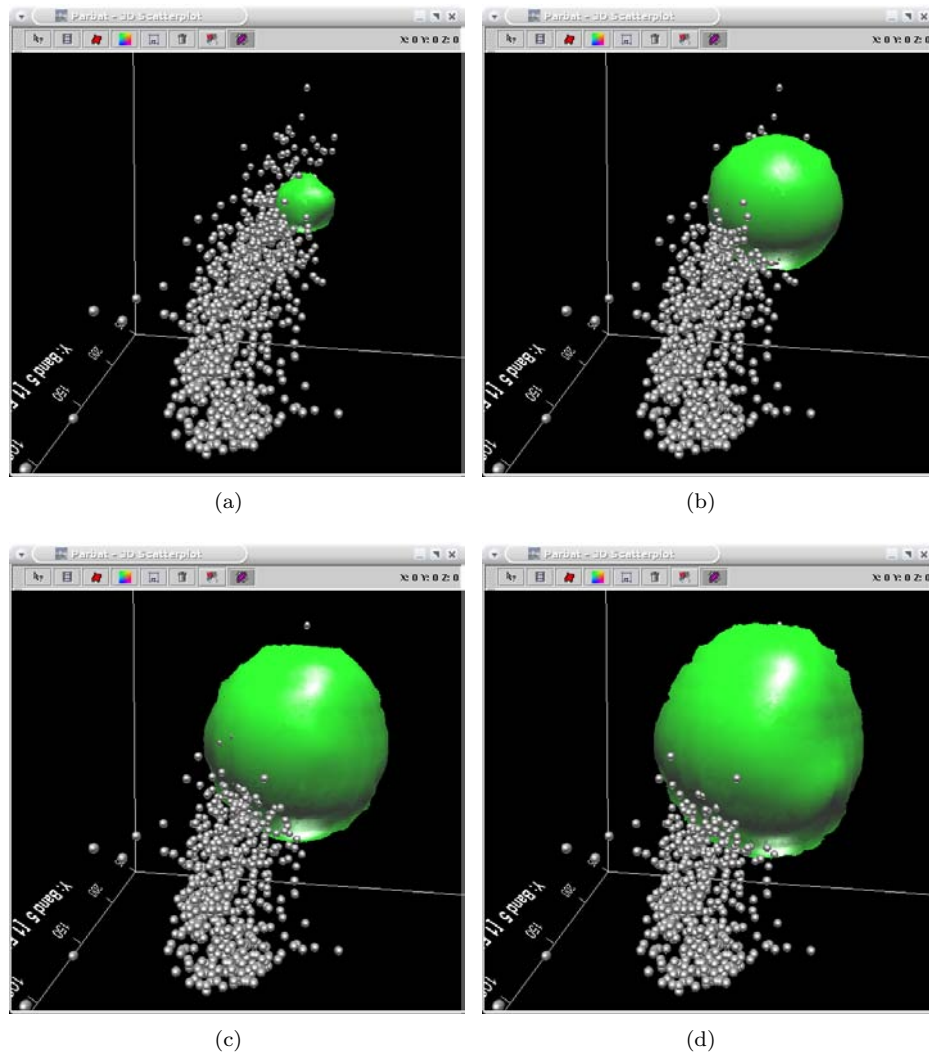


Figure 8.4: Isosurface for class Agriculture for different uncertainty thresholds: (a) Uncertainty range 0–0.25; (b) Uncertainty range 0–0.50; (c) Uncertainty range 0–0.75; (d) Uncertainty range 0–0.95.

## 8.5. Case study: classification

---

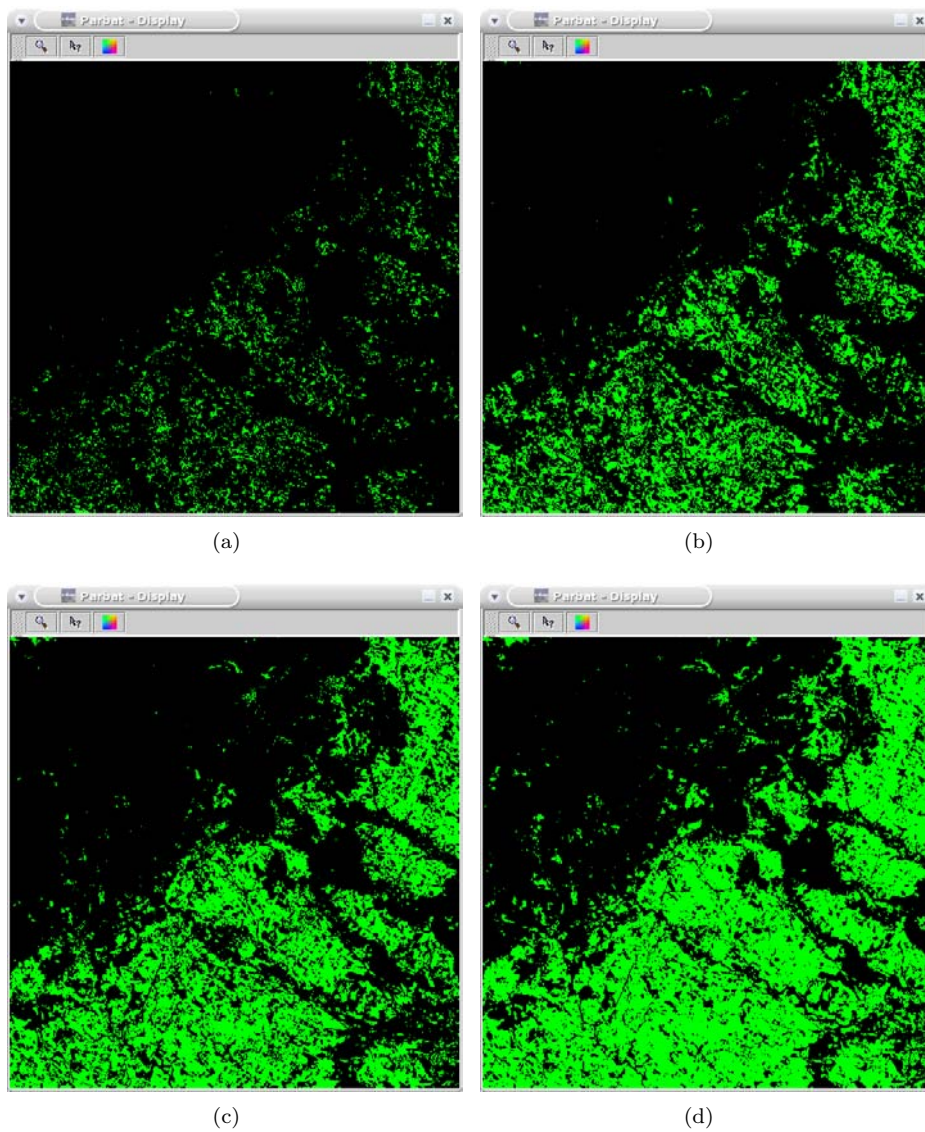
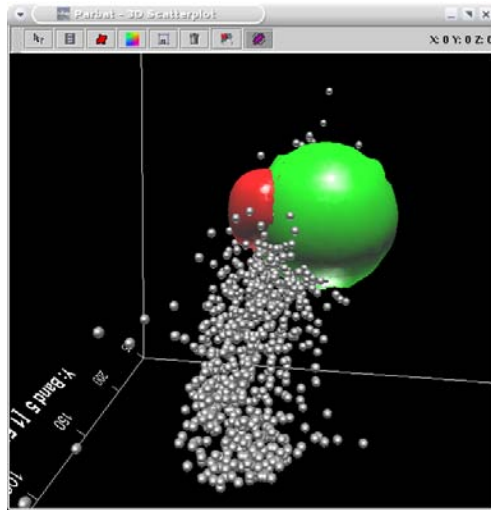
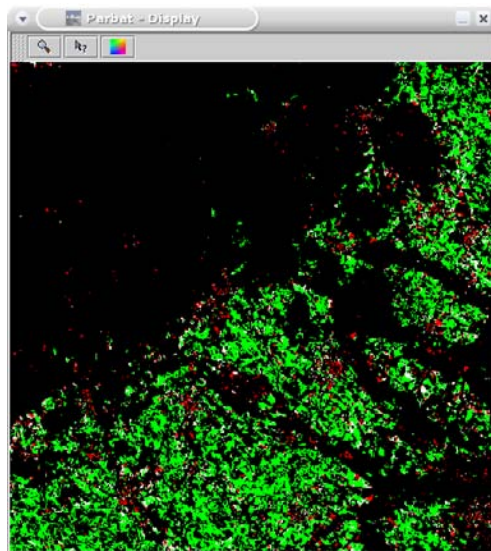


Figure 8.5: Spatial extent of class Agriculture for different uncertainty thresholds: (a) Uncertainty range 0–0.25; (b) Uncertainty range 0–0.50; (c) Uncertainty range 0–0.75; (d) Uncertainty range 0–0.95.



(a)



(b)

Figure 8.6: Isosurfaces and spatial extent for classes Agriculture and Urban, showing overlap: (a) Isosurfaces based on uncertainty range 0–0.50; (b) Spatial extent for this isosurface configuration, showing small areas of overlap in white.

## 8.6 Case study: segmentation

The second case study involves visualisation of uncertainty related to objects. Two objects were selected from a segmentation result presented in chapter 6, using a colour composite of band 12, 8 and 1 of a CASI image of the Ainsdale Sands in the UK (figure 8.7(a)). The result of a multivariate texture-based segmentation of the CASI image is given in figure 8.7(b) (section 6.3). The first object is a woodland object located in the southeast part of the image. Uncertainty values of its building blocks are shown in figure 8.7(c). The second object is a marram grass object located on the fore dune, visible as a straight diagonal object from the east to the north side of the image.

Isosurfaces for the woodland object are shown in figure 8.8. Four uncertainty thresholds were chosen, corresponding to the following uncertainty ranges: 0.0–0.25 (figure 8.8(a)), 0.0–0.50 (figure 8.8(b)), 0.0–0.75 (figure 8.8(c)), and 0.0–0.95 (figure 8.8(d)). The corresponding object spatial extent displays are shown in figure 8.9. For low uncertainty values (0.0–0.25) the ‘core’ area of the woodland object emerged, showing that only a small amount of object building blocks contained low uncertainty values. In the 3D plot, the woodland isosurface is shown as a number of small disjoint shapes. For an increasing uncertainty threshold, the isosurface formed a single large shape containing several small disjoint shapes. The size of the isosurface showed that variance of pixel values in this object was high. At the highest uncertainty threshold (0.0–0.95) small object blocks were added to the spatial extent of the forest object. These object building blocks corresponded to transition areas where willow trees occurred, as opposed to planted pine trees in the core area. At this uncertainty level, the woodland isosurface covered a large part of feature space, containing a large range of pixel values.

Figure 8.10 shows isosurfaces for the fore dune object. Four uncertainty thresholds were chosen, corresponding to the following uncertainty ranges: 0.0–0.50 (figure 8.10(a)), 0.0–0.65 (figure 8.10(b)), 0.0–0.80 (figure 8.10(c)), and 0.0–0.95 (figure 8.10(d)). The initial threshold was higher than in the previous examples, the reason for this being that no object building blocks contained uncertainty values lower than 0.25. Figure 8.10(a) and 8.11(a) show that only a small core area of the fore dune was selected for a low uncertainty threshold. The isosurface consisted of two disjoint sources. For an increasing threshold the spatial extent of the fore dune area increased considerably. The isosurface was formed by one large shape with some smaller disjoint shapes (figure 8.10(c) and 8.11(c)). At the largest uncertainty threshold, transition zones to the beach area were added to the spatial extent of the object. Additionally, the size of the isosurface increased considerably,

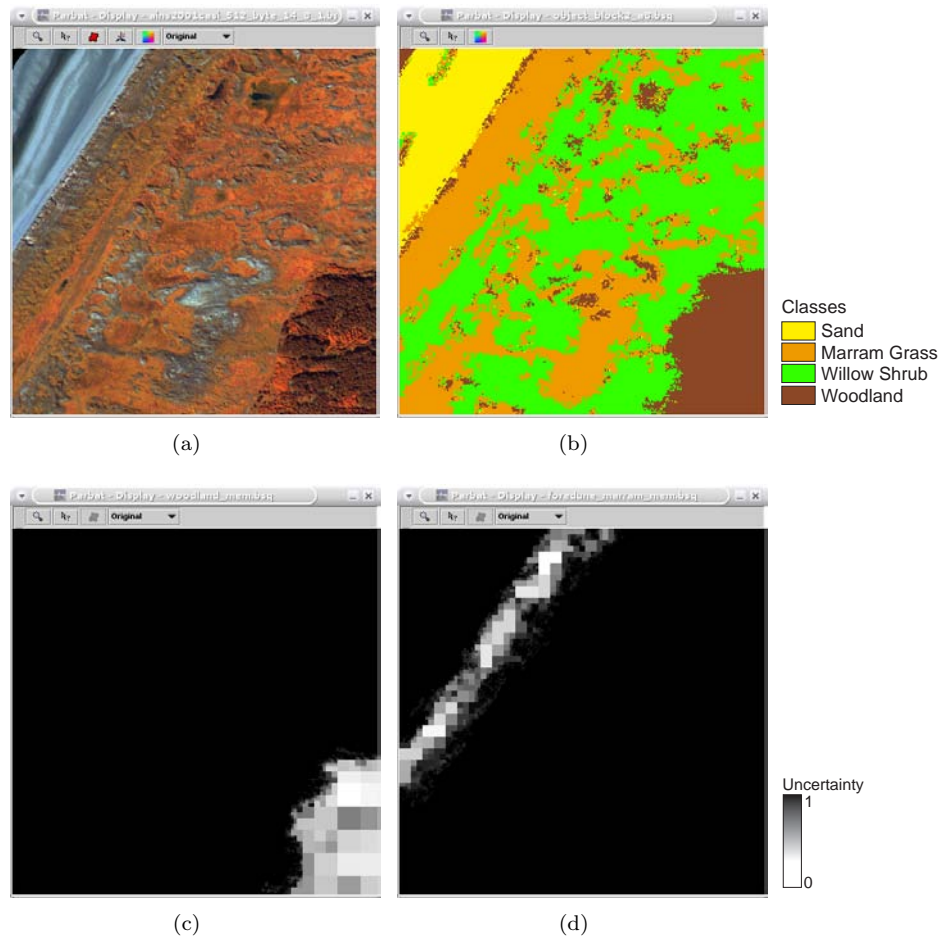


Figure 8.7: Object uncertainty for CASI land cover segmentation: (a) Colour composite of band 12, 8 and 1 of a CASI image of the Ainsdale Sands, UK; (b) Texture-based segmentation result showing land cover objects; (c) Uncertainty values for building blocks of woodland object; (d) Uncertainty values for building blocks of marram grass fore dune object.

again covering a large part of feature space.

## 8.6. Case study: segmentation

---

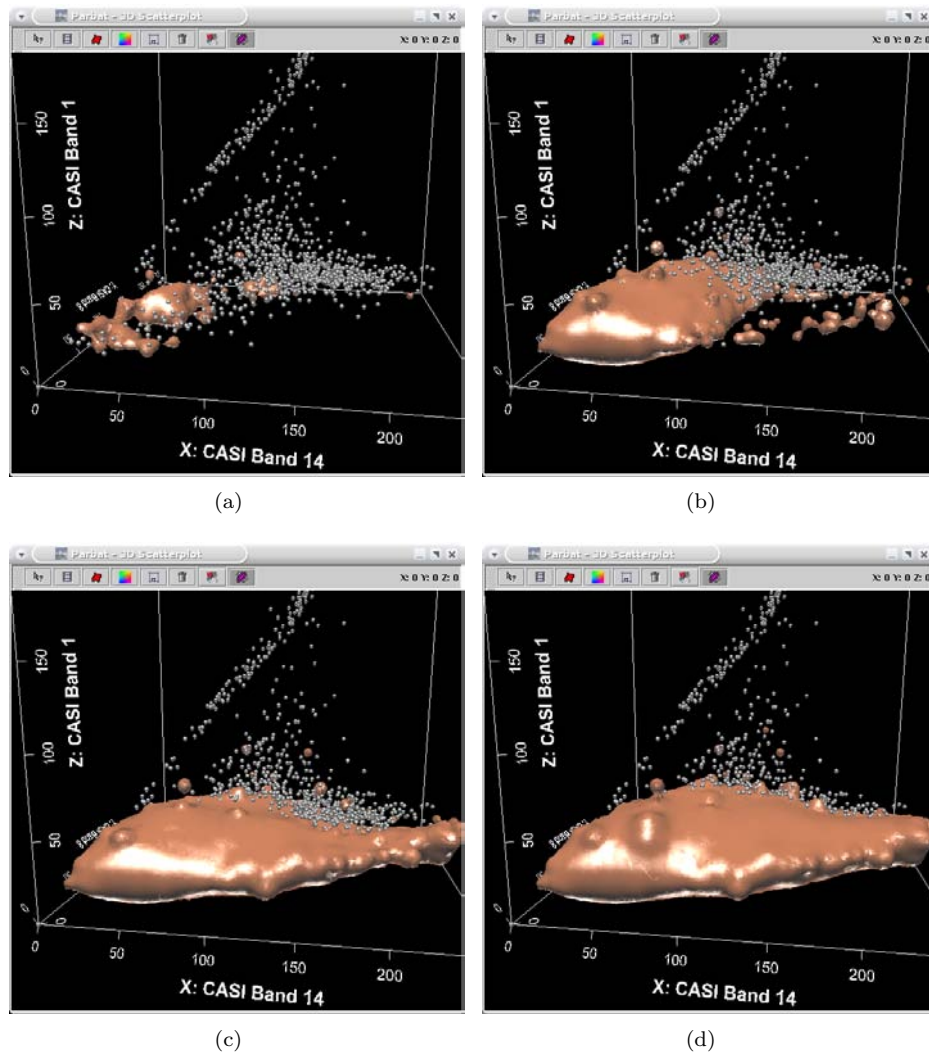


Figure 8.8: Isosurface for Woodland object for different uncertainty thresholds: (a) Uncertainty range 0–0.25; (b) Uncertainty range 0–0.50; (c) Uncertainty range 0–0.75; (d) Uncertainty range 0–0.95.

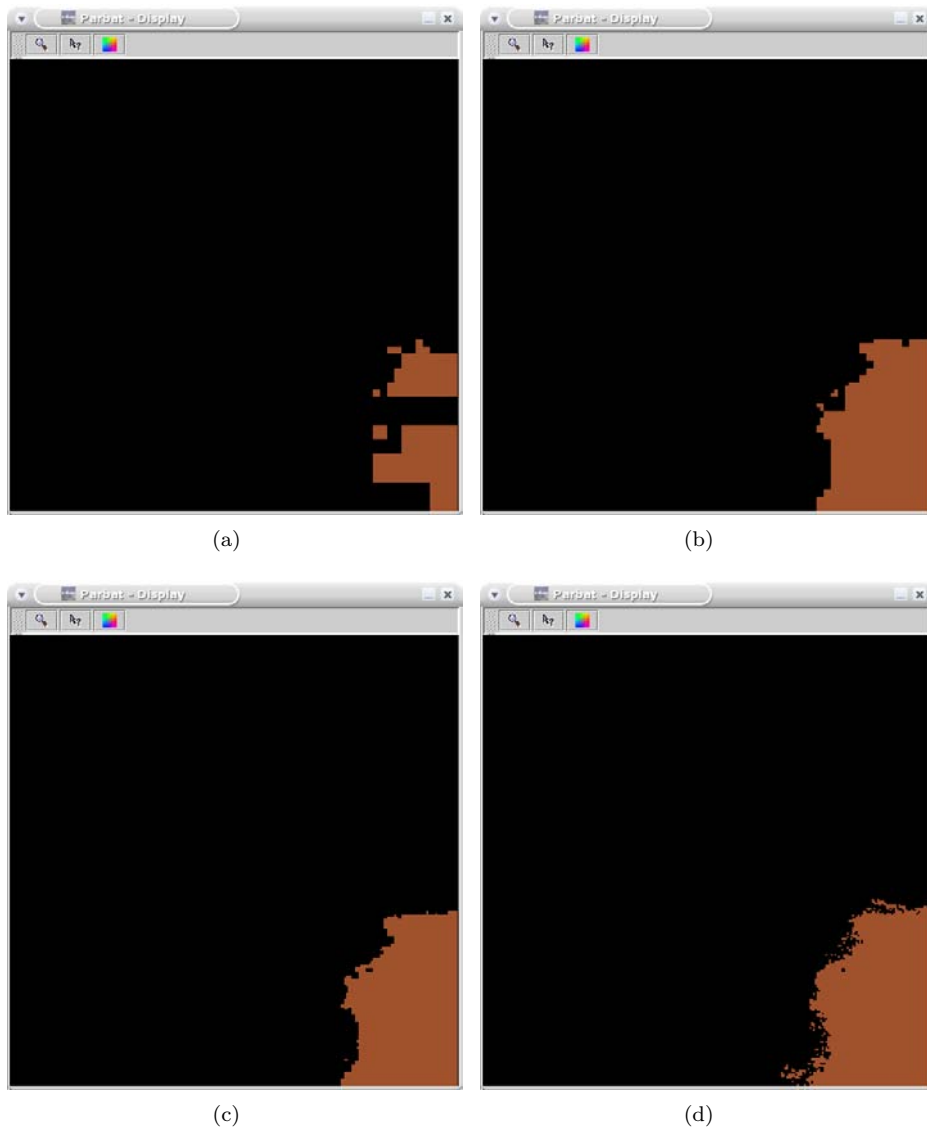


Figure 8.9: Spatial extent of Woodland object for different uncertainty thresholds: (a) Uncertainty range 0–0.25; (b) Uncertainty range 0–0.50; (c) Uncertainty range 0–0.75; (d) Uncertainty range 0–0.95.

8.6. Case study: segmentation

---

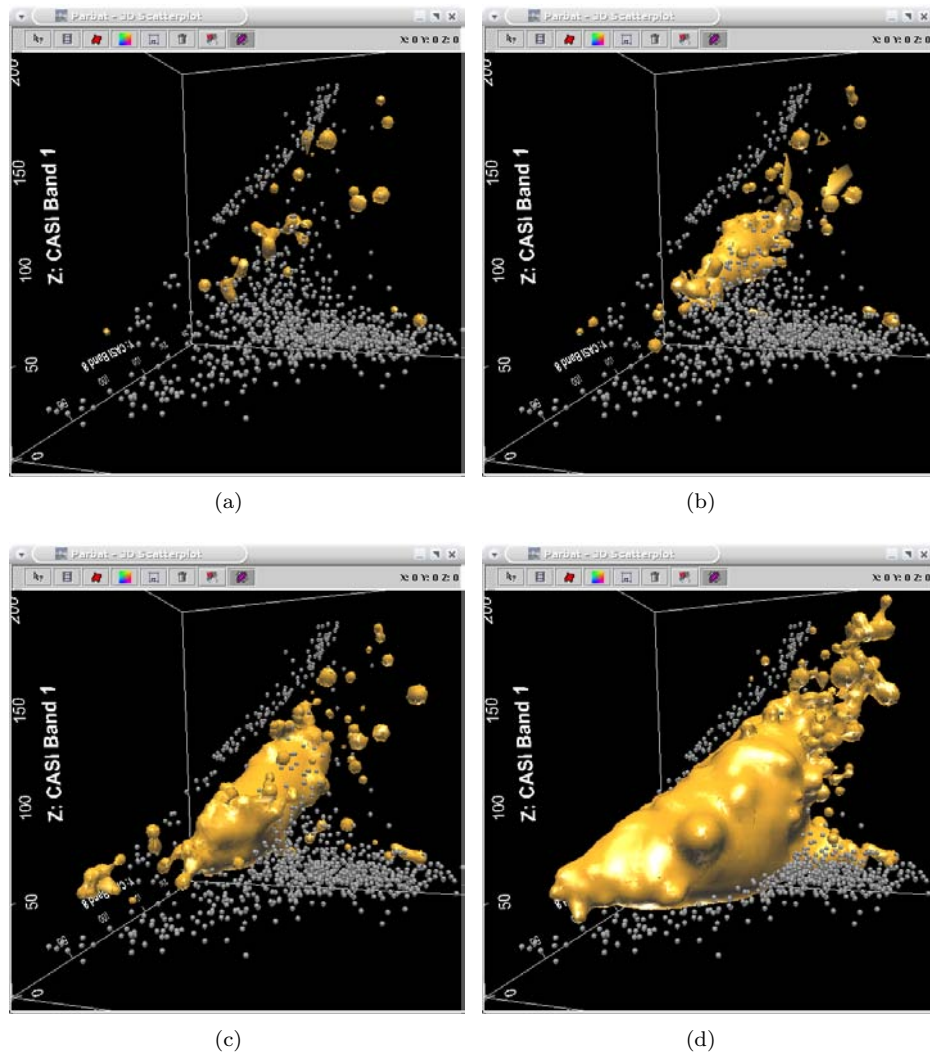


Figure 8.10: Isosurface for Fore dune object for different uncertainty thresholds: (a) Uncertainty range 0–0.50; (b) Uncertainty range 0–0.65; (c) Uncertainty range 0–0.80; (d) Uncertainty range 0–0.95.

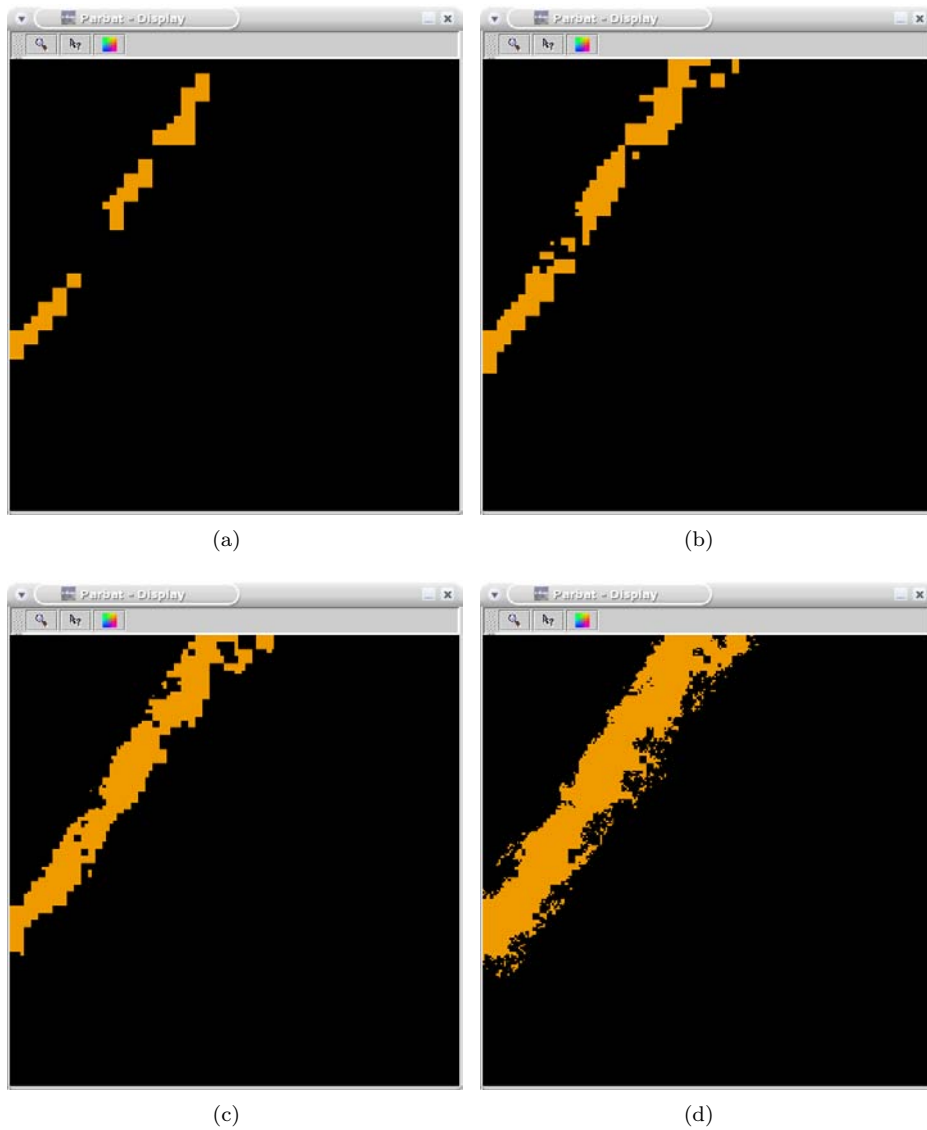


Figure 8.11: Spatial extent of the Fore dune object for different uncertainty thresholds: (a) Uncertainty range 0–0.50; (b) Uncertainty range 0–0.65; (c) Uncertainty range 0–0.80; (d) Uncertainty range 0–0.95.

## 8.7 Discussion

In chapters 2, 3, and this chapter, several techniques were discussed to visualise a cluster of pixels in a 3D feature space. The choice for a specific visualisation depends on the user task. If accuracy is most important,  $\alpha$ -shapes represent a pixel cluster most accurately. However, as computational demands are high, isosurfaces are more suitable for exploration purposes, facilitating real-time visualisation and interactivity.

Isosurfaces for visualisation of objects in 3D feature space are an alternative to  $\alpha$ -shapes. A possible improvement to the tool described in this chapter might be to use  $\alpha$ -shapes when no fast interaction is required. For example, an object could be visualised as an  $\alpha$ -shape for an initial uncertainty threshold. As soon as a user changes the uncertainty threshold, an object is visualised as an isosurface giving an approximation of the shape. A user should be able to switch between  $\alpha$ -shapes and isosurfaces, where  $\alpha$ -shapes are used for a more accurate representation and isosurfaces are used for real-time rendering and interaction.

Figure 8.12 gives an overview of the shapes and their suitability with respect to accuracy. For visualisation of reference class clusters prior to classification or segmentation,  $\alpha$ -shapes and isosurfaces provide the most accurate representation. Additionally, for this type of visualisation the structure of pixels does not change during visualisation, therefore, fast interaction is not required. For a visual classification spheres and ellipsoids are more suitable. These shapes depict the underlying statistics of a point cloud, used by a classifier. In chapter 2 spheres were used to visualise (and interact with) membership functions. In addition,  $\alpha$ -shape were used for a fuzzy classification in chapter 3. Since isosurfaces lack a statistical description of the underlying data, they are unsuitable for a visual classification. For visualisation of object uncertainty, as described in this chapter, isosurfaces and  $\alpha$ -shapes are most accurate.

In addition to accuracy and speed issues, usability is an important factor. For some users, the visual complexity of alpha-shapes, isosurfaces and convex hulls might be too high. Spheres or ellipsoids might then provide a more comprehensible representation. A focus group user test should be conducted to provide a qualitative description of the usability of the visualisation methods described in this chapter.

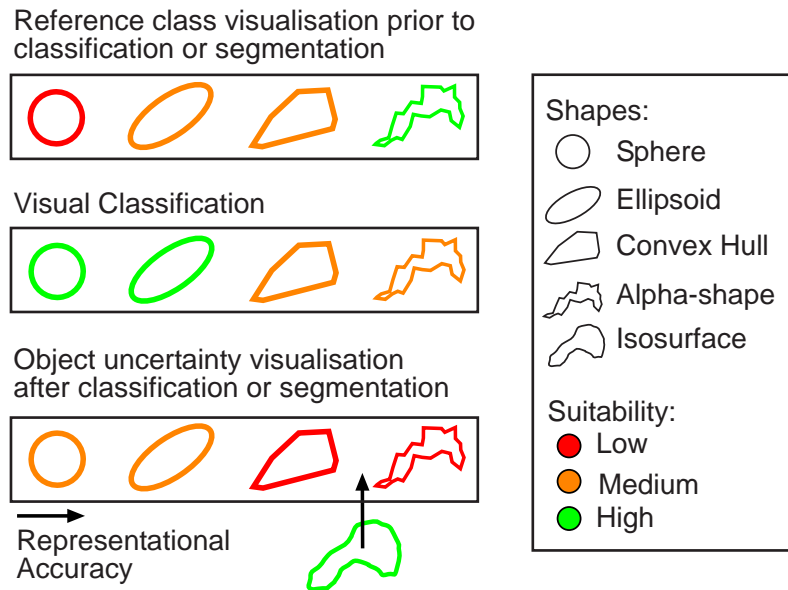


Figure 8.12: Overview of shapes and their suitability for specific user tasks.

## 8.8 Conclusions

In this chapter, new visualisation methods were developed for exploration of uncertainty related to image objects. A 3D plot showing feature space was dynamically linked to an image display showing geographic space. Spheres, ellipsoids, convex hulls, isosurfaces, and  $\alpha$ -shapes were compared for visualisation of objects in a 3D feature space plot. These objects were derived by visual classification or segmentation.  $\alpha$ -shapes provide the most accurate object representation, however, computational demands were very high, making them unsuitable for fast interactions. Alternatively, an isosurface is a good approximation of an  $\alpha$ -shape, facilitating interaction. Isosurfaces enable real-time rendering of objects in a 3D feature space plot. Interaction with an uncertainty threshold showed the change of an isosurface for a changing threshold, providing an indication for thematic object uncertainty.

The spatial extent of an object was visualised in an image display. For a

changing uncertainty threshold, the spatial extent of a selected object changes accordingly. Visual interaction with an uncertainty threshold and a dynamic link between feature space and geographic space is a powerful tool for exploration of the relation between thematic uncertainty and spatial uncertainty related to image objects.

The first case study concerned visualisation of uncertainty for a visual fuzzy classifier. Four uncertainty thresholds were applied to show the difference in spatial extent for the agriculture class. Thematic uncertainty was visualised using isosurfaces. Additionally, the urban class was visualised simultaneously to explore class overlap.

The second case study involved uncertainty visualisation of objects derived by multivariate texture-based segmentation from a CASI image of the Ainsdale Sand, UK. A woodland object was selected as a first example for visualisation of object uncertainty. The visualisation tool was valuable for exploring both thematic uncertainty and spatial extent of this object for different uncertainty thresholds. As a second object fore dune, covered with marram grass, was selected. Again, the visualisation tool provided valuable insights into object uncertainty. The effectiveness of the proposed visualisation tool, for different users, should be assessed in future research.

## Chapter 9

# Conclusions

*We do not live to eat and make money.  
We eat and make money to be able to enjoy life.*

George Leigh Mallory (1924)

In this study, visualisation techniques have been proposed for interaction with a fuzzy image classification and for exploration of thematic uncertainty. A tool has been developed to illustrate these visualisation techniques. It improves insight into fuzzy classification of land cover classes from multi-spectral remotely sensed imagery. Texture-based segmentation algorithms have been developed and applied to identify land cover objects and land form objects from fine spatial resolution imagery and to quantify their thematic uncertainty and spatial uncertainty. The visualisation tool has been extended to explore the relation of uncertainty in the spatial extent of objects and their thematic uncertainty.

### 9.1 Visualisation

- Visualisation of reference class clusters in 3D feature space provides new ways to explore locations of class clusters and class overlap. It yields valuable information about classes prior to classification. Visual information on class overlap provides an indication of thematic uncertainty for pixels in overlap zones. Dynamic linking of a 3D feature space plot and an image display
-

provides a suitable technique for exploration of relations between geographic space and feature space (chapter 2 and 3).

- A new visualisation tool facilitates visual interaction with the parameters of a supervised fuzzy classification algorithm. 3D spheres depict fuzzy membership functions in feature space, enabling a user to interact with a supervised fuzzy classification algorithm and improving insight into the effects of class overlap and changing membership functions. The visual fuzzy classifier is tested on a Landsat 7 ETM+ image of an area in southern France. Validation shows that this classifier is superior to standard fuzzy classification algorithms (chapter 2).
- Spheres and ellipsoids only approximate the shape of class clusters.  $\alpha$ -shapes effectively visualise the ‘real’ shape of class clusters in a 3D feature space plot, proving helpful in interpretation and exploration of class location, shape and overlap in a 3D feature space plot. Reference classes, derived from a Landsat 7 ETM+ image of the study area in France, are used to explore class cluster shapes and overlap (chapter 3).
- $\alpha$ -shapes are used to adapt the distance metric in a supervised fuzzy classification algorithm. A fuzzy classifier based on  $\alpha$ -shapes performs well (overall accuracy = 70 %). Several alternatives are proposed for classification improvement, based on  $\alpha$ -shapes as representations of membership functions (chapter 3).
- A focus group user test provides qualitative feedback about the applied visualisation methods. Users conclude that the visualisation tool improves insight into a fuzzy classification algorithm and related uncertainty (chapter 2).

## 9.2 Segmentation

- Split-and-merge segmentation is useful to extract objects from remotely sensed imagery. Segmentation homogeneity criteria have an important effect on the segmentation result. Several segmentation results can be generated with different segmentation thresholds to test object uncertainty. Existential object uncertainty can be quantified by the boundary stability index (*BSI*). It indicates object uncertainty as depicted by its boundary pixels (chapter 4).

- Several methods have been proposed and applied to validate segmentation results. Seven reference objects on a topographic map have been selected for segmentation validation. The percentage of overlap and the area fit index (*AFI*) of individual objects, are suitable measures for quantification of segmentation accuracy. To determine segmentation accuracy for the whole image, segment boundaries have been used to calculate the fit ( $D(B)$ ) with topographic reference boundaries. A correction factor ( $D(B)_{corr}$ ) has been proposed to correct for the number of boundary pixels in the segmented image. These measures are suitable to depict overall segmentation accuracy based on boundaries (chapter 4).
- The split-and-merge segmentation algorithm has been extended to include texture. Texture is modelled with the joint distribution of the local binary pattern (LBP) operator and local variance. Additionally, object uncertainty values provide important information to identify transition zones between fuzzy objects. The proposed algorithm provides good segmentation results for a test case study with a composite image of five different textures (96% accuracy).
- The algorithm has been tested on a LiDAR DSM and CASI image of a coastal area on the northwest coast of England. Good segmentation results have been obtained for the extraction of land form objects from the LiDAR DSM (overall accuracy = 86%). Uncertainty values provide meaningful information about transition zones between the different land forms. Segmentation of land cover objects from the CASI image yields an overall accuracy of 71% (chapter 5).
- To improve segmentation of land cover objects from multi-spectral imagery, the univariate LBP texture measure has been extended to model multivariate texture. The multivariate LBP texture operator models within and between band pixel relations in three bands. In combination with an RGB colour histogram, it provides a model for multivariate texture-based segmentation.
- An overall accuracy of 98% has been obtained for segmentation of an artificial image with a composition of colour textures. Three bands of the CASI image are used to improve segmentation of land cover classes. Compared to the segmentation result based on a univariate texture model, the multivariate texture-based segmentation algorithm yields better results (overall accuracy = 77%). The second case study, involves segmentation of geological units from ASTER and Landsat imagery of an area in Mongolia. Meaningful geological units are derived (overall accuracy = 77%) providing a useful technique for updating existing maps (chapter 6).

- To improve identification of land form objects, the LBP texture measure is extended with a multi-resolution neighbourhood model to model multi-scale texture. The combination of multi-scale LBP, variance measures and elevation values provide input for a region growing segmentation algorithm. As an application, a LiDAR DSM of a coastal area in England is segmented, yielding unlabelled land form objects. Additionally, a pixel uncertainty value is based on a (merging) similarity measure. These uncertainty values provide valuable information about transition zones between objects (chapter 7).

### 9.3 Object uncertainty visualisation

- In chapter 8, spheres, ellipsoids, convex hulls, isosurfaces, and  $\alpha$ -shapes are used and compared for visualisation of objects in a 3D feature space plot. These objects are derived either by visual classification or segmentation.  $\alpha$ -shapes provide the most accurate representation, however, computational demands are very high, making them unsuitable for fast interactions. Alternatively, an isosurface can provide a good approximation of an  $\alpha$ -shape, facilitating fast interaction (chapter 8).
- Isosurfaces allow for real-time rendering and interaction with a user-defined uncertainty threshold. Interaction with an uncertainty threshold showed the change of an isosurface for a changing threshold, providing an indication for thematic object uncertainty (chapter 8).
- The visualisation techniques are tested in two case studies. The first case study concerns visualisation of uncertainty for objects derived from a visual fuzzy classifier of a Landsat image of an area in southern France. The second case study concerns uncertainty visualisation of objects derived by multivariate texture-based segmentation from a CASI image of the Ainsdale Sand, UK. These case studies show that visual interaction with an uncertainty threshold and a dynamic link between feature space and geographic space, using a 3D feature space plot and an image display respectively, provides a powerful tool for exploration of the relation between uncertainty in the spatial extent of objects and their thematic uncertainty (chapter 8).

# Bibliography

- Aguado, A. S., Montiel, E. and Nixon, M. S. (1998). Fuzzy image segmentation via texture density histograms, EU project Nr. ENV4-CT96-0305 - Fuzzy Land Information from Environmental Remote Sensing (FLIERS) Final Report.
- Andrienko, G. L. and Andrienko, N. V. (1999). Interactive maps for visual data exploration, *International Journal of Geographical Information Science* **13**: 355–374.
- Bastin, L., Fisher, P. F. and Wood, J. (2002). Visualizing uncertainty in multi-spectral remotely sensed imagery, *Computers & Geosciences* **28**(3): 337–350.
- Benz, U. C., Hofmann, P., Willhauck, G., Lingenfelder, I. and M. Heynen (2004). Multi-resolution, object-oriented fuzzy analysis of remote sensing data for GIS-ready information, *ISPRS Journal of Photogrammetry and Remote Sensing* **58**(3–4): 239–258.
- Bertin, J. (1967). *Semiologie Graphique: Les Diagrammes, Les Reseaux, Les Cartes*, Mouton and Gauthiers-Villars.
- Bezdek, J. C. (1981). *Pattern Recognition with Fuzzy Objective Function Algorithms*, Plenum Press, New York.
- Blenkinsop, S., Fisher, P. F., Bastin, L. and Wood, J. (2000). Evaluating the perception of uncertainty in alternative visualization strategies, *Cartographica* **37**(1): 1–13.
- Bloomenthal, J. and Wyvill, B. (1997). *Introduction to Implicit Surfaces*, Morgan Kaufmann Publishers Inc., San Francisco, CA, USA.
- Bouman, C. and Liu, B. (1991). Multiple resolution segmentation of textured images, *IEEE Transactions on Pattern Analysis and Machine Intelligence* **13**: 99–113.
-

- Burrough, P. A. and Frank, A. U. (1996). *Geographic Objects with Indeterminate Boundaries*, number 2 in *GISDATA*, Taylor and Francis.
- Burrough, P. A. and McDonnell, R. A. (1998). *Principles of Geographical Information Systems*, Spatial Information Systems and Geostatistics, Oxford University Press.
- Campbell, J. B. (2002). *Introduction to Remote Sensing*, third edn, Taylor and Francis, London.
- Canter, F. (1997). Evaluating the uncertainty of area estimates derived from fuzzy land cover classification, *Photogrammetric Engineering & Remote Sensing* **63**(4): 403–414.
- CGAL (2004). Computational geometry algorithms library (CGAL).  
**URL:** <http://www.cgal.org>
- Cheng, T., Fisher, P. F. and Rogers, P. (2002). Fuzziness in multi-scale fuzzy assignment of duneness, in G. Hunter and K. Lowell (eds), *Accuracy 2002 - 5<sup>th</sup> International Symposium On Spatial Accuracy Assessment in Natural Resources and Environmental Sciences*, Melbourne, Australia, pp. 154–159.
- Cheng, T. and Molenaar, M. (1999). Objects with fuzzy spatial extent, *Photogrammetric Engineering and Remote Sensing* **63**: 403–414.
- Cheng, T. and Molenaar, M. (2001). Formalizing fuzzy objects from uncertain classification results, *International Journal of Geographical Information Science* **15**(1): 27–42.
- Clarkson, K. (2004). hull – convex hulls, delauney triangulations, alpha shapes.  
**URL:** <http://netlib.bell-labs.com/netlib/voronoi/hull.html>
- Congalton, R. G. (1991). A review of assessing the accuracy of classifications of remotely sensed data, *Remote Sensing of Environment* **37**: 35–46.
- Delves, L. M., Wilkinson, R., Oliver, C. J. and White, R. G. (1992). Comparing the performance of SAR image segmentation algorithms, *International Journal of Remote Sensing* **13**(11): 2121–2149.
- Dey, T. K. and Zhao, W. (2002). Approximate medial axis as a voronoi subcomplex, *Proceedings of the 7th ACM Symposium on Solid Modeling and Applications*, pp. 356–366.
- Drury, S. A. (1993). *Image Interpretation in Geology*, second edn, Chapman and Hall.

- Dykes, J. A. (1997). Exploring spatial data representation with dynamic graphics, *Computers & Geosciences* **23**(4): 345–370.
- eCognition (2004). User guide, *Technical report*, Definiens Imaging GmbH, Munich.  
**URL:** <http://www.definiens-imaging.com>
- Edelsbrunner, H. and Mücke, E. P. (1994). Three-dimensional alpha shapes, *ACM Transactions on Graphics* **13**(1): 43–72.
- Ehlschlaeger, C. R., Shortridge, A. M. and Goodchild, M. F. (1997). Visualizing spatial data uncertainty using animation, *Computers & Geosciences* **23**: 387–395.
- Evans, I. (1977). The selection of class intervals, *Transactions of the Institute of British Geographers (NS)* **2**: 98–124.
- Fenstermaker, L. (1994). *Remote Sensing Thematic Accuracy Assessment: a Compendium*, American Society for Photogrammetry and Remote Sensing (ASPRS), Bethesda.
- Fischer, K. (2004). Introduction to alpha shapes.  
**URL:** <http://n.ethz.ch/student/fischerk/alphashapes/as/>
- Fisher, P. (1994). Visualization of the reliability in classified remotely sensed images, *Photogrammetric Engineering and Remote Sensing* **60**(7): 905–910.
- Fisher, P. F. (1999). *Geographical Information Systems: Vol. 1 Principles and Technical Issues, Vol. 2 Management Issues and Applications*, second edition edn, Wiley & Sons, New York, chapter Models of Uncertainty in Spatial Data, pp. 191–205.
- Fisher, P. F. (2000). Sorites paradox and vague geographies, *Fuzzy Sets and Systems* **113**: 7–18.
- Fisher, P. F., Cheng, T. and Wood, J. (2004). Where is Helvellyn? Multiscale morphometry and the mountains of the English Lake District, *Transactions of the Institute of British Geographers* **29**: 106–128.
- Fisher, P. F., Wood, J. and Cheng, T. (in press). *Fuzzy Modeling with Spatial Information for Geographic Problems*, Springer, chapter Fuzziness and Ambiguity in Multi-scale Analysis of Landscape Morphometry.
- Foody, G. M. (1992). On the compensation for chance agreement in image classification accuracy assessment, *Photogrammetric Engineering & Remote Sensing* **58**: 1459–1460.

- Foody, G. M. (1996). Approaches for the production and evaluation of fuzzy land cover classifications from remotely sensed data, *International Journal of Remote Sensing* **17**(1): 1317–1340.
- Foody, G. M. and Atkinson, P. M. (2002). *Uncertainty in Remote Sensing and GIS*, John Wiley & Sons Ltd.
- Glasbey, C. A. and Horgan, G. W. (1995). *Image Analysis for the Biological Sciences*, John Wiley & Sons.
- Goodchild, M. F., Battenfield, B. and Wood, J. (1994). Introduction to visualizing data validity, in H. Hearnshaw and D. Unwin (eds), *Visualization in Geographical Information Systems*, Wiley & Sons, Chichester, pp. 141–149.
- Gorte, B. H. H. (1998). *Probabilistic Segmentation of Remotely Sensed Images*, PhD thesis, Wageningen Agricultural University.
- Gorte, B. H. H. and Stein, A. (1998). Bayesian classification and class area estimation of satellite images using stratification, *IEEE Transaction on Geoscience and Remote Sensing* **36**(3): 803–812.
- Haralick, R. M., Shanmugam, K. and Dinstein, I. (1973). Textural features for image classification, *IEEE Transactions on Systems, Man and Cybernetics* **2**: 610–621.
- Haralick, R. M. and Shapiro, L. G. (1985). Image segmentation techniques, *Computer Vision, Graphics and Image Processing* **29**(1): 100–132.
- Harrower, M., MacEachren, A. M. and Griffin, A. (2000). Developing a geographic visualization tool to support Earth science learning, *Cartography and Geographic Information Science* **27**: 279–294.
- Hauser, H., Ledermann, F. and Doleisch, H. (2002). Angular brushing for extended parallel coordinates, *Proceedings of the IEEE Symposium on Information Visualization 2002 (InfoVis 2002)*, Boston, MA, pp. 127–130.
- Hazel, C. G. (2000). Multivariate Gaussian MRF for multispectral scene segmentation and anomaly detection, *IEEE Transactions on Geoscience and Remote Sensing* **38**: 1199–1211.
- Hootsmans, R. M. (1996). *Fuzzy Sets and Series analysis for Visual Decision Support in Spatial Data Exploration*, PhD thesis, Utrecht University.
- Horowitz, S. L. and Pavlidis, T. (1976). Picture segmentation by a tree traversal algorithm, *Journal of the Association for Computing Machinery* **23**: 368–388.

- Inselberg, A. (1985). The plane with parallel coordinates, *The Visual Computer* **1**: 69–91.
- Inselberg, A. (1998). Multidimensional detective, *IEEE Proceedings of Information Visualization '97*, pp. 100–107.
- Kessler, F. C. (2000). Focus groups as a means of qualitatively assessing the U-boat narrative, *Cartographica* **37**(33–60).
- Kraak, M. J. and MacEachren, A. M. (1999). Visualization for exploration of spatial data, *International Journal of Geographical Information Science* **13**: 285–287. Guest editorial of a special issue on GeoVisualization.
- Ledermann, F. (2004). Parvis parallel coordinate visualisation.  
**URL:** <http://home.subnet.at/flo/mv/parvis>
- Levoy, M. and Whitted, T. (1985). The use of points as a display primitive, *Technical Report 85-022*, Computer Science Department, University of North Carolina at Chapel Hill.  
**URL:** <http://graphics.stanford.edu/papers/points/>
- Li, F. and Peng, J. (2004). Double random field model for remote sensing image segmentation, *Pattern Recognition Letters* **25**(1): 129–139.
- Lillesand, T. M. and Kiefer, R. W. (2000). *Remote Sensing and Image Interpretation*, fourth edn, Wiley and Sons, New York.
- Lorenson, W. E. and Cline, H. E. (1987). Marching cubes: A high resolution 3D surface construction algorithm, *Proceedings of the 14th annual conference on Computer graphics and interactive techniques*, ACM Press, pp. 163–169.  
**URL:** <http://doi.acm.org/10.1145/37401.37422>
- Lucieer, A. (2004). The homepage of Arko Lucieer.  
**URL:** <http://www.lucieer.net>
- Lucieer, A., Koster, E. H., de Jong, S. M. and Jetten, V. G. (2000). The DAIS La Peyne experiment: Using the optical and thermal DAIS bands to survey and model the surface temperature, *International Archives of Photogrammetry and Remote Sensing*, Vol. XXXIII, GITC, Amsterdam.
- Lucieer, A. and Kraak, M. J. (2002). Interactive visualization of a fuzzy classification of remotely sensed imagery using dynamically linked views to explore uncertainty, in G. Hunter and K. Lowell (eds), *Proceedings Accuracy 2002, 5th International Symposium On Spatial Accuracy Assessment in Natural Resources and Environmental Sciences*, Melbourne, Australia, pp. 348–356.

- Lucieer, A. and Kraak, M. J. (2004). Interactive and visual fuzzy classification of remotely sensed imagery for exploration of uncertainty, *International Journal of Geographical Information Science* **18**(5): 491–512.
- Lucieer, A. and Stein, A. (2002). Existential uncertainty of spatial objects segmented from satellite sensor imagery, *IEEE Transactions on Geoscience and Remote Sensing* **40**(11): 2518–2521.
- MacEachren, A. M. (1992). Visualizing uncertain information, *Cartographic Perspectives* **13**: 10–19.
- MacEachren, A. M. (1994). *Visualization in Modern Cartography*, Vol. Two of *Modern Cartography*, Pergamon - Elsevier Science, chapter Visualization in Modern Cartography: Setting the Agenda, pp. 149–166.
- MacEachren, A. M. and Kraak, M. J. (1997). Exploratory cartographic visualization: Advancing the agenda, *Computers & Geosciences* **23**(4): 335–343.
- MacEachren, A. M. and Kraak, M. J. (2001). Research challenges in geovisualization, *Cartography and Geographic Information Systems* **28**(1): 3–12.
- MacEachren, A. M., Wachowicz, M., Edsall, R., Haug, D. and Masters, R. (1999). Constructing knowledge from multivariate spatiotemporal data: Integrating geographical visualization with knowledge discovery in database methods, *International Journal of Geographical Information Science* **13**: 311–334.
- MacKinaly, S. K. C. J. D. and Schneiderman, B. (1999). *Readings in Information Visualizations, Using Vision to Think*, Morgan Kaufmann Publishers, Inc., San Francisco, California, USA.
- Mojsilovic, A., Kovacevic, J., Hu, J., Safranek, R. J. and Ganapathy, S. K. (2000). Matching and retrieval based on the vocabulary and grammar of color patterns, *IEEE Transactions on Image Processing* **9**(1): 38–54.
- Molenaar, M. (1998). *An Introduction to the Theory of Spatial Object Modelling for GIS*, Taylor & Francis.
- Molenaar, M. (2000). Three conceptual uncertainty levels for spatial objects, *International Archives of Photogrammetry and Remote Sensing. Vol. XXXIII, Part B4*, ISPRS IC WG IV/III.1 – GIS Fundamentals and Spatial Databases, Amsterdam.
- Molenaar, M. and Cheng, T. (2000). Fuzzy spatial objects and their dynamics, *ISPRS Journal of Photogrammetry & Remote Sensing* **55**: 164–175.

- Monmonier, M. (1989). Geographic brushing: Enhancing exploratory analysis of the scatterplot matrix, *Geographical Analysis* **21**(1): 81–84.
- Morgan, D. L. (1998). *The Focus Group Guidebook — Focus Group Kit 1*, Sage Publications.
- Nixon, M. S. and Aguado, A. S. (2002). *Feature Extraction & Image Processing*, Newnes.
- Ojala, T., Mäenpää, T., Pietikäinen, M., Viertola, J., Kyllönen, J. and Huovinen, S. (2002). Outex - new framework for empirical evaluation of texture analysis algorithms, *16<sup>th</sup> International Conference on Pattern Recognition*, Vol. 1, Quebec, Canada, pp. 701–706.  
**URL:** <http://www.outex.oulu.fi>
- Ojala, T. and Pietikäinen, M. (1999). Unsupervised texture segmentation using feature distributions, *Pattern Recognition* **32**: 477–486.
- Ojala, T., Pietikäinen, M. and Harwood, D. (1996). A comparative study of texture measures with classification based on feature distributions, *Pattern Recognition* **29**: 51–59.
- Ojala, T., Pietikäinen, M. and Mäenpää, T. (2002). Multiresolution gray-scale and rotation invariant texture classification with local binary patterns, *IEEE Transactions on Pattern Analysis and Machine Intelligence* **24**(7): 971–987.
- Panjwani, D. K. and Healey, G. (1995). Markov random field models for unsupervised segmentation of textured color images, *IEEE Transactions on Pattern Analysis and Machine Intelligence* **17**(10): 939–954.
- Pietikäinen, M., Mäenpää, T. and Viertola, J. (2002). Color texture classification with color histograms and local binary patterns, *Proceedings of the Second International Workshop on Texture Analysis and Synthesis*, Copenhagen, Denmark, pp. 109–112.
- Pietikäinen, M., Ojala, T. and Xu, Z. (2000). Rotation-invariant texture classification using feature distributions, *Pattern Recognition* **33**: 43–52.
- Poirson, B. and Wandell, B. A. (1996). Pattern-color separable pathways predict sensitivity to simple colored patterns, *Vision Research* **36**(4): 515–526.
- Prieto, M. S. and Allen, A. R. (2003). A similarity metric for edge images, *IEEE Transactions on Pattern Analysis and Machine Intelligence* **25**(10): 1265–1273.

- Randen, T. and Husøy, J. H. (1999). Filtering for texture classification: A comparative study, *IEEE Transactions on Pattern Analysis and Machine Intelligence* **21**: 291–310.
- Richards, J. A. and Jia, X. (1999). *Remote Sensing Digital Image Analysis - An Introduction*, third edn, Springer, Berlin.
- Rosenfield, G. H., Fitzpatrick, L. K. and Ling, H. S. (1982). Sampling for thematic map accuracy testing, *Photogrammetric Engineering and Remote Sensing* **48**: 131–137.
- Rusinkiewicz, S. and Levoy, M. (2000). QSplat: A multiresolution point rendering system for large meshes, in K. Akeley (ed.), *Siggraph 2000, Computer Graphics Proceedings*, ACM Press / ACM SIGGRAPH / Addison Wesley Longman, pp. 343–352.  
**URL:** <http://graphics.stanford.edu/software/qsplat/>
- Sande, C., de Jong, S. M. and Roo, A. (2003). A segmentation and classification approach of IKONOS-2 imagery, *International Journal of Applied Earth Observation and Geoinformation* **4**(3): 217–229.
- Sarkar, A., Biswas, M. K., Kartikeyan, B., Kumar, V., Majumder, K. L. and Pal, D. K. (2002). MRF model-based segmentation approach to classification for multispectral imagery, *IEEE Transactions on Geoscience and Remote Sensing* **40**: 1102–1113.
- Sefton Coast Partnership (2004). Sefton coast partnership — nature conservation.  
**URL:** <http://www.seftoncoast.org.uk>
- Sluiter, R. (2004). Homepage Raymond Sluiter - modelling ecological processes using high resolution hyperspectral remote sensing images.  
**URL:** <http://sluiter.geog.uu.nl>
- Sokal, P. R. and Rohlf, F. J. (1987). *Introduction to Biostatistics, 2nd Edition*, W. H. Freeman, New York.
- Stehman, S. V. (1992). Comparison of systematic and random sampling for estimating the accuracy of maps generated from remotely sensed data, *Photogrammetric Engineering & Remote Sensing* **58**: 181–194.
- Stein, A. and Ettema, C. (2003). An overview of spatial sampling procedures and experimental design of spatial studies for ecosystem comparisons, *Agriculture, Ecosystems and Environment* **94**: 31–47.

- Sun Microsystems Inc. (2004). The source for Java(TM) technology.  
**URL:** <http://java.sun.com>
- Tso, B. and Mather, P. M. (2001). *Classification Methods for Remotely Sensed Data*, Taylor and Francis.
- Varzi, A. C. (2001). Vagueness in geography, *Philosophy & Geography* **4**(1): 49–65.
- Walter, V. (2004). Object-based classification of remote sensing data for change detection, *ISPRS Journal of Photogrammetry and Remote Sensing* **58**(3–4): 225–238.
- Wang, F. (1990). Improving remote sensing image analysis through fuzzy information representation, *Photogrammetric Engineering & Remote Sensing* **56**: 1163–1169.
- Wel, F. . M. v. d. (2000). *Assessment and Visualisation of Uncertainty in Remote Sensing Land Cover Classifications*, PhD thesis, Utrecht University.
- Wel, F. J. M. v. d., Gaag, L. C. v. d. and Gorte, B. G. H. (1997). Visual exploration of uncertainty in remote sensing classification, *Computers & Geosciences* **24**(4): 335–343.
- Zadeh, L. A. (1965). Fuzzy sets, *Information and Control* **8**: 338–353.
- Zhan, Q. (2003). *A Hierarchical Object-Based Approach for Urban Land-Use Classification from Remote Sensing Data*, PhD thesis, Wageningen University.
- Zhang, J. and Foody, G. M. (2001). Fully-fuzzy supervised classification of sub-urban land cover from remotely sensed imagery: Statistical and artificial neural network approaches, *International Journal of Remote Sensing* **22**(4): 615–628.

*Bibliography*

---

# ITC Dissertations

- [1] **Akinyede, Joseph O.**, 1990, *Highway Cost Modelling and Route Selection Using a Geotechnical Information System*, Delft University of Technology.
  - [2] **Pan, Ping He**, 1990, *A Spatial Structure Theory in Machine Vision and Applications to Structural and Textural Analysis of Remotely Sensed Images*, University of Twente, 90-9003757-8.
  - [3] **Bocco Verdinelli, Gerardo H. R.**, 1990, *Gully Erosion Analysis Using Remote Sensing and Geographic Information Systems: A Case Study in Central Mexico*, Universiteit van Amsterdam.
  - [4] **Sharif, Massoud**, 1991, *Composite Sampling Optimization for DTM in the Context of GIS*, Wageningen Agricultural University.
  - [5] **Drummond, Jane E.**, 1991, *Determining and Processing Quality Parameters in Geographic Information Systems*, University of Newcastle.
  - [6] **Groten, Susanne**, 1991, *Satellite Monitoring of Agro-ecosystems in the Sahel*, Westfälische Wilhelms-Universität.
  - [7] **Sharifi, Ali**, 1991, *Development of an Appropriate Resource Information System to Support Agricultural Management at Farm Enterprise Level*, Wageningen Agricultural University, 90-6164-074-1.
  - [8] **van der Zee, Dick**, 1991, *Recreation Studied from Above: Air Photo Interpretation as Input into Land Evaluation for Recreation*, Wageningen Agricultural University, 90-6164-075-X.
  - [9] **Mannaerts, Chris**, 1991, *Assessment of the Transferability of Laboratory Rainfall-runoff and Rainfall—Soil Loss Relationships to Field and Catchment Scales: A Study in the Cape Verde Islands*, University of Ghent, 90-6164-085-7.
-

- [10] **Wang, Ze Shen**, 1991, *An Expert System for Cartographic Symbol Design*, Utrecht University, 90-3930-333-9.
- [11] **Zhou, Yunxuan**, 1991, *Application of Radon Transforms to the Processing of Airborne Geophysical Data*, Delft University of Technology, 90-6164-081-4.
- [12] **de Zuviria, Martín**, 1992, *Mapping Agro-topoclimates by Integrating Topographic, Meteorological and Land Ecological Data in a Geographic Information System: A Case Study of the Lom Sak Area, North Central Thailand*, Universiteit van Amsterdam, 90-6164-077-6.
- [13] **van Westen, Cees J.**, 1993, *Application of Geographic Information Systems to Landslide Hazard Zonation*, Delft University of Technology, 90-6164-078-4.
- [14] **Shi, Wenzhong**, 1994, *Modelling Positional and Thematic Uncertainties in Integration of Remote Sensing and Geographic Information Systems*, Universität Osnabrück, 90-6164-099-7.
- [15] **Javelosa, R.**, 1994, *Active Quaternary Environments in the Philippine Mobile Belt*, Utrecht University, 90-6164-086-5.
- [16] **Lo, King-Chang**, 1994, *High Quality Automatic DEM, Digital Elevation Model Generation from Multiple Imagery*, University of Twente, 90-9006-526-1.
- [17] **Wokabi, S. M.**, 1994, *Quantified Land Evaluation for Maize Yield Gap Analysis at Three Sites on the Eastern Slope of Mt. Kenya*, University Ghent, 90-6164-102-0.
- [18] **Rodríguez Parisca, O. S.**, 1995, *Land Use Conflicts and Planning Strategies in Urban Fringes: A Case Study of Western Caracas, Venezuela*, University of Ghent.
- [19] **van der Meer, Freek D.**, 1995, *Imaging Spectrometry & the Ronda Peridotites*, Wageningen Agricultural University, 90-5485-385-9.
- [20] **Kufoniya, Olajide**, 1995, *Spatial Coincidence: Automated Database Updating and Data Consistency in Vector GIS*, Wageningen Agricultural University, 90-6164-105-5.
- [21] **Zambezi, P.**, 1995, *Geochemistry of the Nkombwa Hill Carbonatite Complex of Isoka District, North-east Zambia, with Special Emphasis on Economic Minerals*, Vrije Universiteit Amsterdam.

- [22] **Woldai, Tsehaie**, 1995, *The Application of Remote Sensing to the Study of the Geology and Structure of the Carboniferous in the Calañas Area, Pyrite Belt, South-west Spain*, Open University, United Kingdom.
- [23] **Verweij, Pita A.**, 1995, *Spatial and Temporal Modelling of Vegetation Patterns: Burning and Grazing in the Páramo of Los Nevados National Park, Colombia*, Universiteit van Amsterdam, 90-6164-109-8.
- [24] **Pohl, Christine**, 1996, *Geometric Aspects of Multisensor Image Fusion for Topographic Map Updating in the Humid Tropics*, Universität Hannover, 90-6164-121-7.
- [25] **Bin, Jiang**, 1996, *Fuzzy Overlay Analysis and Visualization in Geographic Information Systemes*, Utrecht University, 90-6266-128-9.
- [26] **Metternicht, Graciela I.**, 1996, *Detecting and Monitoring Land Degradation Features and Processes in the Cochabamba Valleys, Bolivia. A Synergistic Approach*, University of Ghent, 90-6164-118-7.
- [27] **Chu Thai Hoanh**, 1996, *Development of a Computerized Aid to Integrated Land Use Planning (CAILUP) at Regional Level in Irrigated Areas: A Case Study for the Quan Lo Phung Hiep region in the Mekong Delta, Vietnam*, Wageningen Agricultural University, 90-6164-120-9.
- [28] **Roshannejad, A.**, 1996, *The Management of Spatio-Temporal Data in a National Geographic Information System*, University of Twente, 90-9009-284-6.
- [29] **Terlien, Mark T. J.**, 1996, *Modelling Spatial and Temporal Variations in Rainfall-triggered Landslides: The Integration of Hydrologic Models, Slope Stability Models and GIS for the Hazard Zonation of Rainfall-triggered Landslides with Examples from Manizales, Colombia*, Utrecht University, 90-6164-115-2.
- [30] **Mahavir, J.**, 1996, *Modelling Settlement Patterns for Metropolitan Regions: Inputs from Remote Sensing*, Utrecht University, 90-6164-117-9.
- [31] **Al-Amir, Sahar**, 1996, *Modern Spatial Planning Practice as Supported by the Multi-applicable Tools of Remote Sensing and GIS: The Syrian Case*, Utrecht University, 90-6164-116-0.
- [32] **Pilouk, M.**, 1996, *Integrated Modelling for 3D GIS*, University of Twente, 90-6164-122-5.

- [33] **Duan, Zengshan**, 1996, *Optimization Modelling of a River-Aquifer System with Technical Interventions: A Case Study for the Huangshui River and the Coastal Aquifer, Shandong, China*, Vrije Universiteit Amsterdam, 90-6164-123-3.
- [34] **de Man, W. H. E.**, 1996, *Surveys: Informatie als Norm: Een Verkenning van de Institutionaliserings van Dorp-surveys in Thailand en op de Filippijnen*, University of Twente, 90-9009-775-9.
- [35] **Vekerdy, Zoltan**, 1996, *GIS-based Hydrological Modelling of Alluvial Regions: Using the Example of the Kisafld, Hungary*, Lorand Eotvos University of Sciences, 90-6164-119-5.
- [36] **Gomes Pereira, Luisa M.**, 1996, *A Robust and Adaptive Matching Procedure for Automatic Modelling of Terrain Relief*, Delft University of Technology, 90-407-1385-5.
- [37] **Fandiño Lozano, M. T.**, 1996, *A Framework of Ecological Evaluation oriented at the Establishment and Management of Protected Areas: A Case Study of the Santuario de Iguaque, Colombia*, Universiteit van Amsterdam, 90-6164-129-2.
- [38] **Toxopeus, Bert**, 1996, *ISM: An Interactive Spatial and Temporal Modelling System as a Tool in Ecosystem Management: With Two Case Studies: Cibodas Biosphere Reserve, West Java Indonesia; Amboseli Biosphere Reserve, Kajiado District, Central Southern Kenya*, Universiteit van Amsterdam, 90-6164-126-8.
- [39] **Wang, Yiman**, 1997, *Satellite SAR Imagery for Topographic Mapping of Tidal Flat Areas in the Dutch Wadden Sea*, Universiteit van Amsterdam, 90-6164-131-4.
- [40] **Saldana Lopez, Asun**, 1997, *Complexity of Soils and Soilscape Patterns on the Southern Slopes of the Ayllon Range, Central Spain: a GIS Assisted Modelling Approach*, Universiteit van Amsterdam, 90-6164-133-0.
- [41] **Ceccarelli, T.**, 1997, *Towards a Planning Support System for Communal Areas in the Zambezi Valley, Zimbabwe; A Multi-criteria Evaluation Linking Farm Household Analysis, Land Evaluation and Geographic Information Systems*, Utrecht University, 90-6164-135-7.
- [42] **Peng, Wanning**, 1997, *Automated Generalization in GIS*, Wageningen Agricultural University, 90-6164-134-9.

- [43] **Mendoza Lawas, M. C.**, 1997, *The Resource Users' Knowledge, the Neglected Input in Land Resource Management: The Case of the Kankanaey Farmers in Benguet, Philippines*, Utrecht University, 90-6164-137-3.
- [44] **Bijker, Wietske**, 1997, *Radar for Rain Forest: A Monitoring System for Land Cover Change in the Colombian Amazon*, Wageningen Agricultural University, 90-6164-139-X.
- [45] **Farshad, Abbas**, 1997, *Analysis of Integrated Soil and Water Management Practices within Different Agricultural Systems under Semi-arid Conditions of Iran and Evaluation of their Sustainability*, University of Ghent, 90-6164-142-X.
- [46] **Orlic, B.**, 1997, *Predicting Subsurface Conditions for Geotechnical Modelling*, Delft University of Technology, 90-6164-140-3.
- [47] **Bishr, Yaser**, 1997, *Semantic Aspects of Interoperable GIS*, Wageningen Agricultural University, 90-6164-141-1.
- [48] **Zhang, Xiangmin**, 1998, *Coal fires in Northwest China: Detection, Monitoring and Prediction Using Remote Sensing Data*, Delft University of Technology, 90-6164-144-6.
- [49] **Gens, Rudiger**, 1998, *Quality Assessment of SAR Interferometric Data*, University of Hannover, 90-6164-155-1.
- [50] **Turkstra, Jan**, 1998, *Urban Development and Geographical Information: Spatial and Temporal Patterns of Urban Development and Land Values Using Integrated Geo-data, Villaviciencio, Colombia*, Utrecht University, 90-6164-147-0.
- [51] **Cassells, Craig James Steven**, 1998, *Thermal Modelling of Underground Coal Fires in Northern China*, University of Dundee.
- [52] **Naseri, M. Y.**, 1998, *Monitoring Soil Salinization, Iran*, Ghent University, 90-6164-195-0.
- [53] **Gorte, Ben G. H.**, 1998, *Probabilistic Segmentation of Remotely Sensed Images*, Wageningen Agricultural University, 90-6164-157-8.
- [54] **Ayenew, Tenalem**, 1998, *The Hydrological System of the Lake District Basin, Central Main Ethiopian Rift*, Universiteit van Amsterdam, 90-6164-158-6.

- [55] **Wang, Donggen**, 1998, *Conjoint Approaches to Developing Activity-Based Models*, Technical University of Eindhoven, 90-6864-551-7.
- [56] **Bastidas de Calderon, María**, 1998, *Environmental Fragility and Vulnerability of Amazonian Landscapes and Ecosystems in the Middle Orinoco River Basin, Venezuela*, University of Ghent.
- [57] **Moameni, A.**, 1999, *Soil Quality Changes under Long-term Wheat Cultivation in the Marvdasht Plain, South-central Iran*, University of Ghent.
- [58] **van Groenigen, J.W.**, 1999, *Constrained Optimisation of Spatial Sampling: A Geostatistical Approach*, Wageningen Agricultural University, 90-6164-156-X.
- [59] **Cheng, Tao**, 1999, *A Process-oriented Data Model for Fuzzy Spatial Objects*, Wageningen Agricultural University, 90-6164-164-0.
- [60] **Wolski, Piotr**, 1999, *Application of Reservoir Modelling to Hydrotopes Identified by Remote Sensing*, Vrije Universiteit Amsterdam, 90-6164-165-9.
- [61] **Acharya, B.**, 1999, *Forest Biodiversity Assessment: A Spatial Analysis of Tree Species Diversity in Nepal*, Leiden University, 90-6164-168-3.
- [62] **Abkar, Ali Akbar**, 1999, *Likelihood-based Segmentation and Classification of Remotely Sensed Images*, University of Twente, 90-6164-169-1.
- [63] **Yanuariadi, Tetra**, 1999, *Sustainable Land Allocation: GIS-based Decision Support for Industrial Forest Plantation Development in Indonesia*, Wageningen University, 90-5808-082-X.
- [64] **Abu Bakr, Mohamed**, 1999, *An Integrated Agro-Economic and Agro-Ecological Framework for Land Use Planning and Policy Analysis*, Wageningen University, 90-6164-170-5.
- [65] **Eleveld, Marieke A.**, 1999, *Exploring Coastal Morphodynamics of Aemland (The Netherlands) with Remote Sensing Monitoring Techniques and Dynamic Modelling in GIS*, Universiteit van Amsterdam, 90-6461-166-7.
- [66] **Hong, Yang**, 1999, *Imaging Spectrometry for Hydrocarbon Microseepage*, Delft University of Technology, 90-6164-172-1.
- [67] **Mainam, Félix**, 1999, *Modelling Soil Erodibility in the Semiarid Zone of Cameroon*, University of Ghent, 90-6164-179-9.

- [68] **Bakr, Mahmoud I.**, 2000, *A Stochastic Inverse-Management Approach to Groundwater Quality*, Delft University of Technology, 90-6164-176-4.
- [69] **Zlatanova, Siyka**, 2000, *3D GIS for Urban Development*, Graz University of Technology, 90-6164-178-0.
- [70] **Ottichilo, Wilber K.**, 2000, *Wildlife Dynamics: An Analysis of Change in the Masai Mara Ecosystem*, Wageningen University, 90-5808-197-4.
- [71] **Kaymakci, Nuri**, 2000, *Tectono-stratigraphical Evolution of the Cankori Basin (Central Anatolia, Turkey)*, Utrecht University, 90-6164-181-0.
- [72] **Gonzalez, Rhodora**, 2000, *Platforms and Terraces: Bridging Participation and GIS in Joint-learning for Watershed Management with the Ifugaos of the Philippines*, Wageningen University, 90-5808-246-6.
- [73] **Schetselaar, Ernst**, 2000, *Integrated Analyses of Granite-gneiss Terrain from Field and Multisource Remotely Sensed Data. A Case Study from the Canadian Shield*, University of Delft, 90-6164-180-2.
- [74] **Mesgari, M. Saadi**, 2000, *Topological Cell-Tuple Structure for Three-Dimensional Spatial Data*, University of Twente, 90-3651-511-4.
- [75] **de Bie, Cees A. J. M.**, 2000, *Comparative Performance Analysis of Agro-Ecosystems*, Wageningen University, 90-5808-253-9.
- [76] **Khaemba, Wilson M.**, 2000, *Spatial Statistics for Natural Resource Management*, Wageningen University, 90-5808-280-6.
- [77] **Shrestha, Dhruba**, 2000, *Aspects of Erosion and Sedimentation in the Nepalese Himalaya: Highland-lowland Relations*, Ghent University, 90-6164-189-6.
- [78] **Asadi Haroni, Hooshang**, 2000, *The Zarshuran Gold Deposit Model Applied in a Mineral Exploration GIS in Iran*, Delft University of Technology, 90-6164-185-3.
- [79] **Raza, Ale**, 2001, *Object-Oriented Temporal GIS for Urban Applications*, University of Twente, 90-3651-540-8.
- [80] **Farah, Hussein O.**, 2001, *Estimation of Regional Evaporation under Different Weather Conditions from Satellite and Meteorological Data. A Case Study in the Naivasha Basin, Kenya*, Wageningen University, 90-5808-331-4.

- [81] **Zheng, Ding**, 2001, *A Neuro-Fuzzy Approach to Linguistic Knowledge Acquisition and Assessment in Spatial Decision Making*, University of Vechta, 90-6164-190-X.
- [82] **Sahu, B. K.**, 2001, *Aeromagnetism of Continental Areas Flanking the Indian Ocean; with Implications for Geological Correlation and Gondwana Reassembly*, University of Capetown, South Africa.
- [83] **Alfestawi, Yahia Ahmed M.**, 2001, *The Structural, Paleogeographical and Hydrocarbon Systems Analysis of the Ghadamis and Murzuq Basins, West Libya, with Emphasis on Their Relation to the Intervening Al Qarqaf Arch*, Delft Technical University, 90-6164-198-5.
- [84] **Liu, Xuehua**, 2001, *Mapping and Modelling the Habitat of Giant Pandas in Foping Nature Reserve, China*, Wageningen University, 90-5808-496-5.
- [85] **Oindo, Boniface Oluoch**, 2001, *Spatial Patterns of Species Diversity in Kenya*, Wageningen University, 90-5808-495-7.
- [86] **Carranza, Emmanuel John M.**, 2002, *Geologically-constrained Mineral Potential Mapping: Examples from the Philippines*, Technical University of Delft, 90-6164-203-5.
- [87] **Rugege, Denis**, 2002, *Regional Analysis of Maize-based Land Use Systems for Early Warning Applications*, Wageningen University, 90-5808-584-8.
- [88] **Liu, Yaolin**, 2002, *Categorical Database Generalization in GIS*, Wageningen University, 90-5808-648-8.
- [89] **Ogao, Patrick**, 2002, *Scientific Visualization*, Utrecht University, 90-6164-206-X.
- [90] **Abadi, Abdulbaset Musbah**, 2002, *Tectonics of the Sirt Basin: Inferences from Tectonic Subsidence Analysis, Stress Inversion and Gravity Modeling*, Vrije Universiteit Amsterdam, 90-6164-205-1.
- [91] **Geneletti, Davide**, 2002, *Ecological Evaluation for Environmental Impact Assessment*, Vrije Universiteit Amsterdam, 90-6809-337-1.
- [92] **Sedogo, Laurent D.**, 2002, *Integration of Local Participatory and Regional Planning for Resources Management Using Remote Sensing and GIS*, Wageningen University, 90-5808-751-4.
- [93] **Montoya, Ana Lorena**, 2002, *Urban Disaster Management: A Case Study of Earthquake Risk Assessment in Cartago, Costa Rica*, Utrecht University, 90-6164-2086.

- [94] **Mobin-ud Din, Ahmad**, 2002, *Estimation of Net Groundwater Use in Irrigated River Basins Using Geo-information Techniques: A Case Study in Rechna Doab, Pakistan*, Wageningen University, 90-5808-761-1.
- [95] **Said, Mohammed Yahya**, 2003, *Multiscale Perspectives of Species Richness in East Africa*, Wageningen University, 90-5808-794-8.
- [96] **Schmidt, Karen S.**, 2003, *Hyperspectral Remote Sensing of Vegetation Species Distribution in a Saltmarsh*, Wageningen University, 90-5808-830-8.
- [97] **López Binnqüist, Citlalli**, 2003, *The Endurance of Mexican Amate Paper: Exploring Additional dimensions to the Sustainable Development Concept*, University of Twente, 90-3651-900-4.
- [98] **Huang, Zhengdong**, 2003, *Data Integration for Urban Transport Planning*, Utrecht University, 90-6164-211-6.
- [99] **Cheng, Jianquan**, 2003, *Modelling Spatial and Temporal Urban Growth*, Utrecht University, 90-6164-212-4.
- [100] **Campos dos Santos, José Laurindo**, 2003, *A Biodiversity Information System in an Open Data-Metadatabase Architecture*, University of Twente, 90-6164-214-0.
- [101] **Hengl, Tomislav**, 2003, *Pedometric Mapping: Bridging the Gaps Between Conventional and Pedometric Approaches*, Wageningen University.
- [102] **Barrera Bassols, Narciso**, 2003, *Symbolism, Knowledge and management of Soil and Land Resources in Indigenous Communities: Ethnopedology at Global, Regional and Local Scales*, University of Ghent.
- [103] **Zhan, Qingming**, 2003, *A Hierarchical Object-based Approach for Urban Land-use Classification from Remote Sensing Data*, Wageningen University, 90-5808-917-7.
- [104] **Daag, Arturo Santos**, 2003, *Modelling the Erosion of the Pyroclastic Flow Deposits and the Occurrences of Lahars at Mt. Pinatubo, Philippines*, Utrecht University, 90-6164-218-3.
- [105] **Bacic, Ivan Luiz Zilli**, 2003, *Demand Driven Land Evaluation: With Case Studies in Santa Catarina, Brazil*, Wageningen University, 90-5808-902-9.
- [106] **Murwira, Amon**, 2003, *Scale matters! A New Approach to Quantify Spatial Heterogeneity for Predicting the Distribution of Wildlife*, Wageningen University.

- [107] **Mazvimavi, Dominic**, 2003, *Estimation of Flow Characteristics of Ungauged Catchments: A Case Study in Zimbabwe*, Wageningen University, 90-5808-950-9.
- [108] **Tang, Xinming**, 2004, *Spatial Object Modeling in Fuzzy Topological Spaces: With Applications to Land Cover Change*, University of Twente, 90-6164-2205.
- [109] **Kariuki, Patrick C.**, 2004, *Spectroscopy to Measure the Swelling Potential of Expansive Soils*, University of Delft, 90-6164-221-3.
- [110] **Morales, Javier**, 2004, *Model Driven Methodology for the Design of Geo-information Services*, University of Twente, 90-6164-222-1.
- [111] **Mutanga, Onesimo**, 2004, *Hyperspectral Remote Sensing of Tropical Grass Quality and Quantity*, University of Wageningen, 90-5808-981-9.
- [112] **Šliužas, Ričardas V.**, 2004, *Managing Informal Settlements: a Study Using Geo-information in Dar es Salaam, Tanzania*, University of Utrecht, 90-6164-223-X.

# Publications of the author

- Lucieer, A. and Stein, A. (in press). Texture-based landform segmentation of LiDAR imagery, *International Journal of Applied Earth Observation and Geoinformation*.
- Lucieer, A., Stein, A. and Fisher, P. F. (in review). Multivariate texture-based segmentation of remotely sensed imagery for extraction of objects and their uncertainty, *International Journal of Remote Sensing*.
- Lucieer, A., Veen, L. E. (in prep.). Visualisation of object uncertainty in remotely sensed imagery by 3D interactive isosurfaces, *Information Visualisation*.
- Lucieer, A. (in prep.). Parbat– a geovisualization tool for classification and segmentation of remote sensing images, *Computers and Geosciences*.
- Lucieer, A. and Kraak, M. J. (2004). Interactive and visual fuzzy classification of remotely sensed imagery for exploration of uncertainty, *International Journal of Geographical Information Science* **18**(5): 491–512.
- Lucieer, A., Fisher, P. F. and Stein, A. (2004). *GeoDynamics*, CRC Press LLC, chapter Texture-based Segmentation of Remotely Sensed Imagery to Identify Fuzzy Coastal Objects.
- Lucieer, A., Orkhonselenge, T. and Stein, A. (2004). Texture based segmentation for identification of geological units in remotely sensed imagery, in A. Frank and E. Grum (eds), *Proceedings of the 3<sup>rd</sup> International Symposium on Spatial Data Quality ISSDQ'04*, Technical University of Vienna, Bruck an der Leitha, Austria, pp. 117–120.
- Stein, A., Dilo, A., Lucieer, A. and Vlag, D. (2004). Definition and identification of vague spatial objects and their use in decision ontologies, in A. Frank and
-

- E. Grum (eds), *Proceedings of the 3<sup>rd</sup> International Symposium on Spatial Data Quality ISSDQ'04*, Technical University of Vienna, Bruck an der Leitha, Austria, pp. 99–115.
- Lucieer, A. and Kraak, M. J. (2004). Alpha-shapes for visualizing irregular shaped class clusters in 3D feature space for classification of remotely sensed imagery, *Proceedings Visualization and Data Analysis 2004, San Jose, USA*.
- Werff, H. M. A. v. d. and Lucieer, A. (2004). *Remote Sensing Image Analysis: Including the Spatial Domain*, Vol. 5 of *Remote Sensing and Digital Image Processing*, Kluwer Academic Publishers, Dordrecht, chapter A Contextual Algorithm for Detection of Mineral Alteration Halos with Hyperspectral Remote Sensing.
- Lucieer, A. (2004). The homepage of Arko Lucieer.  
**URL:** <http://www.lucieer.net>
- Lucieer, A., Stein, A. and Fisher, P. F. (2003). Texture-based segmentation of high-resolution remotely sensed imagery for identification of fuzzy objects, *Proceedings of GeoComputation 2003*, Southampton, UK.
- Lucieer, A., Fisher, P. F. and Stein, A. (2003). Fuzzy object identification using texture-based segmentation of high-resolution DEM and remote sensing imagery of a coastal area in England, *Proceedings of the Second International Symposium on Spatial Data Quality*, Hong Kong.
- Lucieer, A. and Stein, A. (2002). Existential uncertainty of spatial objects segmented from satellite sensor imagery, *IEEE Transactions on Geoscience and Remote Sensing* **40**(11): 2518–2521.
- Lucieer, A. and Kraak, M. J. (2002). Interactive visualization of a fuzzy classification of remotely sensed imagery using dynamically linked views to explore uncertainty, in G. Hunter and K. Lowell (eds), *Proceedings Accuracy 2002, 5th International Symposium On Spatial Accuracy Assessment in Natural Resources and Environmental Sciences*, Melbourne, Australia, pp. 348–356.
- Zhan, Q., Molenaar, M. and Lucieer, A. (2002). *Uncertainty in Remote Sensing and GIS*, John Wiley and Sons Ltd., chapter Pixel Unmixing at the Sub-pixel Scale Based on Land Cover Class Probabilities: Application to Urban Areas, pp. 59–77.
- Roo, A. P. J. d., Odijk, M., Schmuck, G., Koster, E. H. and Lucieer, A. (2001). Assessing the effects of land use changes on floods in the Meuse and Oder catchment, *Physics and Chemistry of the Earth* **26**(7–8): 593–599.

- Lucieer, A. (2000). Revising remote sensing classifications, interactive and visual analysis of uncertainty constraints, *Phd research proposal*, International Institute of Geo-Information and Earth Observation (ITC).
- Lucieer, A., Koster, E. H., de Jong, S. M. and Jetten, V. G. (2000). The DAIS La Peyne experiment: Using the optical and thermal DAIS bands to survey and model the surface temperature, *International Archives of Photogrammetry and Remote Sensing*, Vol. XXXIII, GITC, Amsterdam.
- Lucieer, A. and Koster, E. H. (2000). *The DAIS La Peyne experiment: Using the optical and thermal DAIS bands to survey and model the surface temperature*, Master's thesis, Department of Physical Geography, Utrecht University.



# Biography



Arko Lucieer was born on the 17<sup>th</sup> of January 1977 in Rotterdam, the Netherlands. From 1995 to 2000, he studied Physical Geography at Utrecht University, specialising in GIS and remote sensing. He wrote his Masters thesis on modelling the surface thermal heat-balance, using hyper-spectral remote sensing imagery. During a practical period at the Joint Research Centre (JRC) in Italy, he further developed his dynamical modelling skills applied to river flooding. In 2000, he started as a Ph.D. researcher at the International Institute for Geo-Information Science and Earth Observation (ITC) in Enschede, the Netherlands. The research focused on

modelling and visualising uncertainties in remotely sensed image classification and segmentation. During his Ph.D. research, Arko was an Honorary Visiting Research Fellow at Leicester University, UK. He has developed methods for texture-based segmentation and quantification of object uncertainty in remote sensing imagery. His research also aimed to improve awareness of uncertainty in remote sensing image classification and segmentation using interactive visualisation techniques. He has presented his work at several international conferences and has published in international peer-refereed journals. Additionally, he has taught lectures on segmentation, uncertainty, and visualisation at ITC. In June 2004, he started as a lecturer at the Centre for Spatial Information Science, University of Tasmania, Australia.

---